# Modeling Pre-Ignition Dynamics in a Cubic Test Cell Relevant to ASTM E659

Jorge Sanz Sánchez

Faculty Mentor: Prof. Joseph E. Shepherd
Co-Mentor: Dr. Charline Fouchier

September 25, 2026

California Institute of Technology

**Abstract**

Autoignition temperatures (AITs) are widely used in hazard evaluations and measured using the ASTM-E659 standard. AIT is not an intrinsic property and depends on the measurement procedure. Prior efforts by the Explosion Dynamics Laboratory at Caltech have examined variability in autoignition testing, but post-injection vaporization and subsequent mixing remain unclear. Spatiotemporal features vary across vaporization regimes, and convective mixing varies across physical configurations, potentially contributing to AIT variability. This study conducted CFD simulations in a cubic test cell using a reduced-complexity OpenFOAM framework. Initial transient differences among vaporization regimes were suppressed by buoyancy forces arising from the density contrast between air and denser hydrocarbon-fuel vapors, leading to similarly stratified fuel-concentration fields across cases. Subsequent fuel mixing due to the onset of convection was extremely sensitive to wall thermal conditions, which governed a buoyancy-driven convection process capable of accelerating mixing. This process was also influenced by fuel molecular weight and injected fuel quantity. These findings provide a physical explanation for previously unexplained concentration-signal features. The results suggest that differences across vaporization regimes may not dominate AIT variability and highlight the importance of accurately representing wall-temperature boundary conditions in future modeling efforts and experimental design.

# Contents

**1 Introduction** **4**

1.1 Autoignition Temperature and ASTM E659 . . . . . 4

1.2 Pre-Ignition Dynamics and Scope of Study . . . . . 5

**2 Experimental and Numerical Methods** **7**

2.1 Experimental Cell and Instrumentation . . . . . 7

2.2 Geometric Model and Meshing . . . . . 11

2.3 Governing Equations . . . . . 12

2.4 Solver and Thermophysical Model . . . . . 13

2.5 Boundary and Initial Conditions . . . . . 14

2.6 Reduced-Complexity Vaporization Model . . . . . 15

2.7 Analysis Metrics . . . . . 16

2.8 Validation and Model Limitations . . . . . 16

**3 Pre-Ignition Dynamics** **17**

3.1 Reference Case . . . . . 17

3.2 Pre-Injection Circulation . . . . . 18

3.3 Injection and Vaporization . . . . . 19

3.4 Diffusion-Driven Mixing . . . . . 20

3.5 Reformation of Convection . . . . . 20

3.6 Convection Morphology and Stabilization . . . . . 21

3.7 Dynamic Similarity . . . . . 26

3.8 Role of Three-Dimensional Effects . . . . . 29

**4 Sensitivity to Vaporization Characteristics** **29**

4.1 Spatial Source Distribution . . . . . 30

4.2 Vaporization Duration . . . . . 33

4.3 Vaporization-Cooling Sensitivity . . . . . 34

4.4 Additional Vaporization-Driven Mixing Phenomena . . . . . 35

4.5 Conclusions . . . . . 37

**5 Sensitivity to Thermal Conditions** **38**

5.1 Temperature-Profile Distribution . . . . . 38

5.2 Temperature-Profile Magnitude . . . . . 42
5.3 Minimum Wall-Temperature Deficit for Convection . . . . . 45
5.4 Heat-Transfer Model of the Window . . . . . 47
5.5 Experimental Temperature Characterization Inside the Cell . . . . . 50
5.6 Experimental Wall-Temperature Characterization . . . . . 52
5.7 Conclusions . . . . . 55

**6 Sensitivity to Fuel Properties and Fuel Quantity** **56**
6.1 Fuel Molecular-Weight Study . . . . . 56
6.2 Injected-Volume Dependence . . . . . 59
6.3 Temperature Dependence . . . . . 62
6.4 Conclusions . . . . . 63

**7 Conclusions and Future Work** **63**

**Acknowledgments** **66**

**A Numerical Settings** **66**

**B Initialization Issues and Fixes** **67**

**C 3D Simulations** **67**

**D Heat-Transfer Model** **70**

**E Derivations** **73**
E.1 1D Diffusion Analytical Model . . . . . 73
E.2 Navier Stokes Non-Dimensional Equations . . . . . 73
E.3 Frequency of Internal Waves in a Box . . . . . 77

# 1 Introduction

## 1.1 Autoignition Temperature and ASTM E659

The Autoignition Temperature (AIT) is defined as the minimum temperature at which a fuel will ignite without an external ignition source at atmospheric pressure. The AIT is a relevant property that guides hazard evaluations and safety decisions across industrial processes where hot surfaces and flammable atmospheres may be present. The AIT, however, is not an intrinsic fuel property and varies with the measurement procedure, as discussed by Martin and Shepherd [1]. Johnson and Mashuga [2] noted variability in the measured AIT for a given fuel, sometimes on the order of tens of degrees Celsius, highlighting how results depend on the measurement procedure. Table 1 shows the variation of AIT values reported in the literature for a group of selected fuels.

| **Reference [1]** | **Hexane** | **Propanol** | **Acetone** |
|---|---|---|---|
| Thompson (1929) | 253 | 452 | 623 |
| Scott et al. (1948)[a] | 248 | 439 | 561 |
| Setchkin (1954) | 240 | ∼ | 491 |
| Mullins (1955)[a] | 248–487 | 433–505 | 538–727 |
| Zabetakis (1965) | 225 | 440 | 465 |

**Table 1:** Autoignition temperatures reported in the literature.[2] Values are in °C

.

The ASTM E659 is the North American standard[3] for measuring AITs. The test consists of a heated flask in which fuel is inserted and observed for ignition. In an effort to reduce the variability of the data produced by the standard, the Explosion Dynamics Laboratory (EDL) at Caltech has recently focused on automating the test injection process and studying variations in mixing phenomena across the different flask geometries permitted by the current experimental configuration. Specifically, Davis et al.[4] showed that a shorter flask neck would yield stronger convection currents inside the apparatus, as the cold air protruding from the flask's opening would more effectively reach the flask's main body. The flow fields of the simulations exploring the effect of height are provided in Figure 1.

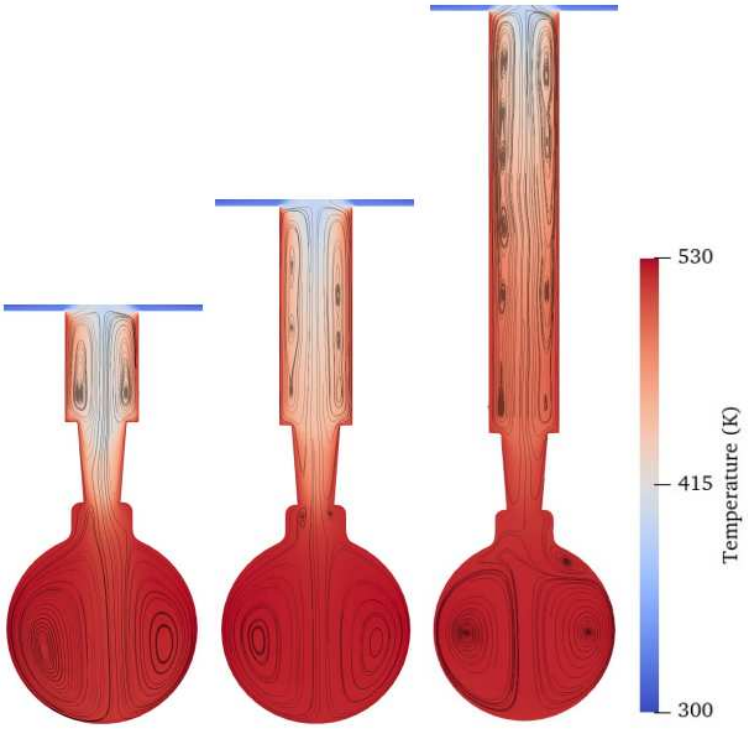



**Figure 1:** Effect of flask height difference in thermal and mixing fields, reproduced from Davis et al.[4]

These findings raised the question of how the mixing physics within the apparatus could vary across fuels and temperatures, and how these variations could affect the experiment's pre-ignition environment.

## 1.2 Pre-Ignition Dynamics and Scope of Study

Davis et al.[5] carried out numerical simulations of the ASTM E659, focusing on heat transfer and fluid motion phenomena. He showed that differences in molecular weights among fuels would alter their mixing processes. Specifically, higher molecular weights were associated with slower mixing times. The higher buoyancy forces and lower diffusivities associated with the heavier fuels created a stratified, fuel-rich region at the bottom of the apparatus, which took a significant time (on the order of tens of seconds more than the lighter fuels) to mix into a homogeneous mixture through diffusion and convection.[4] A main limitation of Davis's simulations was the omission of the vaporization process; fuel was initialized directly in a gaseous state in a region at the center of the main body. Differences in the vaporization processes, determined by the case temperature and the fuel used, remained to be investigated to assess whether they contributed to variability in the mixing process.

To further investigate the mixing process, the EDL developed a cubic test-cell setup (see Fouchier et al.[6]) that provided improved experimental access. The cubic test cell was instrumented with Background Oriented Schlieren (BOS) imaging, which captures density differences in the volume; infrared laser absorption, which is used to quantify concentration changes along a laser path located at the mid-height of the flask; high-speed imaging; and various thermocouple probes to acquire temperature measurements. Note that the experimental techniques used are explained in detail in Section 2.1. A picture of the experimental test cell is shown in Figure 2.



**Figure 2:** Experimental cubic test cell of Fouchier et al. [6]

The concentration signal obtained in the new cell exhibited[6] a significant transient increase that differed from the analytically derived evolution corresponding to a purely diffusive phenomenon, hinting at the presence of a convection current inside the cell that alters and enhances the mixing process. The concentration signal matched that associated with a diffusive process until the sudden peak appeared, delimiting a clear diffusion-driven and a convection-driven period. This is portrayed in Figure 3 for hexane.

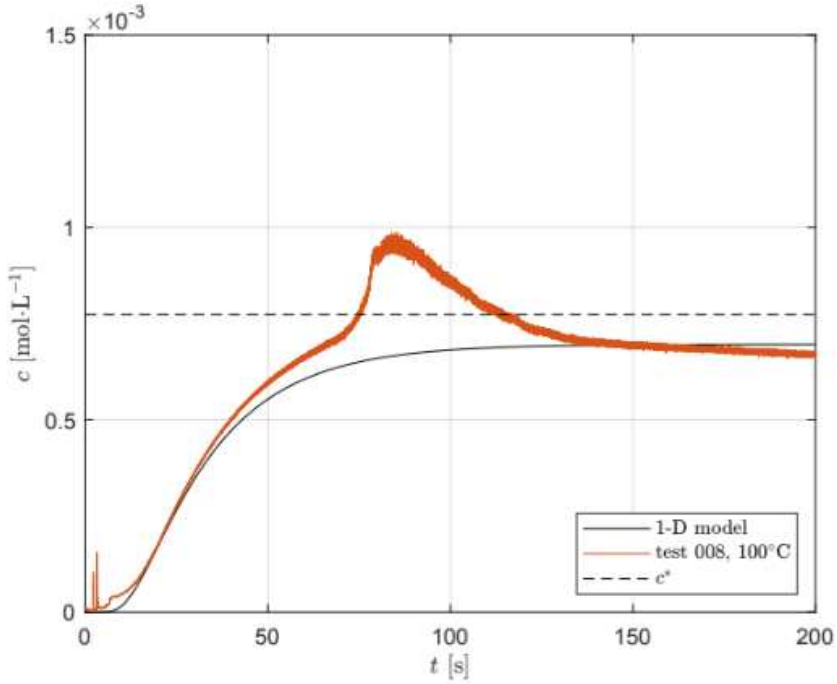



**Figure 3:** Comparison of test measurements of fuel (hexane) concentration at $z/H = 0.5$ with 1D model predictions and ideal final concentration $c^*$ based on a fuel volume of 100 $\mu$L and test cell temperature of 100 °C, reproduced from Fouchier et al. [6]

Fouchier et al.[6] showed that a similar convection signal could be attributed to thermal deficits at the cell's side walls, which are not perfectly insulated. However, the timing and morphology of the signal differed greatly from the experimentally obtained signal, and its origin remained unclear.

The current work aims to provide further insight into this unexplained signal and the overall mixing mechanism by carrying out 2D OpenFOAM-based numerical simulations of the pre-ignition environment, focusing on the main candidate causes of the convection: vaporization-process-induced differences, cell temperature conditions, and fuel properties. Additional experiments will be performed to confirm the computational trends.

We found that the onset of convection was not affected by differences in the vaporization process for fuels with molecular weight above 80 g/mol for cases where $T_{\text{cell}} > T_{\text{boiling}}$ since the compositional buoyancy that erases these initial differences increases with fuel molecular weight. Differences in vaporization histories were rapidly diminished by a strong buoyancy force generated by the large density difference between fuel vapor and air that led to a similarly stratified initial concentration field across different vaporization conditions. We also found that the timing and morphology of the convection process were extremely sensitive to wall thermal conditions, which created density differences in the volume and triggered natural convection. The timing of the convection process was also influenced by fuel properties, with higher-molecular-weight fuels exhibiting lower diffusivities, thereby postponing the onset of the convection-driven period. Overall, the results show that the onset of the convection period is driven by a competition between stabilizing compositional stratification and destabilizing thermally driven buoyancy.

# 2 Experimental and Numerical Methods

## 2.1 Experimental Cell and Instrumentation

The cubic test cell consisted of a 1-liter cell fabricated from metal (aluminum and stainless steel) and 2 mm quartz windows to provide optical access to the cell. The 1-liter cell was enclosed in a housing made of aluminum and glass wool to insulate it and minimize heat losses. The north-south pair of windows included an additional 2 mm quartz window spaced 1 inch apart to minimize natural convection heat losses. Window shutters composed of aluminum and a 1-inch-thick glass wool insulation were also installed along the north-south direction with the same purpose. The shutters were retracted as the experiment began to allow visualization. The east-west direction had no shutters or additional windows and consisted of a small circular perforation in the housing and rectangular aluminum cover sheets at the window, which left a vertical gap to accommodate the laser path. The apparatus heating system consisted of feedback-controlled electric heaters placed at the top and bottom aluminum plates.

The Phantom v2512 high-speed camera was set up in the north-south direction and used to record vaporization imaging and to capture density differences using the background-oriented Schlieren (BOS) method. BOS captures density gradients by measuring the apparent displacement of a background dot pattern caused by refractive-index gradients within the test volume. BOS provides a path-integrated measurement by capturing changes in density across a 3D volume and projecting them onto a 2D image.

A He-Ne laser (Thorlabs H339P2) with a 1 mm output diameter was used to obtain quantitative concentration measurements in the cell. The method uses Beer-Lambert's law of absorption.

$$I(t) = I_0 \exp\left(-\sigma \bar{c}(t) l\right), \qquad \bar{c}(t) = \frac{1}{l}\int_0^l c(x,t)\, dx. \tag{1}$$

Which measures the average concentration $\bar{c}(t)$ along the laser path $l = 10\,\text{cm}$. The absorption cross section $\sigma$ varied among the different fuels investigated, and measured values were obtained from the Mével et al.[7] compilation. The dodecane value of $70.2\,\text{m}^2/\text{mol}$ was calculated using the Mével et al. correlation formula for the estimation of hydrocarbon cross-sections. The line-integrated concentration measurement was replicated in the numerical simulations and was used as the mixing benchmark in the present studies. Table 2 presents the absorption cross sections at $3.39\,\mu\text{m}$ for the n-alkanes used in the experimental analysis at 373 K.

| **Fuel** | **Absorption cross section, $\sigma$ [m$^2$/mol]** |
|---|---|
| n-Pentane | 33.48 |
| n-Hexane | 40.09 |
| n-Heptane | 43.88 |
| n-Octane | 47.27 |
| n-Dodecane | 70.2 |

**Table 2:** Absorption cross sections at $3.39\,\mu\text{m}$ for the n-alkanes used in the experimental analysis at 373 K Values from Mével et al.[7].

Experimental repeatability for the concentration measurements is demonstrated for the current setup in Figure 4[6], enabling inference of trends from the data.

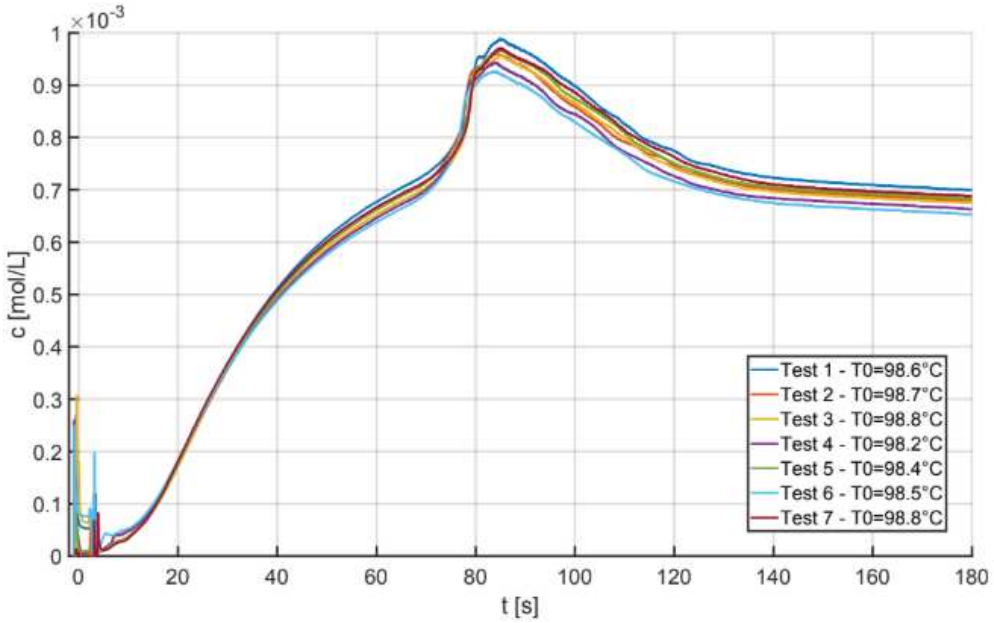



**Figure 4:** Repeatability of experimental setup for a $100\,\mu\text{L}$, 100 °C injection of hexane. Reproduced from Fig. 4 of Fouchier et al.[6].

Temperature measurements were obtained at 75 Hz using Omega-type K thermocouples. The original setup included a thermocouple suspended at the center of the cell ($T_4$) and two thermocouples

($T_5$ and $T_6$) placed on the top and bottom aluminum plates, used for the feedback heating control algorithm.

The temperature characterization setup was extended by performing tests with a T-shaped 3-thermocouple probe with a width of 3 inches to characterize the pre-injection temperature field. The T-shaped probe was placed parallel to both the N-S and E-W directions and moved upward in discrete increments of 10 mm in the $[0, 100]$ mm vertical direction along the center and windows inside the cell; each position reports an uncertainty of $\pm 10$ mm. For the thermocouple movable-probe, a central thermocouple was added to the previously used T-shaped thermocouple arrangement[8]. An image of the probe is shown in Figure 5. A sketch showing the thermocouple numbering and the two probe orientations is included below.



**Figure 5:** Thermocouple probe used for the pre-injection thermal characterization of the cubic test cell.

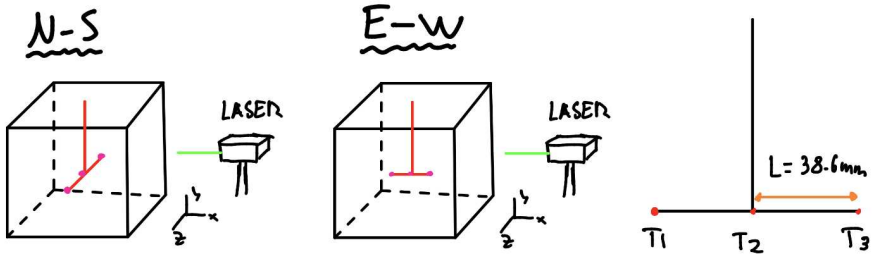



**Figure 6:** Sketch of the thermocouple numbering and probe orientations used during the thermal characterization.

Repeatability was verified for the measurements taken with the T-shaped probe. The cell environment was confirmed to remain relatively constant between trials. $T_4/T_{\text{cell}}$ (thermocouple in the middle of the cell), $T_5/T_{\text{top}}$ (thermocouple at the top plate), and $T_6/T_{\text{bot}}$ (thermocouple at the bottom plate) showed similar values across repeated experiments. The variation in $T_4/T_{\text{cell}}$ remains within $\pm 1\,^{\circ}\text{C}$, which is smaller than the thermocouple uncertainty of $\pm 2\,^{\circ}\text{C}$. One of the thermocouple temperature versus measurement-number plots is presented in Figure 7, portraying the repeatability.

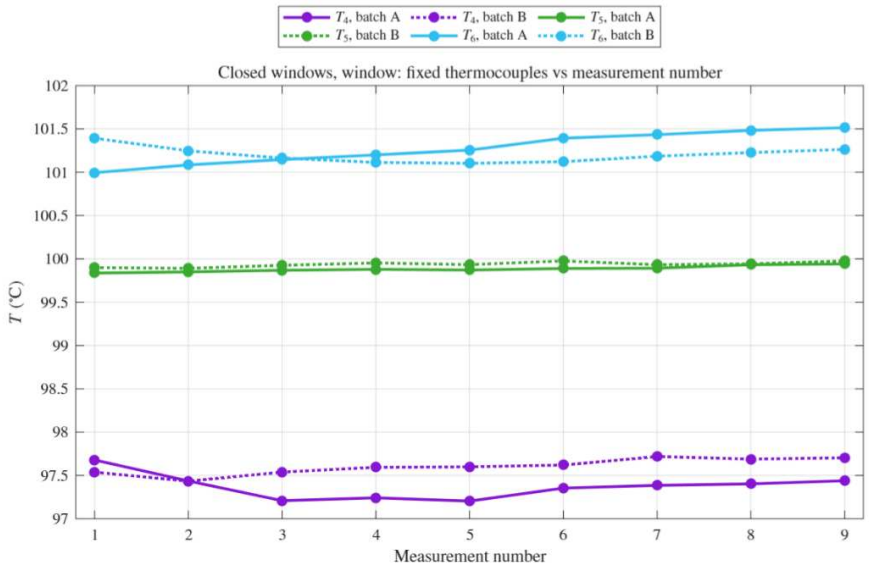
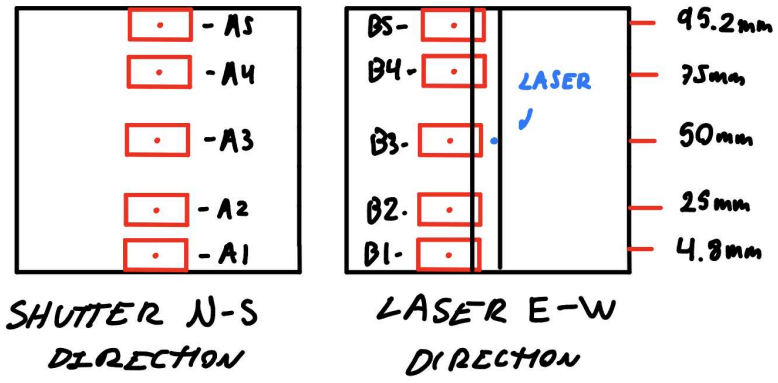
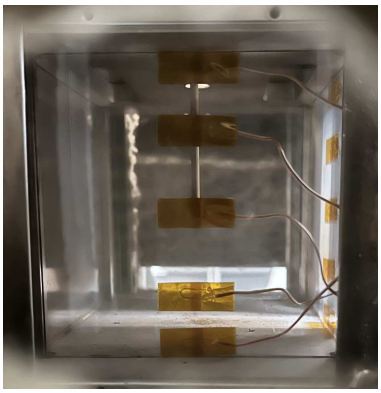



**Figure 7:** Fixed thermocouples versus measurement number for the closed-windows, along-the-window case.

The temperature characterization was further extended by placing 5 static self-adhesive thermocouples on one wall of both the N-S and E window pairs to characterize wall thermal conditions. The thermocouples were placed at approximately the horizontal center of the cell and were placed vertically at [5 25 50 75 95] mm ±5 mm uncertainty. All type K thermocouples report a thermocouple uncertainty of ±2°C. Figure 8 shows a schematic of the thermocouple positions and an image of the experimental setup with the thermocouples taped in place.




**(a)** Schematic of the self-adhesive thermocouple positions.



**(b)** Experimental setup with the self-adhesive thermocouples taped in place.

**Figure 8:** Self-adhesive thermocouple setup used for the characterization of the wall thermal conditions: (a) thermocouple position schematic and (b) experimental setup.

Repeatability was verified among experiments. The wall temperatures were confirmed to be relatively constant within experiments, with a mean standard deviation of ±0.445 °C across thermocouples, below the thermocouple uncertainty of ±2 °C. Figure 9 shows the repeatability of the self-adhesive

thermocouple measurements for 5 different tests.

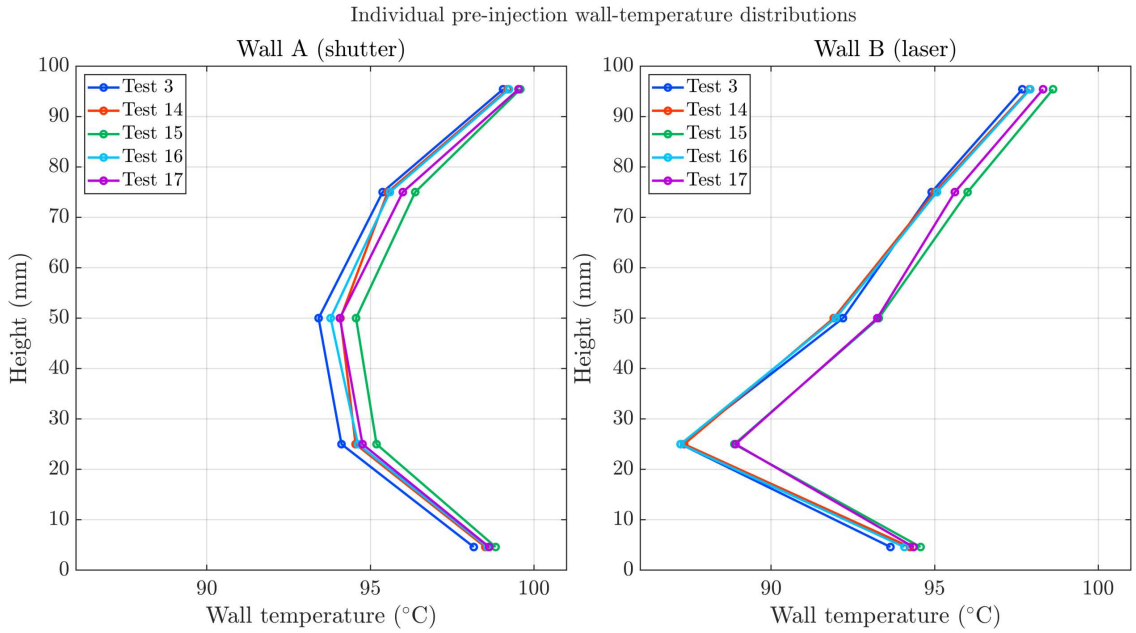
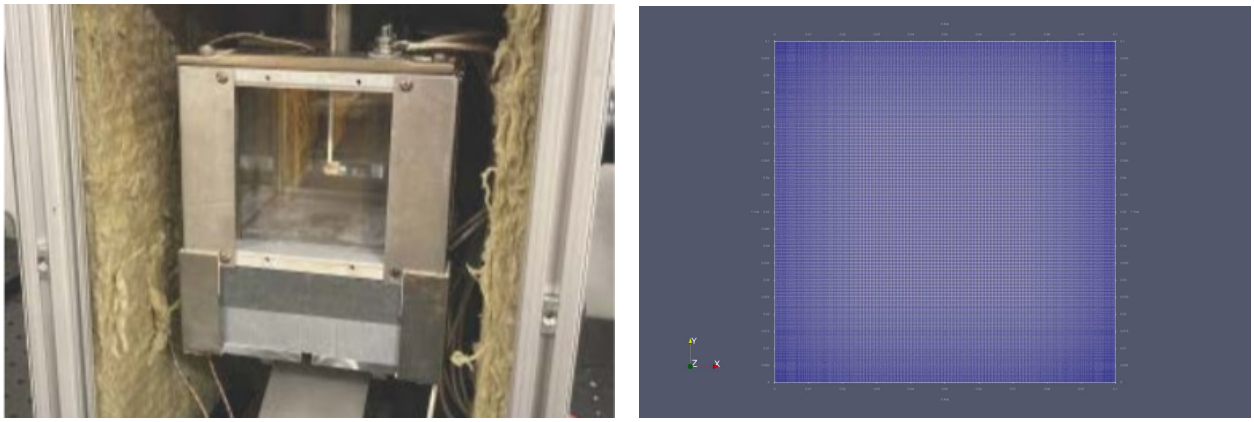



**Figure 9:** Repeatability of the self-adhesive thermocouple measurements across five different tests.

## 2.2 Geometric Model and Meshing

The main geometric model is the two-dimensional version of the cubic test cell. The 2D dimensions of the cell are 100 mm $\times$ 100 mm. The meshing process was performed using OpenFOAM's hexahedral mesher, blockMesh. The cells in the simulations are perfectly hexahedral and thus report 0 points of non-orthogonality. The grid spans 300 $\times$ 300 cells, with graded refinement near the walls to improve the resolution of thermal and momentum boundary layers. The average nominal cell dimension is 333 $\mu$m. Grid independence was demonstrated for this value on the pre-injection initialization field. A few coarse grid simulations were also performed in a three-dimensional cell. The 3D dimensions of the cell are 100 mm $\times$ 100 mm $\times$ 100 mm, and the grid spanned 100 $\times$ 100 $\times$ 100 cells, with an average nominal cell dimension of 1 mm. Grid independence was not demonstrated for this value due to insufficient computational resources; thus, the results are inconclusive. 3D simulations are provided in Appendix C. Pictures of the experimental test cell and the 2D mesh are shown in Figure 10.



**(a)** **(b)**

**Figure 10:** (a) North side view of the experimental cubic test cell, reproduced from Fouchier et al.[6]. (b) Solution mesh with verified grid independence for the pre-injection field.

## 2.3 Governing Equations

The governing equations are the Navier–Stokes equations for a non-reacting, non-Boussinesq, variable-density, buoyancy-driven, reduced-pressure, multispecies ideal-gas mixture with external vaporization-derived mass source terms. They can be represented in the following form:

$$\frac{\partial \rho}{\partial t} + \nabla \cdot (\rho \mathbf{u}) = S_{m,\text{fuel}} \tag{2}$$

*Mass conservation.*

$$\frac{\partial (\rho \mathbf{u})}{\partial t} + \nabla \cdot (\rho \mathbf{u}\mathbf{u}) = -\nabla p_{rgh} - gh\nabla\rho + \nabla \cdot \boldsymbol{\tau}. \tag{3}$$

*Momentum conservation.*

$$\frac{\partial (\rho Y_{fuel})}{\partial t} + \nabla \cdot (\rho \mathbf{u} Y_{fuel}) = -\nabla \cdot (-\rho D_{fuel-air} \nabla Y_{fuel}) + S_{m,\text{fuel}} \tag{4}$$

*Fuel species conservation.*

$$Y_{air} = 1 - Y_{fuel} \tag{5}$$

*Species fraction closure.*

$$\begin{aligned} \frac{\partial}{\partial t}\left[\rho\left(h + \frac{1}{2}\mathbf{u}\cdot\mathbf{u}\right)\right] + \nabla \cdot \left[\rho \mathbf{u}\left(h + \frac{1}{2}\mathbf{u}\cdot\mathbf{u}\right)\right] \\ = \frac{\partial p}{\partial t} + \rho \mathbf{u}\cdot\mathbf{g} + \nabla\cdot(\kappa\nabla T) \\ - \nabla\cdot\left[\left(-\rho D_{\text{fuel}-\text{air}}\nabla Y_{\text{fuel}}\right)\left(h_{\text{fuel}} - h_{\text{air}}\right)\right] + S_{m,\text{fuel}} h_{\text{fuel,inj}}. \end{aligned} \tag{6}$$

*Energy conservation.*

The symbols are: $t$, time; $\rho$, mixture density; $\mathbf{u}$, velocity; $p$, pressure; $\mathbf{g}$, gravitational acceleration; $\boldsymbol{\tau}$, viscous stress tensor; $h$, mixture specific enthalpy; $h_{\text{fuel}}$ and $h_{\text{air}}$, fuel and air specific enthalpies, respectively; $h_{\text{fuel,inj}}$, specific enthalpy of the injected fuel vapor; $\kappa$, mixture thermal conductivity; $T$, temperature; $D_{\text{fuel}-\text{air}}$, binary fuel–air diffusion coefficient; $Y_i$, species mass fraction; and $S_{m,\text{fuel}}$, the volumetric fuel mass-source term.

Note that a constant binary fuel–air diffusion coefficient, $D_{\text{fuel}-\text{air}}$, was adopted as a modeling simplification. For each fuel, $D_{\text{fuel}-\text{air}}$ was obtained by considering the infinite-dilution limit of fuel vapor in air for the molecules of interest at the reference temperature and pressure.

The equation of state for the ideal gas is:

$$\rho = \frac{p}{R_{mix}T}, \qquad R_{mix} = R_u \left( \frac{Y_{air}}{W_{air}} + \frac{Y_{fuel}}{W_{fuel}} \right) \tag{7}$$

where $R_{mix}$ is the mixture gas constant, $R_u$ is the universal gas constant, and $W_{air}$ and $W_{fuel}$ are the molecular weights of air and fuel, respectively.

The viscous stress tensor can be defined as:

$$\boldsymbol{\tau} = \mu \left[ \nabla \mathbf{u} + (\nabla \mathbf{u})^T - \frac{2}{3}(\nabla \cdot \mathbf{u})\mathbf{I} \right] \tag{8}$$

where $\mathbf{I}$ is the identity matrix.

## 2.4 Solver and Thermophysical Model

The framework uses the solver `multicomponentFluid` within the new OpenFOAM 13 modular solver structure. This solver supersedes the prior version `buoyantReactingFoam`. `multicomponentFluid` is defined as "Solver module for steady or transient turbulent flow of compressible multicomponent fluids with optional mesh motion and change" from the OpenFOAM documentation[9].

The modeled current is two-species, non-reacting, variable-density, and buoyancy-driven. Because of the large density variations due to both temperature and composition gradients across the test cells, the Boussinesq approximation is not applied; buoyancy force is directly computed from $-gh\nabla\rho$, and density changes are computed through the full equation of state of the gas, which takes into account composition, temperature, and pressure changes: $f(Y_i, P, T)$.

The current solver is set up to use the reduced-gravity pressure $p_{\text{rgh}}$. The reduced-pressure, $p_{\text{rgh}}$, is defined as $p_{\text{rgh}} = p - \rho(gh)$. Its main benefit is that it removes the stiff, large hydrostatic pressure component $\rho gh$ from the solution of the pressure variable, leaving only the small, dynamic, and thermodynamic changes. This is a common approach for buoyancy-driven flow solvers as discussed in the OpenFOAM documentation for `prghPressure`[10].

Turbulent effects are currently neglected due to the Reynolds number being consistent with a laminar treatment of the flow,

$$Re = \frac{UL}{\nu} = \frac{(0.1 \text{ m/s})(0.10 \text{ m})}{2.3 \times 10^{-5} \text{ m}^2/\text{s}} \approx 440 \tag{9}$$

where $U = 0.1$ m/s is the maximum velocity of the simulation, $L = 100$ mm is the characteristic length of the test cell, and $\nu \approx 2.3 \times 10^{-5}$ m$^2$/s is the kinematic viscosity of air at approximately 100 °C.

The framework's thermophysical package is built from native OpenFOAM models as follows. The `JANAF` model is selected to compute temperature-dependent thermodynamic properties, such as specific heat[11]. The Sutherland transport model is used to compute viscosity and conductivity as functions of temperature:

$$\mu = A_s \frac{\sqrt{T}}{1 + T_s/T}, \tag{10}$$

$$\kappa = \mu c_v \left(1.32 + 1.77 \frac{R}{c_v}\right). \tag{11}$$

where $\mu$ is the dynamic viscosity, $\kappa$ is the thermal conductivity, $A_s$ and $T_s$ are Sutherland coefficients, and $c_v$ and $R$ are the specific heat at constant volume and gas constant, respectively. The individual species properties are subsequently combined according to the local mixture composition.

The selected diffusion model is `FickianFourier`; diffusion is modeled by prescribing the infinite-dilution simplification fuel–air binary diffusion coefficient, $D_{\text{fuel}-\text{air}}$, at the case reference temperature and pressure. Using the mixture-averaged diffusion coefficient:

$$D_{i,m} = \frac{1 - Y_i}{\sum_{j \neq i} \frac{X_j}{D_{ij}}}, \tag{12}$$

where $X_j$ is the species mole fraction and $D_{ij}$ is the binary diffusion coefficient between species $i$ and $j$. For fuel at infinite dilution in an air $N_2$–$O_2$ mixture, $Y_{\text{fuel}} \to 0$, such that

$$D_{\text{fuel}-\text{air}} = \left(\frac{X_{N_2}}{D_{\text{fuel}-N_2}} + \frac{X_{O_2}}{D_{\text{fuel}-O_2}}\right)^{-1}. \tag{13}$$

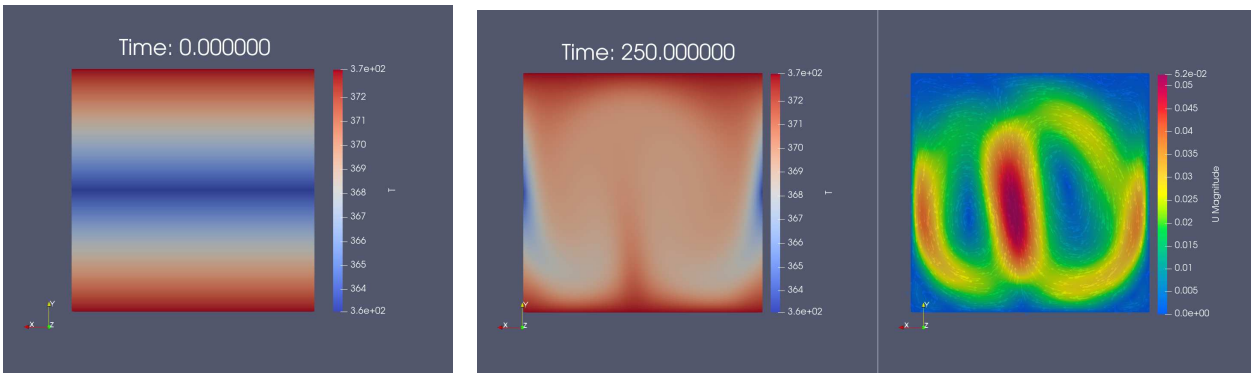
Note that mixture-averaged diffusion formulations generally require a correction velocity $V_c$ to enforce net zero mass flux associated with diffusion[12]; however, because the current treatment is a binary species, $Y_{\text{air}} = 1 - Y_{\text{fuel}}$ gives $\nabla Y_{\text{air}} = -\nabla Y_{\text{fuel}}$, and thus $-\rho D \nabla Y_{\text{air}} - \rho D \nabla Y_{\text{fuel}} = 0$, making the diffusive mass fluxes automatically balance. The Soret effect is not included in the reduced-complexity framework. The species simulated are a hydrocarbon fuel, hexane for most simulations, and air, which is treated as one species. The specific species included per simulation are noted in the discussion of the results.

### 2.5 Boundary and Initial Conditions

The simulation is carried in two different stages. First, the case is initialized only with air with the corresponding boundary and initial conditions. The boundary conditions include no-slip walls, constant top and bottom wall temperatures at the case reference temperature, and an imposed thermal deficit on the side walls. The specific thermal deficit varies depending on the simulation and study. The temperature profile along the walls is intended to approximate heat loss near the windows. The initial temperature field follows that of the boundary conditions imposed, with the thermal deficit of the walls being applied initially to all the domain. Once the simulation

is initialized, some time is needed for it to develop a transient stable field, characterized by an oscillating convection plume.

Images of the imposed boundary and initial temperature profile, as well as the developed transient dry-air field, are shown in Figure 11.




**(a)** **(b)**

**Figure 11:** (a) Imposed initial and boundary temperature profile. (b) Developed pre-injection oscillatory dry-air field showing the oscillatory convection plume.

The second stage involves the injection process. The initial conditions of this stage are taken as the last time step of the prior initialization stage. The boundary conditions of the case are kept constant. The injection process itself will be explained in the following section.

## 2.6 Reduced-Complexity Vaporization Model

The injection approach involves representing the main effect of the vaporization process on the flow field, mass addition, where vaporization adds fuel into the flask, changing composition, density and buyoancy.

This effect is modeled through vapor mass source. It is implemented using the subdictionary `massSource` within the dictionary `fvModels`. Detailed vaporization physics, such as droplet dynamics, are not represented in the current framework.

The mass source is defined as:

$$S_{m,\text{fuel}} = m_{\text{vap}} F(\mathbf{x}) G(t). \tag{14}$$

$m_{\text{vap}}$ is the total fuel mass, $G(t)$ a normalized temporal distribution representing the vaporization event, and $F(\mathbf{x})$ a normalized spatial function capturing the morphology of the vaporization region. The added fuel is introduced as vapor at $T_{\text{vap}}$.

Here, $F(\mathbf{x})$ is normalized over the source volume and $G(t)$ is normalized over the vaporization duration, so that the integrated sources add to the total mass $m_{\text{vap}}$. The current approach uses the spatial and temporal distributions to help distinguish vaporization regimes, such as LDF from non-LDF cases. For example, major temporal and spatial differences will be captured through a separate calibration of $F(\mathbf{x})$, and $G(t)$.

The effect of vaporization cooling has been neglected as its thermal-buoyancy contribution produced no discernible effect with respect to the composition-driven buoyancy in the sensitivity study from

Section 4.3. It was also observed experimentally that the temperature of the walls did not vary significantly during the vaporization process, confirming that vaporization is not the cause of the thermal deficit at the window walls. Details are given in Section 4.3.

In addition, no momentum or directionality is added to the source. Its location and timing is tied to experimental imaging data, and the active flow field within the simulation will govern the physical transport mechanism.

## 2.7 Analysis Metrics

Flow post-processing was done using the free software ParaView. Concentration measurements were obtained by integrating fuel concentration along a horizontal line at the mid-height of the flask, mirroring the method used to obtain the experimental signal. Velocity, temperature, density, composition, and pressure values were sampled across the simulation every 0.5s. Higher-frequency sampling of these variables, at 0.05s, was carried out in regions of relevance (e.g., the horizontal laser path line).

To quantify differences in convection among cases, two characteristic times are defined. The first, time until convection begins, answers when convection appears after injection; the second, time from onset to stability, answers how long it takes for convection to stabilize after it appears. To determine these times, the evolution of the total kinetic energy:

$$E_k = \int_V \frac{1}{2}\rho|\mathbf{U}|^2\,dV \;\approx\; \sum_i \frac{1}{2}\rho_i \left(U_{x,i}^2 + U_{y,i}^2\right)\Delta V_i.$$

in the 2D domain was tracked. The convection onset event was defined as the moment, after injection, where the total kinetic energy in the domain exceeded 5 percent of the maximum simulation value. The convection stabilization event was defined as the moment when total kinetic energy varies by less than 1 percent of the total maximum kinetic energy for at least 5 s after the formation of convection.

## 2.8 Validation and Model Limitations

The current framework was validated against the analytical 1D diffusion model shown in Appendix E.1, and Fouchier et al.[6] OpenFOAM 6 results. The model agreement with both models is shown in Figure 12.

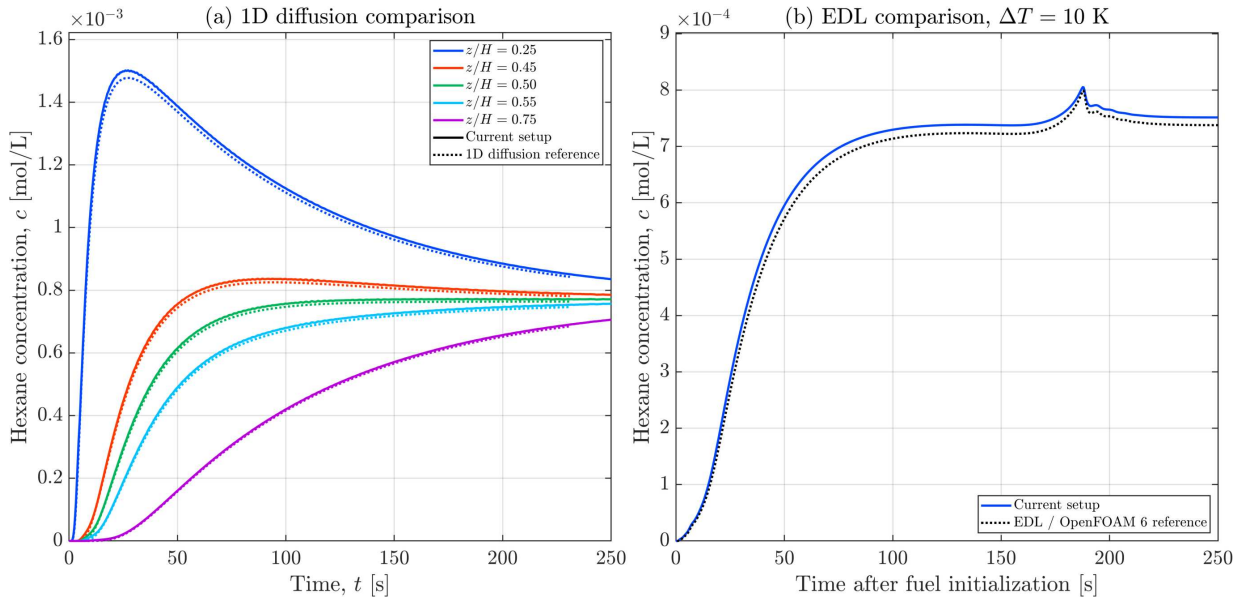



**Figure 12:** Validation of the current OpenFOAM framework against the analytical 1D diffusion model and prior EDL OF6 simulations[6].

The main limitation of the current approach is the 2D simplification. The concentration signal inferred from the simulation cannot be fully interpreted as the experiment's because a third dimension affecting dispersion within the cell is missing. However, the current framework is a very useful tool for analyzing trends among the relevant variables of the problem and informing the experiment.

# 3 Pre-Ignition Dynamics

## 3.1 Reference Case

The main mechanism of pre-ignition mixing inside the cell varies in morphology, timing, and magnitude among different injection volumes, fuels, and temperatures. Still, the same underlying physics is observed across most of the rapid-vaporization cases considered. Accordingly, a reference case will be selected to discuss the principal mixing mechanism in depth, and the sensitivity of the process to different problem parameters will be examined in detail in the following sections.

The reference case chosen to explain the mixing mechanism is shown in Table 3. The imposed wall temperature distribution is shown in Figure 13.

| **Parameter** | **Reference value** |
|---|---|
| Fuel | Hexane |
| Case temperature | 100 °C |
| Temperature boundary conditions | 15 °C deficit over $H/10 \leq h \leq 9H/10$, with linear interpolation to zero deficit at the top and bottom walls |
| Injected volume | 100 $\mu$L |
| Vaporization duration | 5 s |
| Vaporization shape | 50 mm × 5 mm at the bottom center |

**Table 3:** Reference case to explore pre-ignition dynamics.

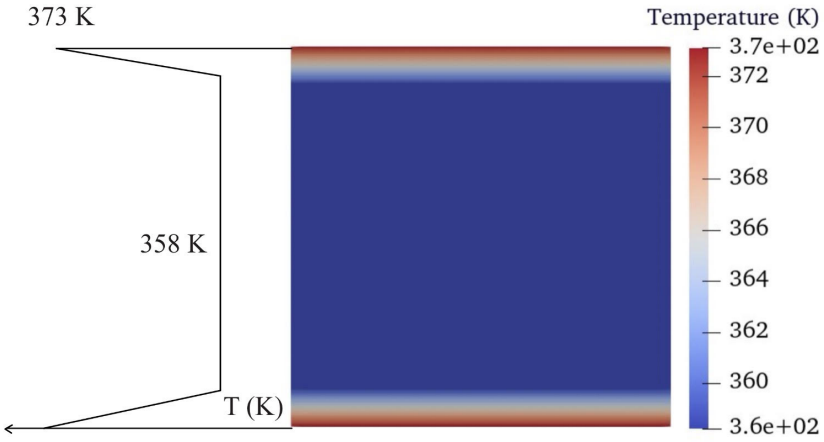



**Figure 13:** Imposed wall temperature distribution for the reference case.

## 3.2 Pre-Injection Circulation

Before any results can be discussed, the pre-injection field must reach a stable, developed state. This was concluded when the simulation reported a periodic, repeatable behavior. The exact time to reach this state varied from case to case according to their specific conditions but was in the order of 150–350 s. Figure 14 shows the evolution of temperature at the center probe $T_{\text{cell}}$ until the reference state reaches the developed periodic state.

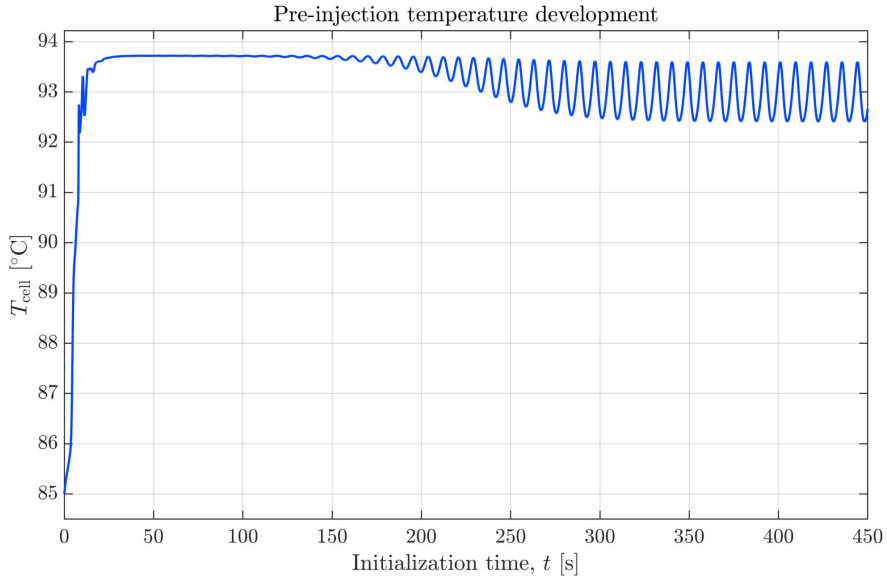



**Figure 14:** Time evolution of $T_{\text{cell}}$ until reaching a stable state

After the stabilization is reached, the first finding is that convection is present in the cell even before injection. This circulation is driven by thermal buoyancy. The imposed wall thermal deficit, intended to capture heat loss from the cell, cools the air near it (1). The cooler gas has a higher density, as can be seen through the equation of state, $\rho = pW/(R_u T)$, and thus sinks (2), creating

two downward momentum regions at the side walls (3). This downward momentum is redirected upwards (4) by the square geometry, and two circulation cells form (5). Figure 15 provides an explanatory diagram of the circulation process inside the cell.

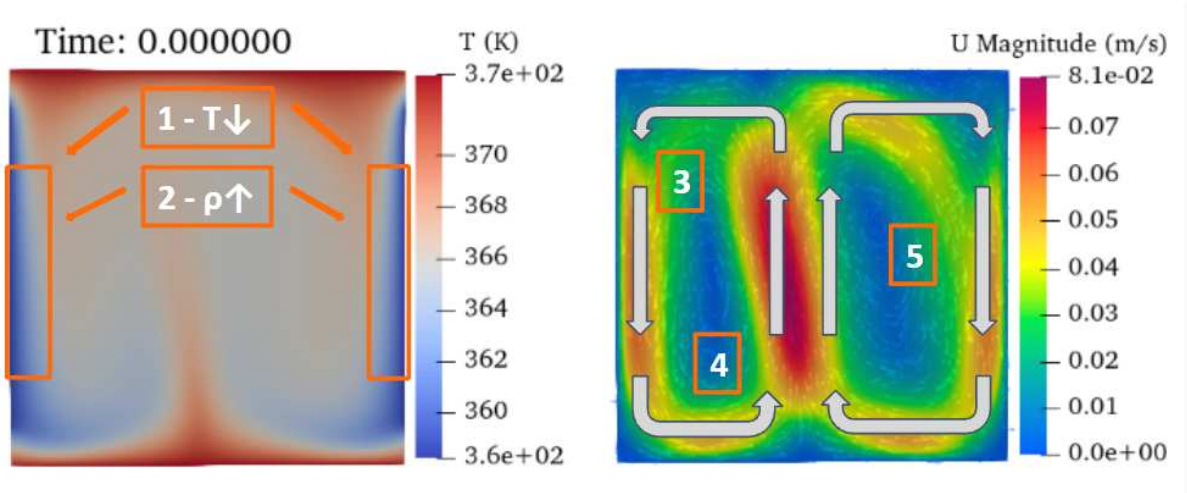
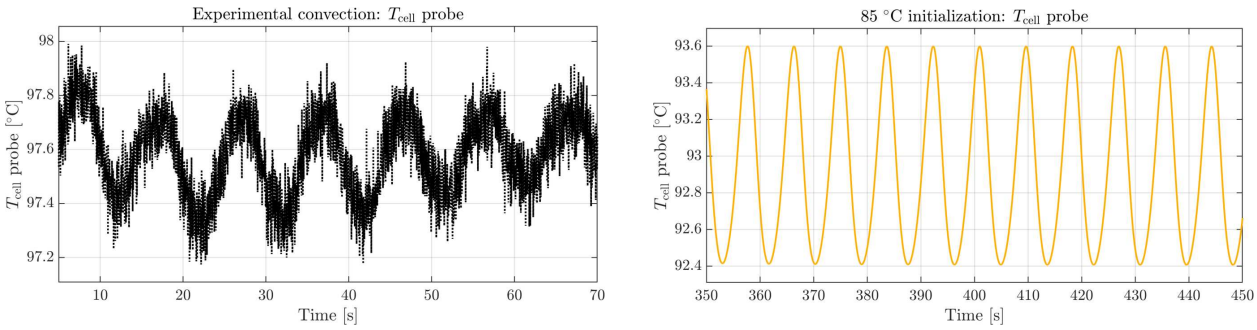



**Figure 15:** Explanatory diagram of the circulation process inside the cell using the temperature (left) and velocity (right) fields.

It is also noteworthy that the central plume exhibits an inherent side-to-side oscillation, which manifests as small periodic variations in the problem variables, such as temperature, at a center probe. This oscillatory behavior has also been observed in the experimental setup, with comparable orders of magnitude for amplitude and frequency; some samples of this phenomenon are shown in Figure 16. Note that the exact frequency and amplitude vary between experiments and simulations.



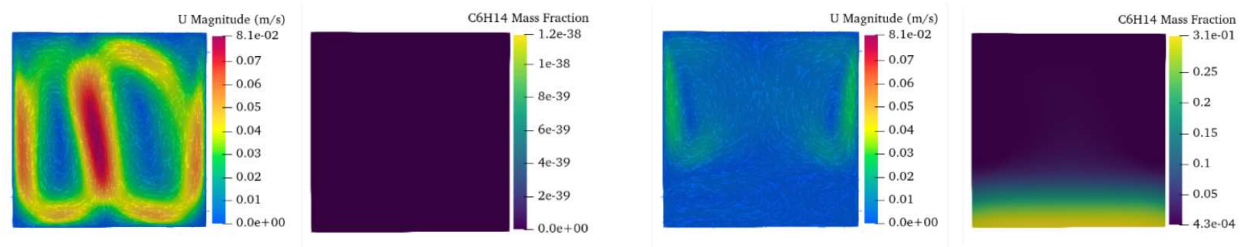

**(a)** Experimental $T_{\text{cell}}$ temperature oscillations.

**(b)** Numerical $T_{\text{cell}}$ temperature oscillations.

**Figure 16:** Experimental and numerical $T_{\text{cell}}$ temperature oscillations.

### 3.3 Injection and Vaporization

After the fuel is injected and vaporized, the pre-injection convection field is strongly suppressed by compositional buoyancy forcing, resulting in a nearly stagnant field and a highly fuel-rich stratified layer at the bottom of the cell. The difference between pre-injection and 10 s after injection is shown in Figure 17.




**(a)** $t = 0$: velocity and compositional fields. **(b)** $t = 10\,\mathrm{s}$: velocity and compositional fields.

**Figure 17:** Velocity and compositional (mass fraction) fields before injection and 10 s after injection.

## 3.4 Diffusion-Driven Mixing

After injection, the highly fuel-rich layer begins to mix via diffusion. This can be confirmed by noticing the coincidence of the obtained concentration curve to the 1D diffusion analytical model[6] except for the transient between 70 and 100 s. Details of the model are given in Appendix E.1. The timing of the diffusive process will vary across fuels, volumes, and temperatures on the order of tens of seconds. Figure 18 portrays a comparison of the measured concentration evolution at $H/2$ for the cubic cell and the predicted 1D diffusion model for the reference case initial conditions.

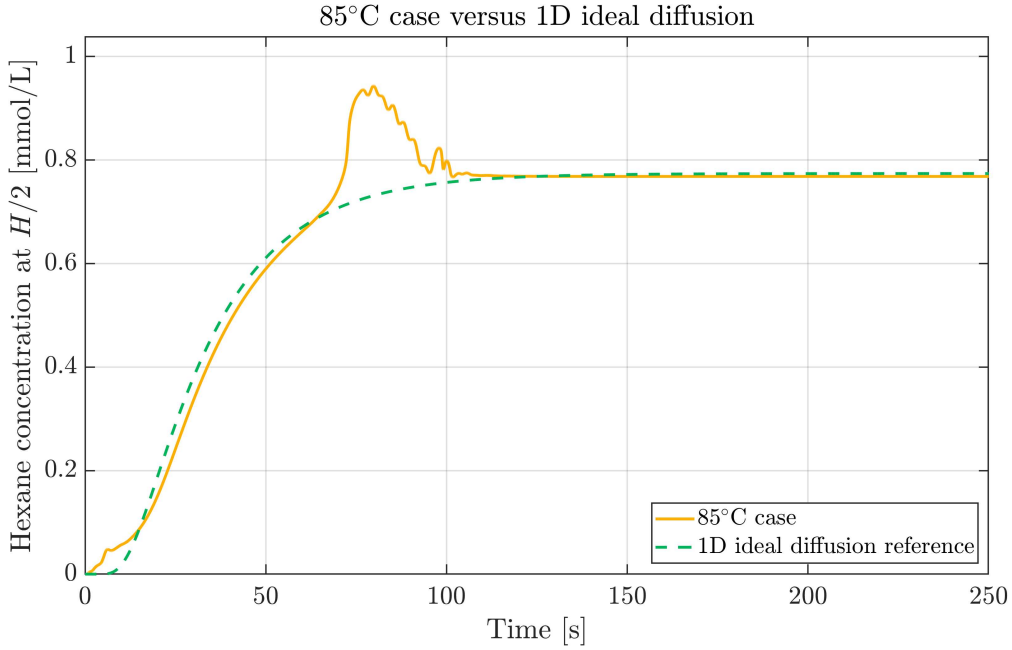



**Figure 18:** Computed line-averaged concentration evolution at $H/2$ for the reference case compared to the predictions of the 1D diffusion model.

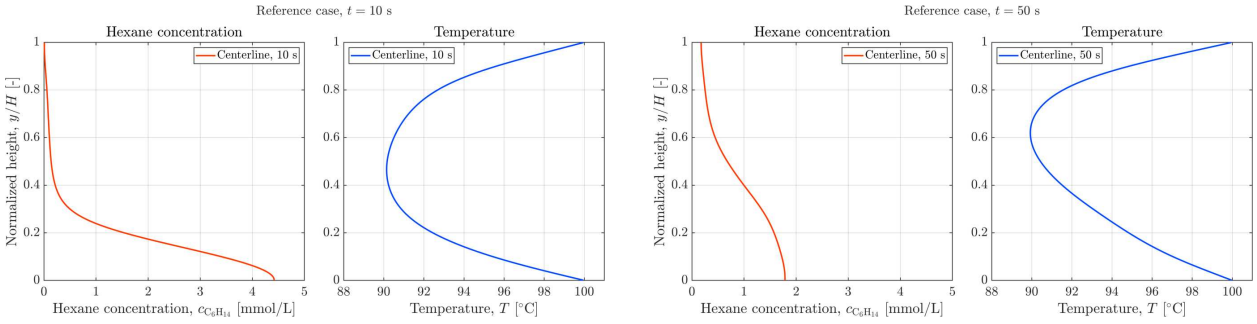
## 3.5 Reformation of Convection

After a certain period of diffusive mixing, circulation reappears in the cell, again driven by the wall thermal-deficit-induced buoyancy. These convection currents have the same morphology as the pre-injection ones, with two counter rotating cells and an oscillating central plume. This circulation enhances mixing, leading to a fully mixed environment.

The timing of convection onset can be explained by a competition mechanism between compositional- and thermal-induced density variations. For convection to occur, there must be an unstable local density inversion in the cell, where denser gas sits atop lighter gas and sinks, triggering the circulation. In our current case, density differences arise from composition and temperature differences. Pressure-induced density differences can be considered negligible; For $H = 0.1\,\mathrm{m}$, $p \approx 10^5\,\mathrm{Pa}$, and $\rho \approx 1\,\mathrm{kg\,m^{-3}}$, $\Delta p/p \sim \rho g H/p \approx 1.2 \times 10^{-5}$, whereas for the imposed 15 °C deficit, $\Delta T/T \sim 15/373 \approx 4.0 \times 10^{-2}$, roughly $3 \times 10^3$ times larger than the pressure contribution.

$$\rho = \frac{p\overline{M}}{R_u T} \qquad \Rightarrow \qquad \frac{1}{\rho}\frac{\partial \rho}{\partial z} = \frac{1}{p}\frac{\partial p}{\partial z} + \frac{1}{\overline{M}}\frac{\partial \overline{M}}{\partial z} - \frac{1}{T}\frac{\partial T}{\partial z} \tag{15}$$

The compositional contributions have a stabilizing effect, as the injected dense fuel vapor is located at the bottom of the flask and transitions into a lighter mixture that moves upward. The thermal contributions, on the other hand, have a destabilizing effect, as they cool gas near the walls, making it denser than the mixture below it and causing it to sink. The onset of convection is determined by which one of these two contributions dominates. Right after injection, the compositional-driven density distribution is highly stable, as very heavy fuel sits at the bottom of the flasks; thermal buoyancy-induced differences are not strong enough to create a region of sufficiently cool mixture to penetrate this stable stratification. As time progresses and diffusive mixing smears the compositional distribution, the system reaches a point where thermal buoyancy can generate an instability: a local density inversion. Circulation is then triggered. Figure 19 shows the evolution of the compositional and temperature fields along a vertical centerline in the domain for the reference case; it illustrates how the compositional stratification is smeared by diffusion over time.




**(a)** $t = 10\,\mathrm{s}$. **(b)** $t = 50\,\mathrm{s}$.

**Figure 19:** Evolution of the compositional and temperature fields along the vertical centerline, illustrating the smearing of the compositional stratification by diffusion over time.

## 3.6 Convection Morphology and Stabilization

After convection begins, a key point of interest is the convection stabilization process. After the initial local density inversion is triggered, two counter-rotating vortices are generated as cold gas falls along the side walls (1). The gas eventually reaches the bottom of the flask, where its momentum is redirected upwards, generating a central plume (2). The plume itself does not have enough inertia to penetrate the still-stratified field fully and instead turns back down, creating a region of two counter-rotating cells. This region rapidly mixes, creating two clearly delimited density regions in the cell: a fuel-rich, highly mixed bottom region, and an air-dominant, unmixed top region.

This environment leads to a very interesting oscillatory mechanism: as the plume penetrates the

stable stratification (3), it creates a perturbation (4). The buoyancy force restores this perturbation, but, like a spring restoring force, the fluid has downward momentum at the equilibrium point, creating a downward perturbation (5) and leading to an oscillatory overshoot cycle. Mixing due to advection and diffusion at the interface shifts the equilibrium point/interface of this system upward during each cycle, so that each cycle starts from a higher equilibrium height (6). A diagram of this process, overlaid on the evolution of the density field, is shown in Figure 20. The position of the interface over time, showing the oscillations and upward drift for the reference case, is shown in Figure 21.

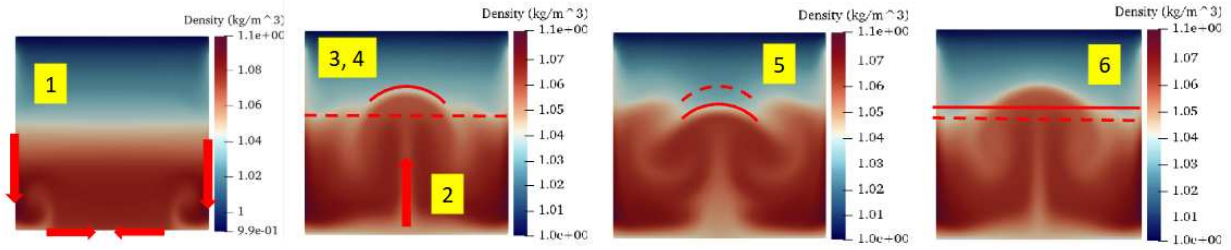



**Figure 20:** Oscillatory overshoot cycle illustrated over the evolution of the density field. The time interval between the first and last frames is $\Delta t = 10\,\mathrm{s}$.

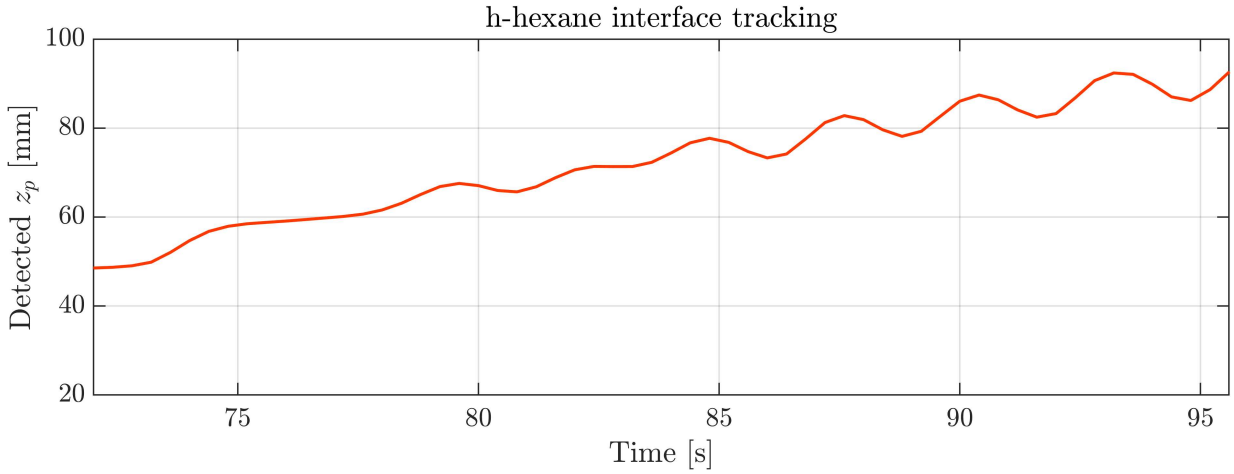



**Figure 21:** Position of the density interface over time, showing the oscillatory behavior and upward drift for the reference case.

The observed oscillations are similar to the well-documented phenomenon of internal waves in a stably stratified fluid.[13] The characteristic frequency of the simplified problem, where a parcel of fluid has a different density in a continuously stratified field, is called the Brunt-Vaisala frequency and can be calculated as

$$N = \sqrt{-\frac{g}{\rho_0}\frac{\partial \rho(z)}{\partial z}} \tag{16}$$

Table 4 shows that the frequencies estimated by the formula are in the same order of magnitude as those observed in the simulation, considering $\rho_0 = (\rho_b + \rho_t)/2$ and $\frac{\partial \rho}{\partial z} \sim -\frac{\rho_b - \rho_t}{\delta}$, where $\delta$ is the approximate interface size and $z$ increases upward. The measured frequencies from the simulation

are extracted from the inverse of peak-to-peak periods of the interface oscillations from Figure 21. Densities are sampled on both sides of the interface yielding $\Delta\rho = \rho_b - \rho_t = 0.025$–$0.027$ kg/m$^3$ and $\delta = 8.57$–$10.89$ mm.

| Interval [s] | Measured $f_{\text{sim}}$ [Hz] | B-V frequency $N/(2\pi)$ [Hz] |
|---|---|---|
| 87.60–90.40 | 0.357 | 0.772 |
| 90.40–93.20 | 0.357 | 0.819 |
| Cycle mean | 0.357 | 0.795 |

**Table 4:** Comparison of measured simulation frequencies and Brunt–Vaisala (B-V) frequency estimates for the n-hexane reference case

A more careful approach is to consider a box with two distinct stratified density regions, as in our problem. Under several simplifying assumptions and following the derivation of Appendix E.3, the characteristic frequencies for two layers of difference densities in a box are given by:

$$f_n = \frac{1}{2\pi}\sqrt{\frac{\frac{n\pi}{H}(\rho_b - \rho_t)g}{\rho_b \coth\left(\frac{n\pi h_b}{H}\right) + \rho_t \coth\left(\frac{n\pi h_t}{H}\right)}}. \tag{17}$$

where $n$ is the spatial mode number, $\rho_t$ and $\rho_b$ are the different densities of the top and bottom regions, $h_1$ and $h_2$ are the distances to the interface from the top and bottom walls respectively, and $H$ is the box height.

Using this new analysis, the analytical frequencies for mode 1 and 2 are much closer to those observed in the simulation. Table 5 compares oscillation frequencies between the simulation's reference case and the first and second modes of the new internal wave model using the same sampled data as for Table 4.

| Interval [s] | Measured $f_{\text{sim}}$ [Hz] | Model $f_1$ [Hz] | Model $f_2$ [Hz] |
|---|---|---|---|
| 87.60–90.40 | 0.357 | 0.236 | 0.400 |
| 90.40–93.20 | 0.357 | 0.208 | 0.366 |
| Cycle mean | 0.357 | 0.222 | 0.383 |

**Table 5:** Fundamental frequency ($n = 1$) and ($n = 2$) from the two-layer formula for n-hexane versus the measured simulation frequency.

The importance of the spatial aspect of the oscillatory mechanism is also highlighted in this model. Figure 22 plots the predicted frequency of the internal-wave model as a function of the wavenumber.

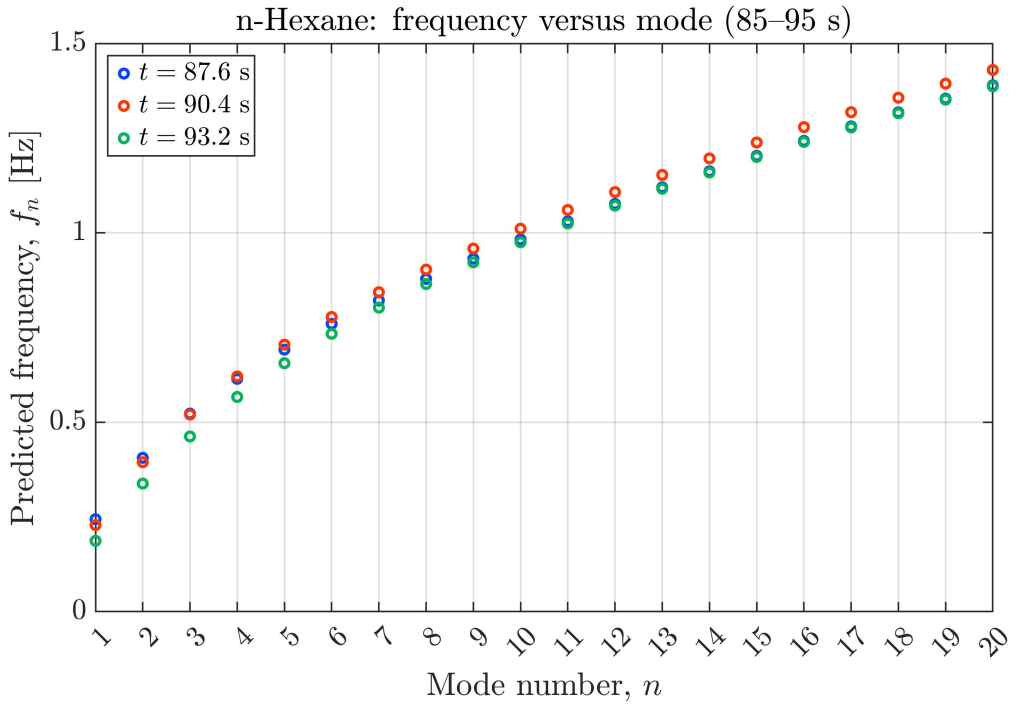
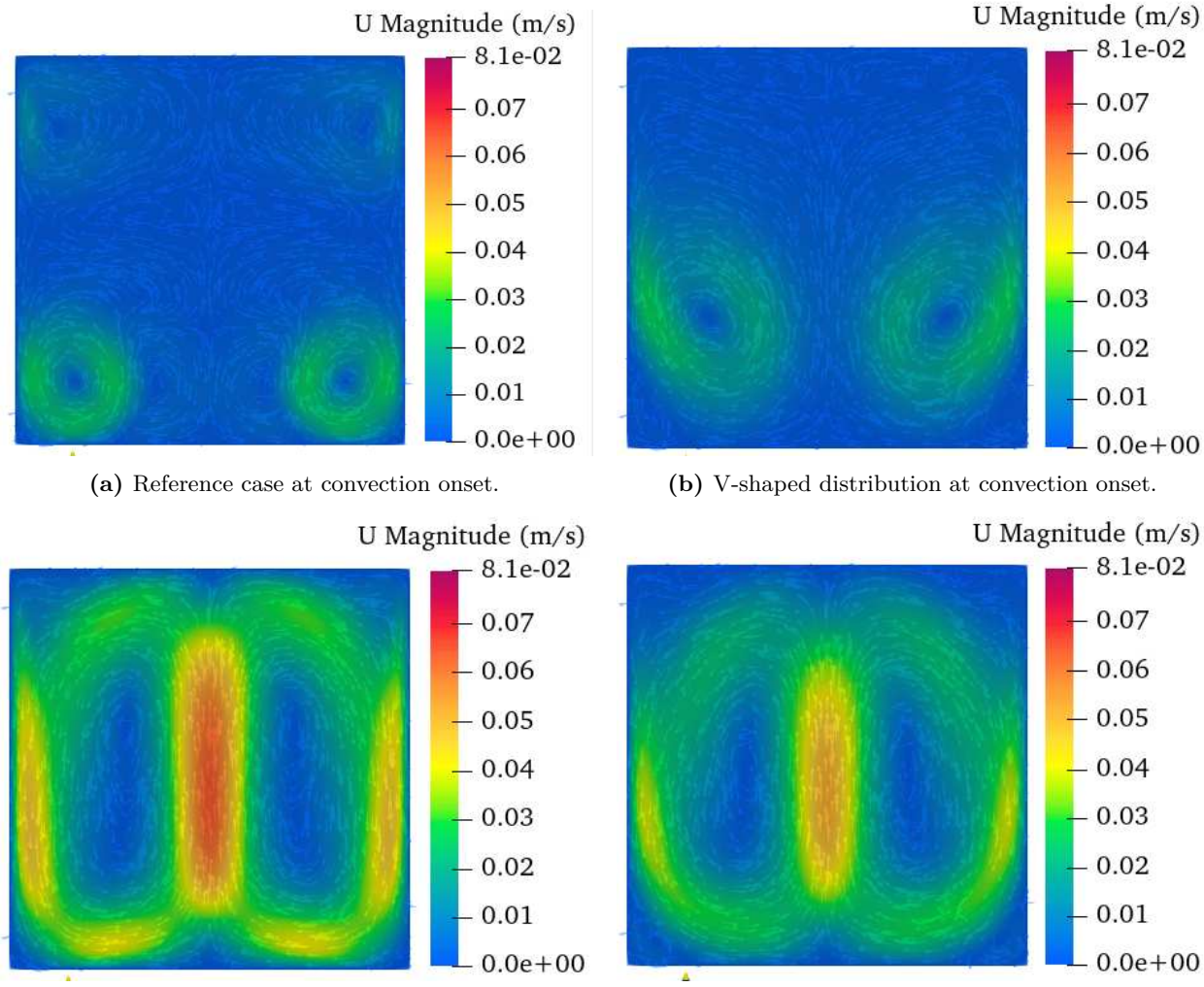



**Figure 22:** Predicted internal-wave frequency as a function of wavenumber for the n-hexane reference case.

In the context of the two-layer model, the frequency and shape of the observed perturbation can be represented as the superposition of all the distinct modes that compose it based on the initial perturbation shape. This oscillation is soundly based on the physics of stratified flow but is not observed experimentally in the concentration measurement. This may be due to inherent line-path averaging from the laser-absorption method used, 3D effects, and to the lower molecular-weight hydrocarbons tested, which have lower associated frequencies as shown in Section 6.

The exact morphology of the convection event varies from case to case due to differences in fuel properties and/or temperature conditions. Figure 23 shows an example of the difference between the circulation structures that may be formed for the reference case and a case with a different temperature boundary condition.




**(a)** Reference case at convection onset.

**(b)** V-shaped distribution at convection onset.

**(c)** Reference case during convection stabilization.

**(d)** V-shaped distribution during convection stabilization.

**Figure 23:** Comparison of the circulation structures at convection onset and convection stabilization for the reference case (a,c) and a different imposed V-shaped temperature distribution (b,d), detailed in Section 5.1.

The circulation formation process varies between cases; for example Figure 23 (a) has a pair of circular rotating vortices that arise from the bottom of the cell, while Figure 23 (b) shows the same pair coming from the middle of the side walls with a more oval distribution. Note that these convective structures evolve differently in terms of timing and shape over time.

The emphasis on these different circulation structures are important because they drive the shape of the concentration signal of interest. Both cases converge to a relatively similar double-circulation cell mode.

The explanation for why different circulation structures arise under different temperature boundary conditions lies in the mechanism of vorticity generation in buoyancy-driven flows. The vorticity transport equation is:

$$\frac{D\boldsymbol{\omega}}{Dt} = (\boldsymbol{\omega} \cdot \nabla)\mathbf{u} - (\nabla \cdot \mathbf{u})\boldsymbol{\omega} + \frac{\nabla\rho \times \nabla p}{\rho^2} + \nabla \times \left[\frac{1}{\rho}\nabla \cdot \boldsymbol{\tau}\right]. \tag{18}$$

where the baroclinic term

$$\frac{\nabla\rho \times \nabla p}{\rho^2} \tag{19}$$

can be simplified to

$$\frac{\nabla\rho \times \mathbf{g}}{\rho}. \tag{20}$$

For a gravity-dominated, near-hydrostatic field, $\nabla p \approx \rho\mathbf{g}$. Thus, vorticity and circulation are generated by the cross product of density and pressure gradients, i.e., by a misalignment of these gradients. Different temperature boundary condition profiles and fuel properties will induce different density variation profiles, as $\nabla\rho$ is related to $\nabla T$ and $\nabla Y$, and thus different circulation structures. This is the same mechanism that creates weather systems.[13]

### 3.7 Dynamic Similarity

Fouchier et al.[6] showed that a dimensional analysis of an analytic 1D diffusion model yielded a solution $c(t,z) = c^* f(Dt/H^2, z/H; \delta/H)$ where $f$ is a universal nondimensional function of the nondimensional variables. Using this idea, diffusive processes with different diffusivities arising from temperature or fuel selection, and with different initial concentrations were simulated by Fouchier et al.[6], demonstrating the validity of this non-dimensional scaling .

Applying this diffusion scaling to different cases across the simulations of the present work shows that the diffusive mixing process also collapses for $Dt/H^2 < 0.05$ against $\bar{c}/c^*$ across different fuels, temperatures, and injected volumes. This result supports the existence of a diffusion-dominated process for most cases. The exceptions will be covered in the following sections. Figure 24 shows the collapse of the concentration histories using the non-dimensional scaling for a variation of injected volume from the parametric study of Section 6.2.

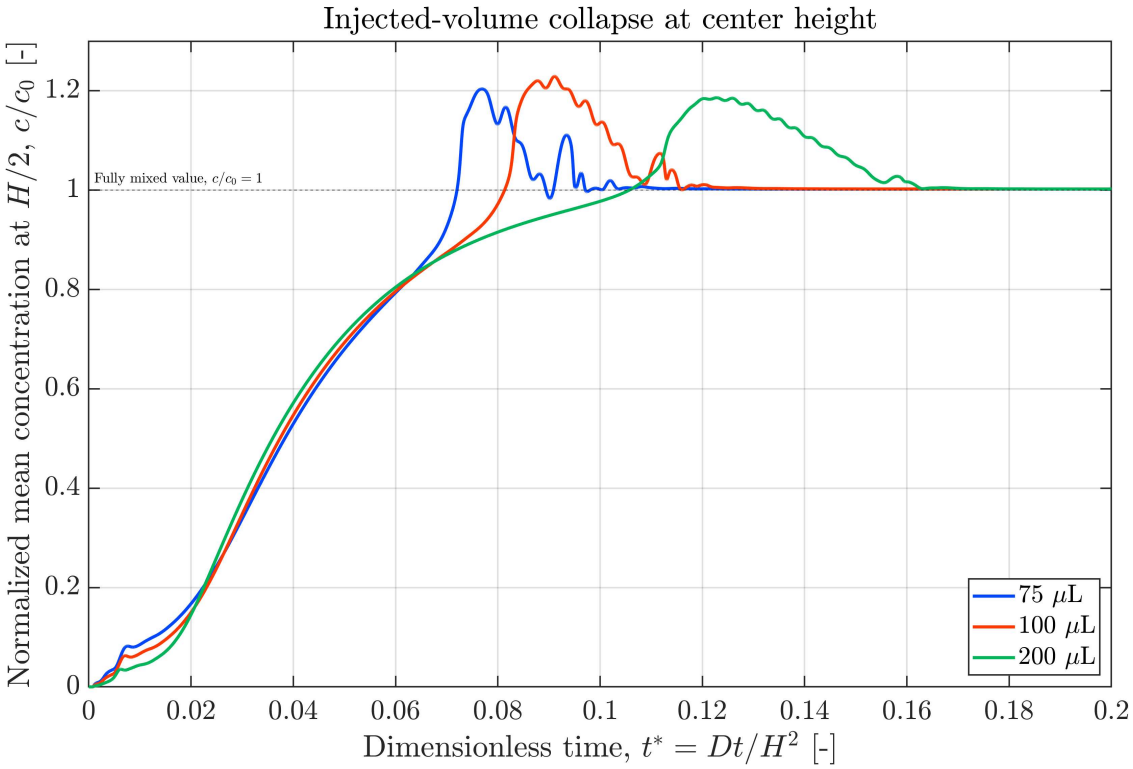



**Figure 24:** Collapse of the computed line-averaged mixing concentration histories prior to convection onset for different injected volumes using the non-dimensional scaling of Fouchier et al.[6]

This non-dimensional scaling also shows satisfactory results for the experiments in the present work with some exceptions, which will be covered in detail in their relevant sections. The convection onset time and the signal morphology do not collapse under this diffusive universal scaling, as expected, because multiple variables beyond diffusion drive the convection process.

To understand under what conditions the convection process will exhibit similar non-dimensional behavior, the momentum and species equations are derived in their non-dimensional forms. Following the non-dimensional groups and derivations used by Davis[14], the variables are defined as

$$\begin{aligned} t^* &= \frac{t\alpha_0}{L^2}, \qquad \nabla^* = L\nabla, \qquad \mathbf{u}^* = \frac{\mathbf{u}L}{\alpha_0}, \qquad p^* = \frac{pL^2}{\rho_0\alpha_0^2}, \\ \rho^* &= \frac{\rho}{\rho_0}, \qquad \Theta = \frac{T}{T_0}, \qquad \mu^* = \frac{\mu}{\mu_0}, \qquad D^* = \frac{D}{D_0}, \qquad Y_f^* = \frac{Y_f - Y_{f,0}}{\Delta Y_f}. \end{aligned} \tag{21}$$

where the superscript $^*$ represents a dimensionless quantity and the subscript 0 a reference value. The momentum equation becomes:

$$\rho^*\frac{\partial \mathbf{u}^*}{\partial t^*} + \rho^*\mathbf{u}^*\cdot\nabla^*\mathbf{u}^* = -\nabla^* p^* + Ra_0 Pr_0\,\mathbf{e}_g + Pr_0\left\{\mu^*\nabla^{*2}\mathbf{u}^* + \frac{\partial\mu^*}{\partial\Theta}(\nabla^*\Theta)\cdot\left[\nabla^*\mathbf{u}^* + (\nabla^*\mathbf{u}^*)^T\right]\right\}, \tag{22}$$

where Rayleigh and Prandtl numbers are

$$Ra = \frac{\Delta\rho L^3 g}{\mu\alpha}, \qquad Pr = \frac{\nu}{\alpha} = \frac{\mu}{\rho\alpha}. \tag{23}$$

The species equation post-vaporization (no source term), becomes:

$$\rho^* \left( \frac{\partial Y_f^*}{\partial t^*} + \mathbf{u}^* \cdot \nabla^* Y_f^* \right) = \frac{1}{Le_0} \nabla^* \cdot \left( \rho^* D^* \nabla^* Y_f^* \right) , \tag{24}$$

where the Lewis number is

$$Le = \frac{\alpha}{D}. \tag{25}$$

It can be seen from the non-dimensional momentum equation that the $Ra$ and $Pr$ numbers are critical parameters affecting buoyancy-driven flow, and similarly that the $Le$ number is a critical parameter affecting species transport for the coupled buoyancy and species-transport problem. In addition, property variations driven by large temperature differences will affect the flow independently of the non-dimensional numbers. For cases to be dynamically similar, these non-dimensional groups must be matched, in addition to having the same non-dimensional boundary and initial conditions and similar property changes.

Density differences in the current work arise from changes in composition and temperature; however, it is not possible to infer directly from the Rayleigh number whether the characteristic density difference $\Delta\rho$ arises from either one. First-order relative density differences driven by composition and temperature[15] are often computed by linearizing under the Boussinesq approximation.

$$\frac{|\Delta\rho_T|}{\rho_0} \sim \beta_T \Delta T, \qquad \text{and} \qquad \frac{|\Delta\rho_Y|}{\rho_0} \sim \beta_Y \Delta Y_f \, , \tag{26}$$

where, for an ideal fuel–air mixture around pure air,

$$\beta_T = \frac{1}{T_0}, \qquad \beta_Y = 1 - \frac{W_{\text{air}}}{W_f}, \tag{27}$$

and

$$R_\rho = \frac{|\Delta\rho_T|}{|\Delta\rho_Y|} \sim \frac{\beta_T \Delta T}{\beta_Y \Delta Y_f} = \frac{\Delta T / T_0}{\left( 1 - \dfrac{W_{\text{air}}}{W_f} \right) \Delta Y_f} \, , \tag{28}$$

which represents a non-dimensional, thermal vs. compositional, density-variation parameter. If $R_\rho > 1$, the characteristic thermal density difference exceeds the compositional component; if $R_\rho < 1$, the opposite happens. Different temperatures, concentrations, and fuel selections will initially alter this parameter, leading to different thermal versus compositional balances across cases. This may modify the Rayleigh number and generate different convection dynamics. In addition, it is expected that for otherwise comparable cases, cases with higher $R_\rho$ will exhibit an earlier convection onset, as the thermally destabilizing variations will overcome the compositionally stabilizing variations

sooner.

From this analysis, complete dynamic similarity is not generally expected among the cases considered here, as changes in case temperature, injection volume, and fuel selection modify several of the quantities that must be matched: $Ra$, $Pr$, $Le$, property variations, and non-dimensional initial and boundary conditions.

### 3.8 Role of Three-Dimensional Effects

The role of three-dimensional effects could not be definitely established in the present study, as grid independence has not been demonstrated due to the limitations of computing resources. Discussion and preliminary results of the 3D simulations are given in Appendix C. It is hypothesized that the thermal buoyancy provided by different walls may play a superimposed effect, accelerating the onset of convection. There may also be asymmetries in the flow that are not captured by the current 2D setup.

## 4 Sensitivity to Vaporization Characteristics

The first sensitivity analysis focuses on investigating the effect of both the spatial and temporal aspects of the vaporization event, as different vaporization regimes may exhibit different characteristics. For example, Leidenfrost vaporization will have a broader effective vaporization region, as droplets quickly disperse across the entire floor of the flask. In contrast, a boiling case will have a much more localized region at the puddle interface. Different vaporization regimes may also exhibit different temporal shapes, with vaporization time decreasing as temperature increases until $T_{\mathrm{LDF}}$,where the temperature difference between the flask bottom and the droplet is sufficiently high that a thin film of hexane vapor forms, reducing heat transfer and increasing vaporization time. The current study focuses on rapid vaporization processes above $T_{\mathrm{boiling}}$, which are almost all for the relevant fuels near their AITs. Consideration of slower vaporization processes, including condensation mechanisms, will be included in Section 4.4.

The parametric studies in Section 4 made modifications based on the reference case indicated in Table 6. Figure 25 shows the imposed temperature boundary condition distribution.

| **Parameter** | **Reference value** |
|---|---|
| Fuel | Hexane |
| Case temperature | 100 °C |
| Temperature boundary conditions | 10 °C linear deficit |
| Injected volume | 100 $\mu$L |
| Vaporization duration | 5 s |
| Vaporization shape | 50 mm × 5 mm at the bottom center |

**Table 6:** Reference case for parametric studies on vaporization.

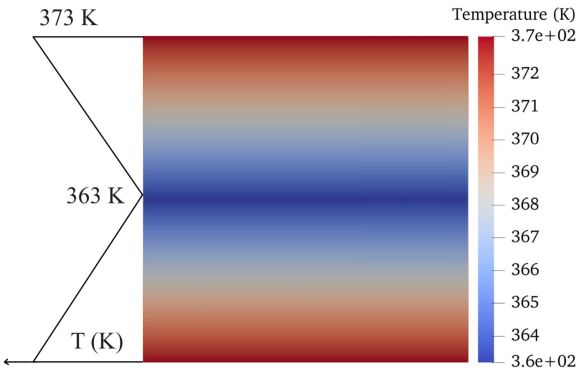



**Figure 25:** Imposed V-shaped 10 °C deficit wall temperature distribution.

## 4.1 Spatial Source Distribution

We first studied the variation of the shape of an instantaneously initialized hexane cloud. This injection approach differs from the standard one used in the current work explained in Section 3.3.

To correctly preserve the injected amount of hexane (100 µL), the area of the initialized region in the 2D domain was adjusted to represent the equivalent area that would be occupied by hexane vapor at 100 °C.

Calculating the injected mass:

$$m = 0.1\,\text{mL} \times 0.655\,\text{g/mL} = 0.0655\,\text{g}.$$

Calculating the injected moles ($n$):

$$n = \frac{0.0655\,\text{g}}{86.18\,\text{g/mol}} \approx 0.00076\,\text{mol}.$$

Calculating the injected volume:

$$V = \frac{nRT}{P} = \frac{0.00076\,\text{mol} \times 0.0821\,\text{L atm/(mol K)} \times 373.15\,\text{K}}{1\,\text{atm}} \approx 0.0233\,\text{L}.$$

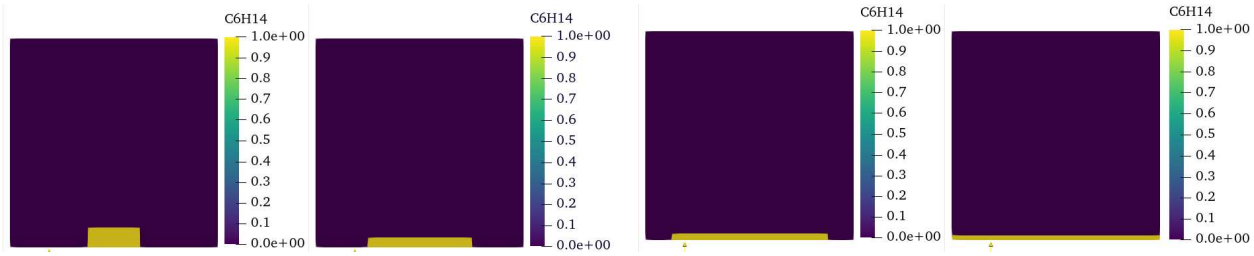
Finally, the equivalent area for a fixed width of the third dimension of 0.1 m:

$$V = WA, \qquad A = \frac{V}{W} = \frac{0.0233 \times 10^{-3}\,\text{m}^3}{0.1\,\text{m}} = 2.33 \times 10^{-4}\,\text{m}^2.$$

In the study, the cloud was shrunk in width and increased in height, keeping the total area, proportional to total amount of initialized gas, constant. The case matrix included 4 variants. The rest of the simulation parameters were kept equal to the baseline case explained in Table 6. Table 7 summarizes the instantaneous initialization case matrix. Figure 26 shows the different initialization clouds used in the simulations.

| Case | Length (m) | Height (m) |
|---|---|---|
| A | 0.025 m | 0.009 48 m |
| B | 0.050 m | 0.004 74 m |
| C | 0.075 m | 0.003 16 m |
| D | 0.100 m | 0.002 37 m |

**Table 7:** Instantaneous initialization cloud dimensions.




**(a)** Cases A and B. **(b)** Cases C and D.

**Figure 26:** Instantaneous initialization hexane cloud geometries represented as mass-fraction zones of $Y_f = 1$.

No significant sensitivity of the solution to the initialization shape was observed. In all cases, fuel sinks due to buoyancy, disrupts the pre-injection flow field, and subsequently disperses through diffusion until the convection cells reform at almost the same time. There is also no significant difference between the cases near the vaporization event, in the first seconds of the simulation. Results still vary greatly from the experimentally reported bump, due to the choice of temperature boundary condition. Figure 27 compares the four spatial sensitivity cases with the experimental data. Figure 28 shows the evolution of the fuel mass fraction at $t + 20\,\mathrm{s}$ after injection, with no visible differences among the cases.

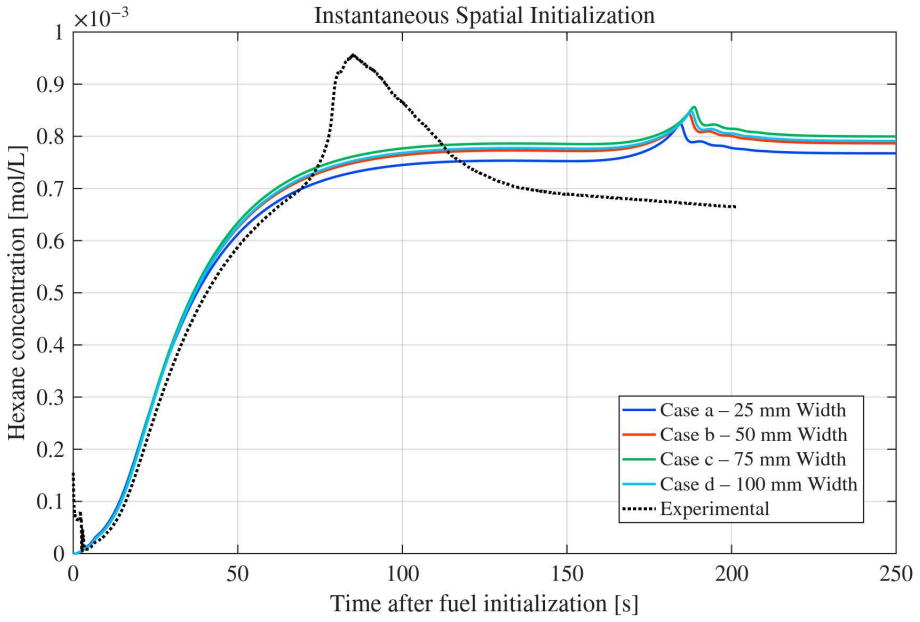
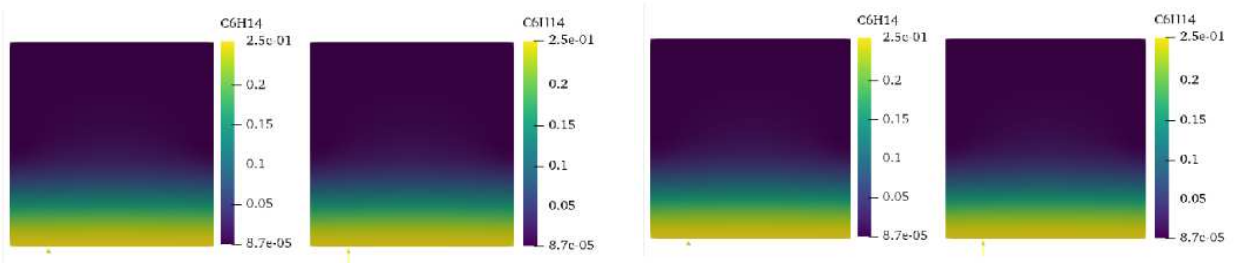



**Figure 27:** Comparison of the computed line-averaged concentration for the four spatial sensitivity cases and the experimental data, shown as a black dotted line.




**(a)** Cases A and B at $t + 20\,\mathrm{s}$. **(b)** Cases C and D at $t + 20\,\mathrm{s}$.

**Figure 28:** Fuel mass-fraction fields for cases A–D at $t + 20\,\mathrm{s}$ after injection.

The small difference among cases observed in Figure 27 stems from the discretization of the computational volume. The prescribed areas do not fall perfectly at the interface between cells, slightly altering the discrete cell volume where hexane is initialized and creating small differences in the total amount of hexane initialized between cases. It is important to restate, however, that the overall morphology and magnitude of the convective bump across all cases is maintained.

To confirm that the spatial shape of the vaporization process does not have a significant effect on the convection onset process, another parametric study modifying the spatial shape was conducted, this time using the standard temporal mass source initialization explained in Section 2.6.

The mass source allows for prescribing a fuel vapor mass source rate in the simulation. The shape of this mass source was varied between cases. Specifically, the case matrix included 4 different widths: 25, 50, 75, and 100 mm at a constant height of 5 mm. Table 8 specifies the cloud dimensions used in the study:

| Case | Length (m) | Height (m) |
|---|---|---|
| A | 0.025 m | 0.005 m |
| B | 0.050 m | 0.005 m |
| C | 0.075 m | 0.005 m |
| D | 0.100 m | 0.005 m |

**Table 8:** Temporal mass-source initialization cloud dimensions.

The spatial height of the vaporization cloud was estimated by measuring the height of the high-density region in BOS images. The injection duration of 5 s was estimated from direct images of the vaporization event for the 100 °C, 100 µL case, by observing when no more liquid fuel is visible.

Additional changes were also implemented for the study; hexane is now injected at its corresponding vaporization temperature at 1 atm, 341.9 K. The rest of the parameters in the simulation remain equal to the reference case explained in Table 6.

Again, no discernible change among the cases was observed. The convection signature of all cases is the same. The initial transient is also nearly identical. Results still vary greatly from the experimentally reported bump because of the chosen temperature boundary condition. The discretization issue mentioned in Section 4.1 is no longer present, as the vapor mass is now prescribed directly by the source rather than indirectly by the initialized shape. Figure 29 highlights the near-perfect similarity among the concentration signatures for all cases and their comparison with the experimental data.

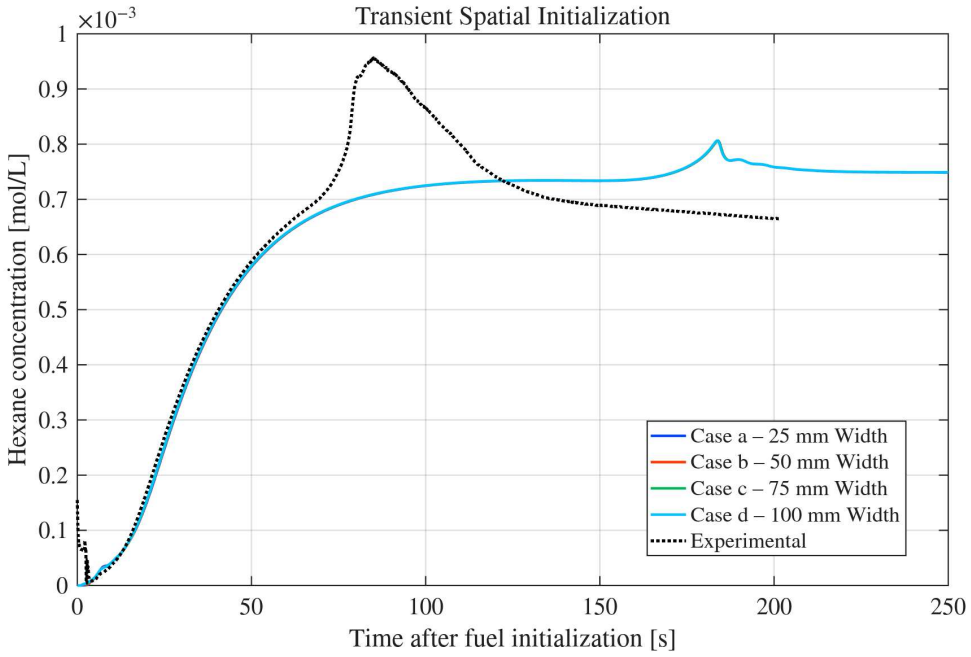



**Figure 29:** Comparison of the computed line-averaged concentration for the four transient spatial sensitivity cases and the experimental data, shown as a black dotted line. Note that cases A–D overlap, making only case D appear visible.

The main conclusion from these two studies is that, at least at the current level of model detail, the spatial shape of the vaporization event has no significant effect on the subsequent convection mode formation. It is also important to mention that the current study has not included any droplet dynamics modeling, a potentially relevant spatial phenomenon.

## 4.2 Vaporization Duration

The following sensitivity study aimed to understand the effect of the temporal aspect of the vaporization process. To do so, the duration of the mass source was varied among cases to cover a wide range of times. The case matrix included 5 cases, with simulated injection times of: 5 s, 7.5 s, 10 s, 15 s, 20 s. The rest of the parameters of the simulation were kept equal to that of the reference case indicated in Table 6.

| Case | Mass Source Duration (s) |
|---|---|
| A | 5 |
| B | 7.5 |
| C | 10 |
| E | 15 |
| F | 20 |

**Table 9:** Temporal mass source initialization time.

Two major conclusions were drawn from the study: slower injection postpones the formation of the convective bump by a few seconds, as it delays the fuel addition process and the subsequent

development of the diffusive period. Secondly, no major effect on the shape and magnitude of the convection was reported. Results still vary greatly from the experimentally reported bump because of the choice of temperature boundary condition. Note that the shorter vaporization time (5 s) seems to match more closely the initial diffusion stages. This is consistent with the approximate vaporization time extracted from the 100 °C, 100 µL case which is also on the order of 5 s estimated from imaging. Figure 30 compares the computed line-averaged concentration for the different injection-duration cases with the experimental data.

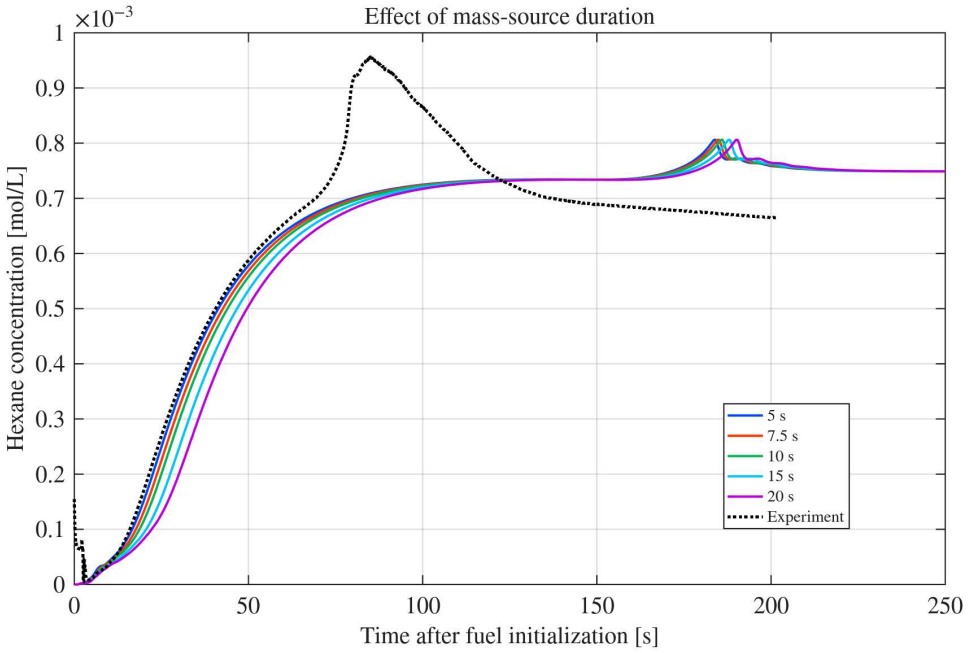



**Figure 30:** Comparison of the computed line-averaged concentration for the five injection-duration cases and the experimental data, shown as a black dotted line.

Overall, at least for the current level of detail of the model, the temporal shape of the vaporization event for rapid vaporization processes has no significant effect on the subsequent convective mode formation for rapid vaporization cases.

## 4.3 Vaporization-Cooling Sensitivity

Finally, a simplified analysis was done to evaluate the effect of vaporization cooling on the pre-ignition field. As vaporization occurs, the surrounding gas has to supply a considerable amount of heat to the hexane liquid, effectively cooling it. This phenomenon is experimentally observed in thermocouple measurements. Cooling could induce density variations in the field that could alter subsequent convective effects.

To analyze the event, gas was initialized at 20 °C temperature to induce effective cooling in the flask and preliminarily analyze its effect. The rest of the initialization parameters were kept constant in accordance with the reference case indicated in Table 6.

Note that the amount of cooling induced represents only approximately 33% of the total cooling, as we are omitting the large latent cooling contribution. Still, it serves as a first reduced-complexity

approximation of the potential effects.

$$\frac{Q_{\text{sens}}}{Q_{\text{tot}}} \times 100 = \frac{7.34 + 3.69}{32.97} \times 100 \approx 33\%. \tag{29}$$

No discernible effect was seen between cases, with both the 100 °C and 20 °C cases reporting the same concentration signatures. No difference was observed when examining the injection event either. Figure 31 compares the computed line-averaged concentration for the two initial fuel-temperature cases with the experimental data.

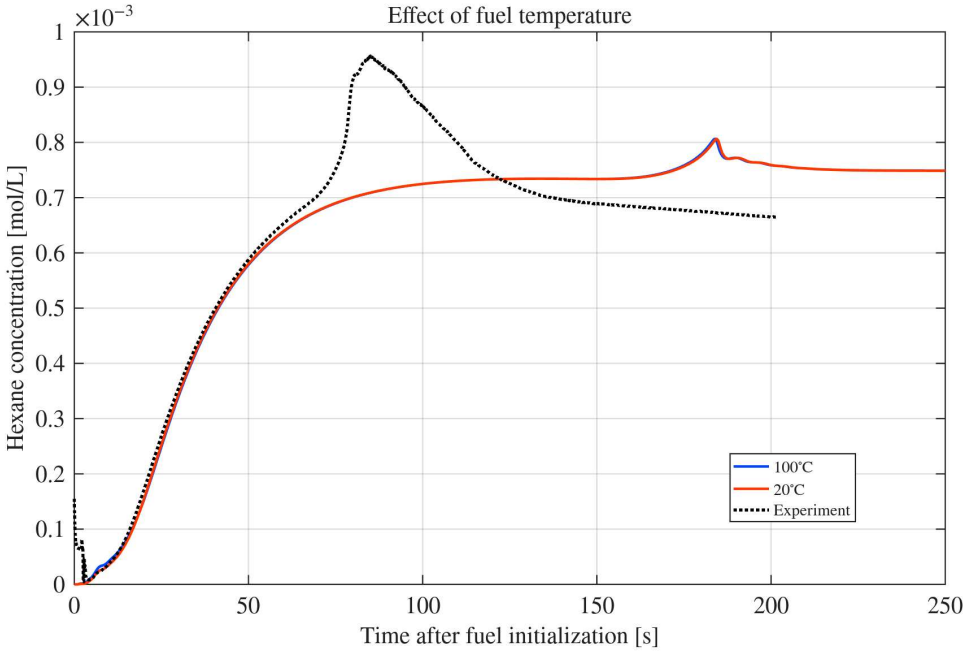



**Figure 31:** Comparison of the computed line-averaged concentration for the two initial fuel-temperature cases and the experimental data, shown as a black dotted line.

The negligible effect is consistent with the compositional buoyancy being significantly stronger than the thermal perturbation, with both having the same effect: sinking the fuel vapor. Another factor may be the treatment of the wall boundary conditions. They have constant values and thus can supply heat indefinitely without affecting the temperature along them, so a physical gas-wall interaction, which could change the boundary conditions, is not modeled. Experimental efforts were conducted to analyze these potential effects and will be explained in Section 4.4.

## 4.4 Additional Vaporization-Driven Mixing Phenomena

In addition to the computational studies, we ran a series of experiments to examine the role of gas-wall cooling interactions and the effects of vaporization at temperatures below the boiling point.

We injected 300 $\mu$L of hexane to increase the total heat required for vaporization to investigate the thermocouple response, among other things. The wall thermocouples and the top and bottom thermocouple showed no significant temperature drop. The center thermocouple, $T_{\text{cell}}$, placed near the injection pipe, showed a rapid drop and recovery during injection. Figure 32 shows the

temperature evolution of the N-S walls, E-W walls, and $T_{\text{top}}$, $T_{\text{bot}}$, and $T_{\text{cell}}$ thermocouples. An accurate description of the self-adhesive thermocouple setup is given in Section 2.1. Continuing the discussion from Section 4.3, it is concluded that the gas-wall cooling interaction has no significant effect on the temperature boundary conditions and subsequent convection.

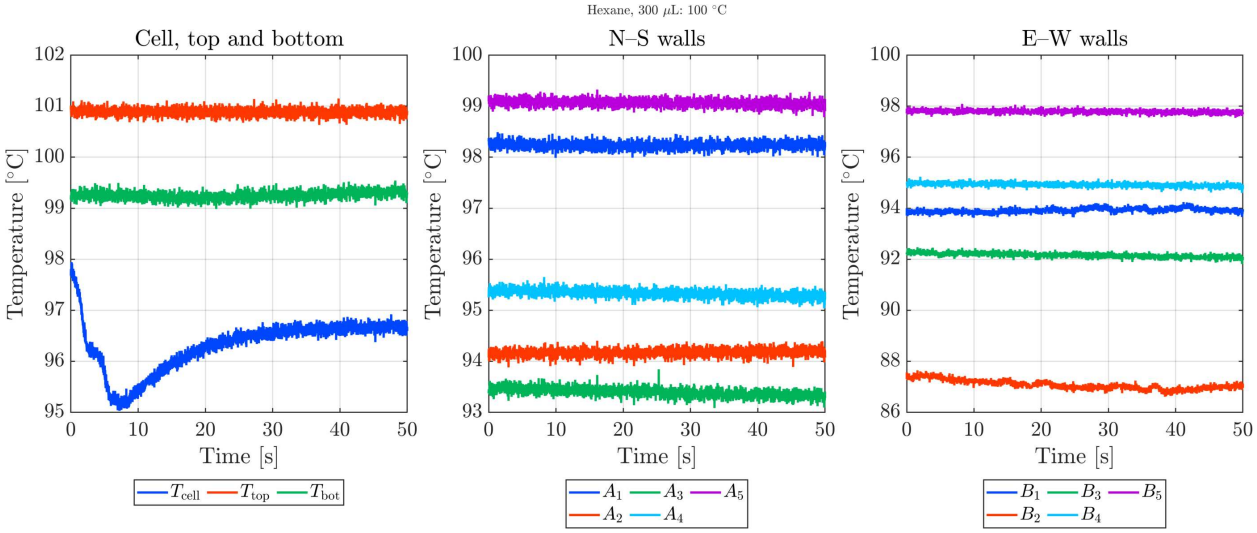



**Figure 32:** Temperature evolution of the N-S and E-W wall thermocouples and the $T_{\text{top}}$, $T_{\text{bot}}$, and $T_{\text{cell}}$ thermocouples following the injection of 300 $\mu$L of hexane.

More experiments were conducted to analyze the effects of vaporization processes below the boiling temperature. Figure 33 portrays the difference in mixing using nondimensional variables. Fuels (pentane, hexane, and heptane) have $T > T_{\text{boiling}}$ and show good agreement with the diffusive scaling prior to convection onset. Fuels like octane and dodecane have $T < T_{\text{boiling}}$ and the partial pressure of the fuel can exceed its saturation vapor pressure locally at the walls, causing some of the fuel to condense and altering the diffusive process. The amount of condensation increases as the boiling point increases and the saturation vapor pressure decreases. The observed differences from the purely diffusive process in the concentration histories are consistent with this trend. At a case temperature of $100°C$, a fuel such as octane, which has a boiling temperature of 125.6 °C, shows modest deviations from the diffusive scaling and dodecane, which has a boiling point of 216 °C exhibits extremely large deviations.

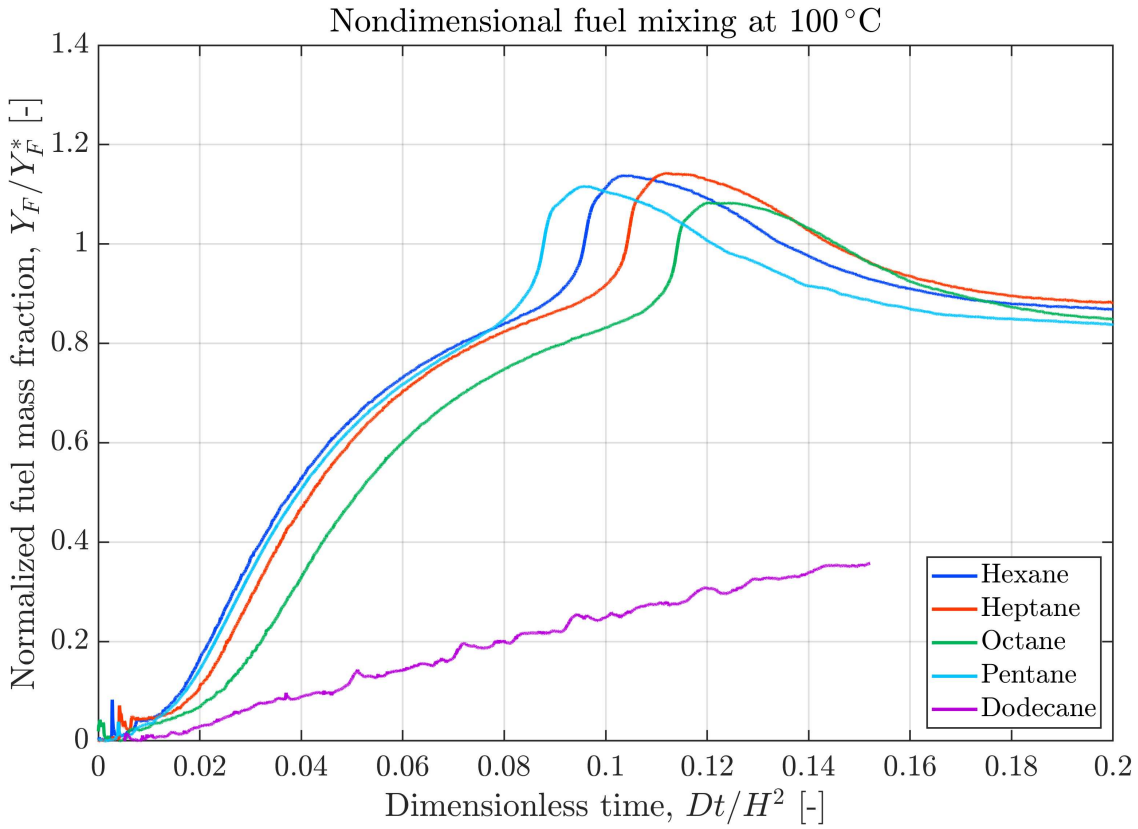



**Figure 33:** Analysis of measured line-averaged fuel concentration at $H/2$ location and a case temperature of 100 °C using non-dimensional variables. Hexane, heptane, and pentane have boiling points lower than 100 °C; octane and dodecane have higher boiling points.

This diffusive imbalance is seen to alter the formation of the circulation, as it includes additional vaporization and condensation processes at the walls. Its effect on the convection signal is yet to be understood and lies outside the scope of the report. These effects may be relevant for AIT measurements if a fuels' AIT is comparable to or less than $T_{\text{boiling}}$. The effect of fuel vapor pressure is quite important to other types of flammable atmosphere evaluation, such as the flash point testing.

A final, additional question concerns the effect of vaporization on lighter fuels, where the initial buoyant effect might not be as strong as for the cases examined in the current study. However, this question falls outside the scope of the present project, as most fuels of interest, such as Jet-A and SPK, exhibit even higher average molecular weight, around $160 \pm 10$ g mol$^{-1}$, varying from specific mixture to mixture, compared to hexane's 86.18 g mol$^{-1}$.

## 4.5 Conclusions

From the previously presented studies, it is concluded that, at least at the current level of simplification, differences in the vaporization process, including its spatial and temporal effects, have little effect on the subsequent convective mode for rapid vaporization cases above $T_{\text{boiling}}$.

All cases lead to the same stratified, hexane-rich field at the bottom of the flask. The injection event can therefore be considered as almost independent of the later convection, with any initial transient rapidly decaying due to the strong buoyant forcing mechanism. This conclusion is consistent with

what has been observed experimentally[6] where the rich fuel also stratifies in the bottom of the flask within the first few seconds after injection.

# 5 Sensitivity to Thermal Conditions

The next batch of studies focuses on the effect of thermal conditions on the mixing mechanism in the cell. It is expected that the mixing will be sensitive to temperature changes due to the thermal-buoyancy nature of the driving mechanism. The studies focus on changes to and experimental characterization of, the temperature boundary conditions. The reference case for these studies is described in Table 10. The reference temperature boundary condition is shown in Figure 34.

| **Parameter** | **Reference value** |
|---|---|
| Fuel | Hexane |
| Case temperature | 100 °C |
| Temperature boundary conditions | 10 °C linear deficit |
| Injected volume | 100 $\mu$L |
| Vaporization duration | 5 s |
| Vaporization shape | 50 mm × 5 mm at the bottom center |

**Table 10:** Reference case for parametric studies on thermal effects.

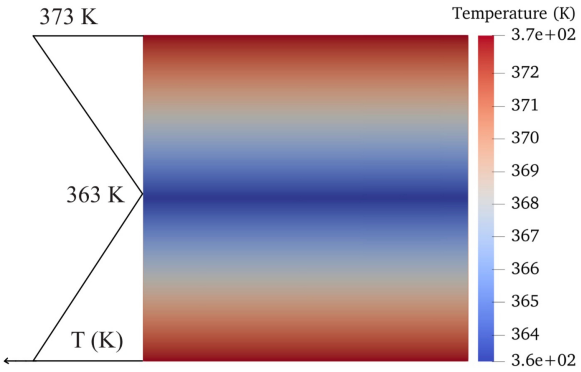



**Figure 34:** Imposed V-shaped 10 °C deficit wall temperature distribution.

## 5.1 Temperature-Profile Distribution

The first study focused on the spatial distribution of the temperature boundary condition. To do so, the position of the reference 10 K deficit was moved down while keeping the distribution linear to the top and bottom walls. Figure 35 shows the temperature boundary-condition distributions used in the study. The study matrix comprised three heights: $H/2$ (the reference case), $3H/8$, and $H/4$. Table 11 shows the case matrix.

| Case | Coldest-point position, $y/H$ |
|---|---|
| Reference | 1/2 |
| A | 3/8 |
| B | 1/4 |

**Table 11:** Case matrix for the temperature boundary-condition distribution study.

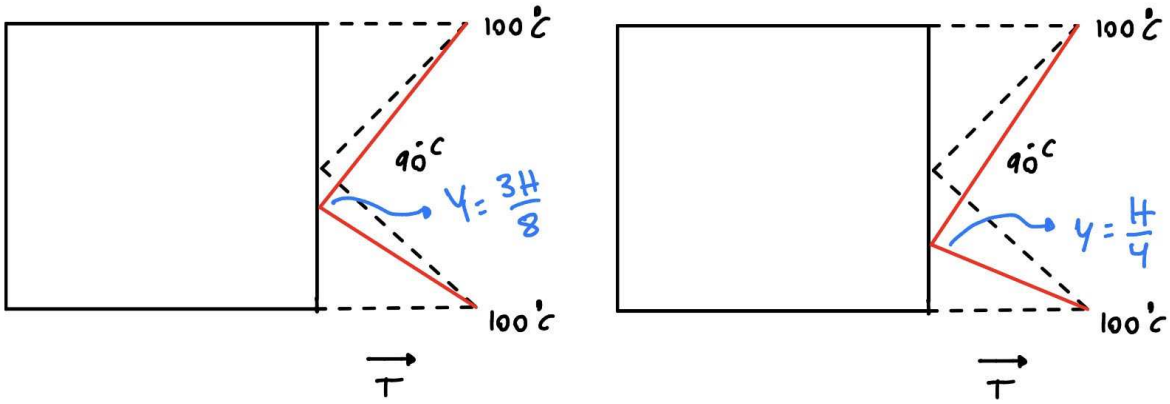



**Figure 35:** Case A and B boundary-condition distributions evaluated in the sensitivity study, with the 10 K deficit located at $3H/8$ and $H/4$

The mixing process is very sensitive to changes in the distribution of the temperature boundary condition. Table 12 summarizes the characteristic convection timings for each case. Figure 36 compares the computed line-averaged concentration for the three temperature-distribution cases with the experimental data.

| Metric | $H/2$ (Reference) | $3H/8$ | $H/4$ |
|---|---|---|---|
| Convection onset [s] | 173.35 | 153.60 | 123.75 |
| Onset-to-stabilization time [s] | 49.50 | 61.75 | 84.00 |

**Table 12:** Characteristic convection timings for the temperature-distribution sensitivity cases.

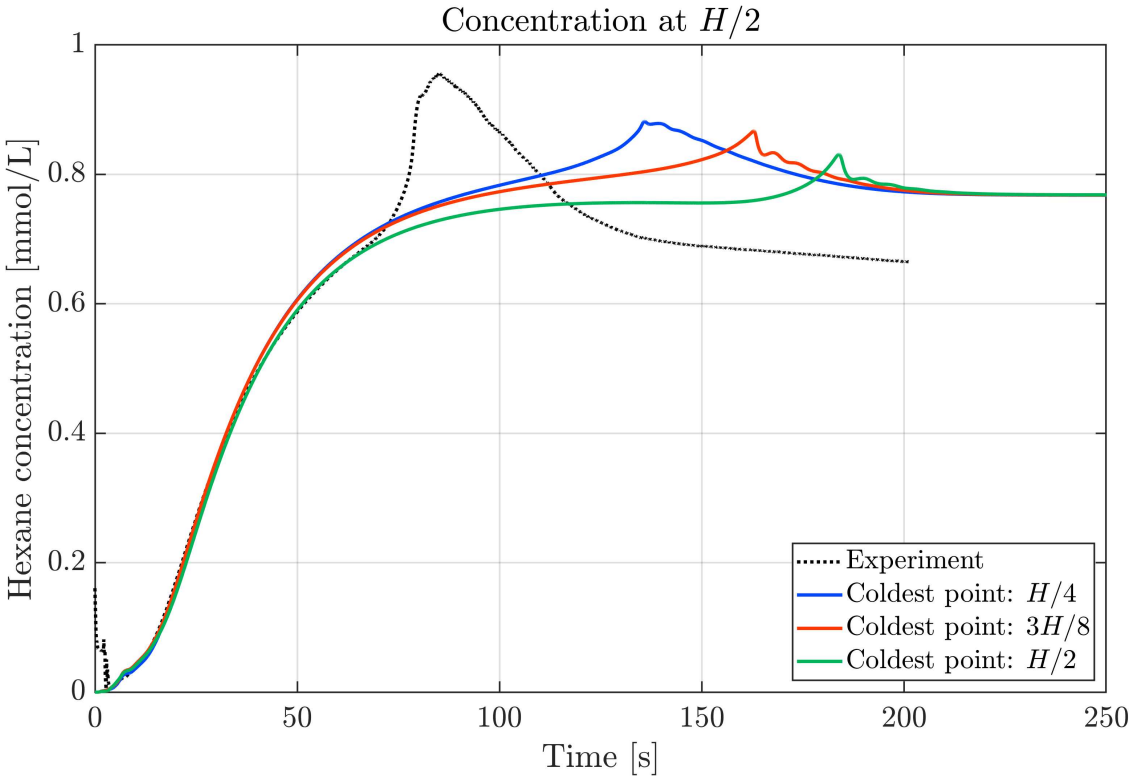



**Figure 36:** Comparison of the computed line-averaged concentration for the three temperature-distribution cases and the experimental data.

The results are quite revealing. The simple H/8 shifts of the cold source greatly affect the shape of the convection event. As the cold source is shifted downwards, convection appears sooner, as can be seen in Table 12. In contrast, the convection stabilization time increases as the position of the cold source decreases. Both trends are consistent with the mechanism explained in Section 3.5. As the cold source is moved down, thermal buoyancy locally overcomes compositional stabilization sooner because the composition field at lower heights evolves earlier as the initial vapor layer diffuses upward. In addition, because the circulation cells form in a less-mixed environment as they appear earlier, it takes longer for the interface between the circulation-enhanced well-mixed region and the unmixed mixture to smear down and drift upwards.

Comparing the results with the experimental data, moving the coldest spot downward makes the concentration signal closer to the experimental curve, with a smoother and earlier bump than in the baseline case at $H/2$. This could indicate that some additional heat loss is occurring near the bottom of the cell.

Figure 37 shows the temporal evolution of the velocity-magnitude profile along the vertical centerline of the domain.

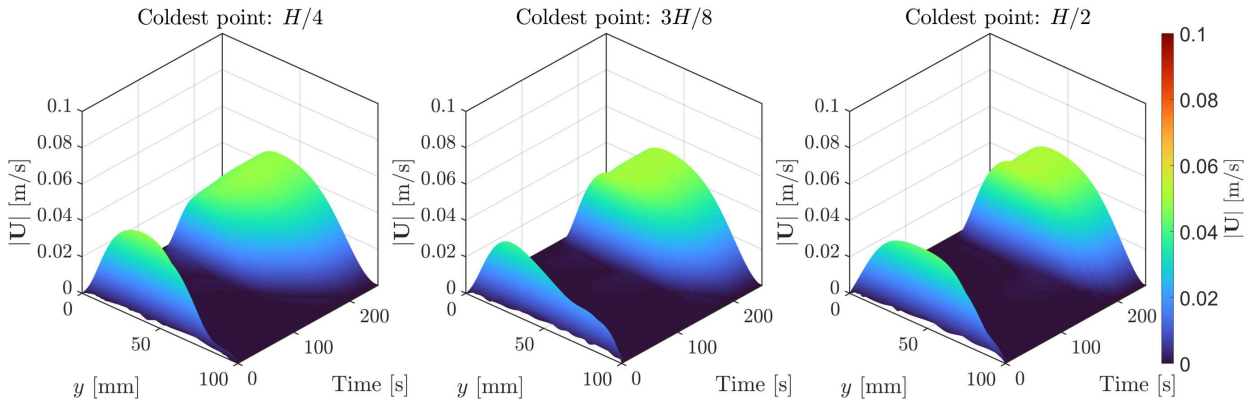



**Figure 37:** Temporal evolution of the velocity-magnitude profile along the vertical centerline for the three temperature-distribution cases.

From Figure 37, it is also visible what was already mentioned in Section 3.3: the total disruption of convection after injection. The graphs also show an earlier, smoother onset of convection for cases H/4 and 3H/8 compared with H/2. This observation is also supported by Figure 38, which shows the evolution of the kinetic energy per unit depth in the domain as a function of time, with the convection onset and stabilization marked by black and red symbols based on the criterion established in Section 2.7. In addition, Figure 38 also shows that the overall domain kinetic energy decreases as the coldest point is moved downward. This is consistent because the cold air has less height to acquire downward momentum due to buoyancy.

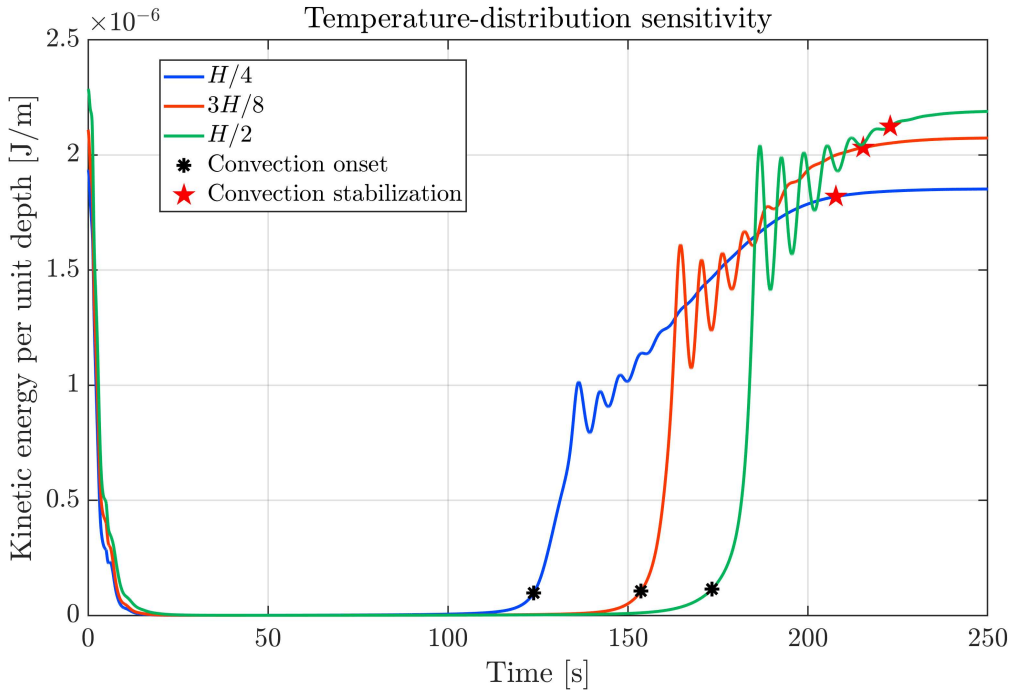



**Figure 38:** Evolution of the total kinetic energy per unit depth in the computational domain as a function of time for the three wall-temperature distributions.

## 5.2 Temperature-Profile Magnitude

The second study focused on the overall magnitude of the temperature boundary condition. Note that, to enhance the differences, this study implemented a new temperature distribution with a constant-temperature region, which will also be analyzed on its own. This temperature distribution imposed a constant temperature over [H/10, 9H/10] and a linear transition from that value to the top and bottom 100 °C heated plates to ensure temperature continuity. This was also the reference boundary condition used in Section 3.1. Figure 39 shows the type of boundary condition used in the study.

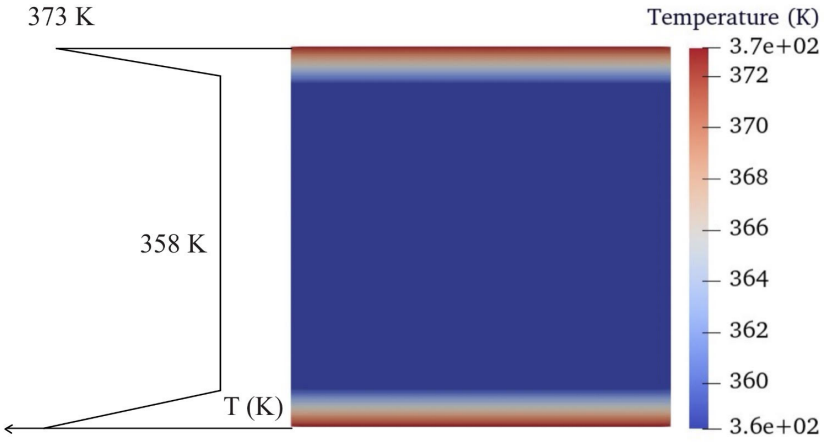



**Figure 39:** Imposed wall temperature distribution used in the study.

The study matrix included the effects of three different temperatures of the constant section at 85 °C, 90 °C, and 95 °C. Table 13 shows the case matrix.

| Case | Constant-section temperature |
|---|---|
| A | 85 °C |
| B | 90 °C |
| C | 95 °C |

**Table 13:** Case matrix for the temperature-magnitude sensitivity study.

The results of the study were once again revealing. Table 14 summarizes the characteristic convection timings for each case. Figure 40 compares the computed line-averaged concentration for the three wall-temperature cases with the experimental data.

| Metric | 85 °C | 90 °C | 95 °C |
|---|---|---|---|
| Time until convection begins [s] | 65.2 | 91.6 | 157.6 |
| Convection stabilization time [s] | 56.4 | 61.6 | 67.6 |

**Table 14:** Characteristic convection timings for the wall-temperature sensitivity cases.

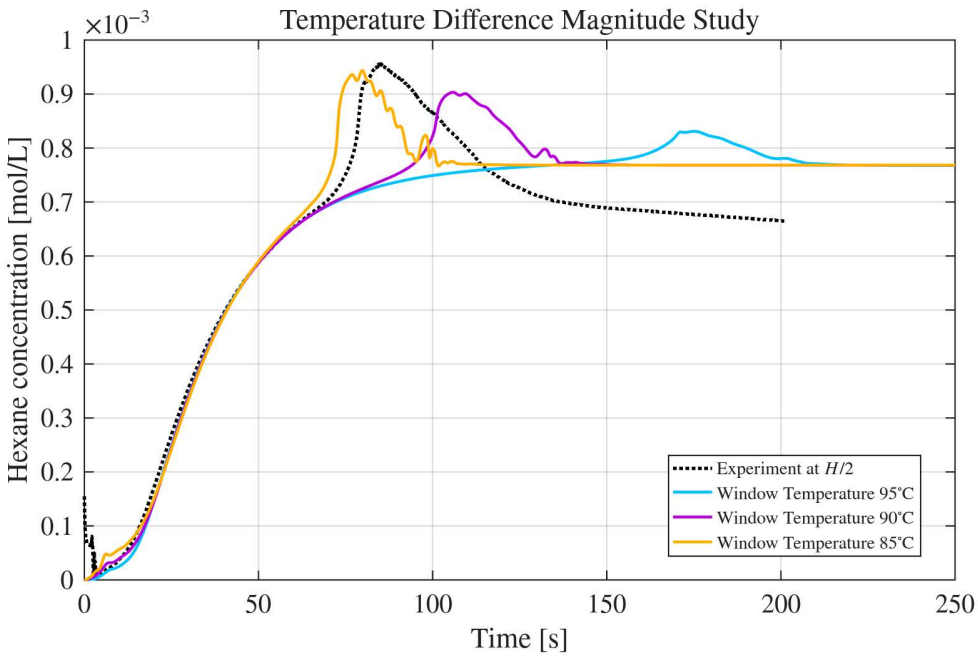



**Figure 40:** Comparison of the computed line-averaged concentration for the three wall-temperature cases and the experimental data.

Before discussing any trends, it is worth noting how similar the results for the current distribution, specifically at 85°C and 90°C, are to the experimental data. However, it cannot be inferred that there is a correlation between these distributions and the experimental one.

Comparing the cases now, a clear trend arises. The greater the temperature difference between the cool inner wall and the top and bottom heated plates, the faster convection appears and stabilizes. The trend is stronger for the convection onset timing, which varies by tens of seconds, versus the convection stabilization timing, which varies only by a few seconds. These results are consistent with physical intuition: a higher $\Delta T$ will produce a higher thermal-density difference making thermal-buoyant effects more prevalent, thereby accelerating convection onset. In addition, the convection stabilization timing shows less reduction because, as convection onset occurs earlier, the field is not yet well-mixed; however, because thermal buoyancy is more competitive, the overall time is shorter as the thermal deficit increases. The exact quantitative values can be seen in Table 14.

The convection onset trend can also be observed in Figure 41 and Figure 42. Figure 41 shows the temporal evolution of the velocity-magnitude profile along the vertical centerline of the domain, while Figure 42 presents the evolution of the total kinetic energy per unit depth in the domain as a function of time.

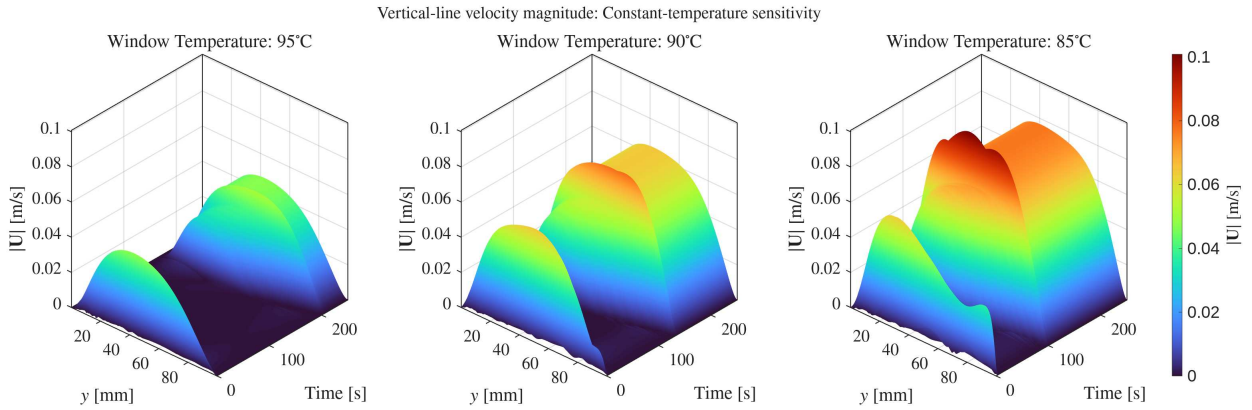



**Figure 41:** Temporal evolution of the velocity-magnitude profile along the vertical centerline for the three wall-temperature cases.

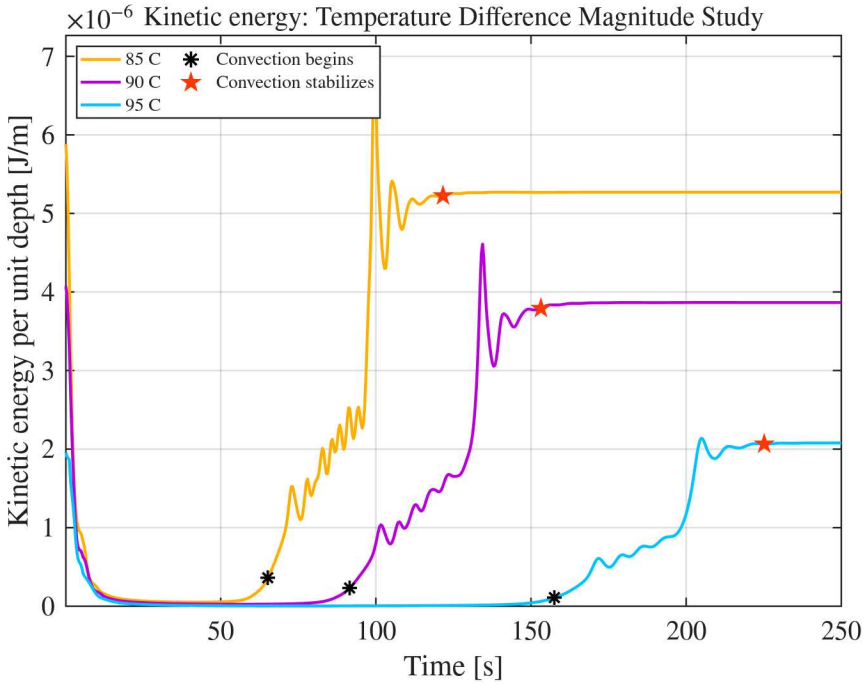



**Figure 42:** Evolution of the total kinetic energy per unit depth in the computational domain as a function of time for the three wall-temperature magnitude cases.

It can also be observed that the overall strength of the convection plume increases as the temperature difference increases, with velocity magnitude along the centerline increasing by about $0.02\,\mathrm{m\,s^{-1}}$ between cases.

The overall conclusion of the study is that the magnitude of the temperature difference accelerates the formation and stabilization of the convective mode as thermal buoyancy becomes competitive. In addition, it strengthens the conclusion that a change in the temperature boundary condition leads to drastic changes in mixing due to an altered balance between thermal and compositional buoyancy.

## 5.3 Minimum Wall-Temperature Deficit for Convection

Another study focused on the magnitude of the thermal deficit and was initiated to investigate whether a minimum thermal deficit exists below which convection would not be triggered. To do so, the maximum thermal deficit of the reference boundary condition of Section 5.1 was adjusted while keeping the top and bottom plates at 100 °C and the V-shaped distribution. The simulation time was 400 s, longer than a typical experiment. In addition, the study matrix was expanded to include another fuel, dodecane. In-depth analysis of the sensitivity of convection to fuel properties and fuel quantity will be covered in Section 6. Table 15 portrays the case matrix. Figure 43 shows variation of the convection onset with decreased thermal deficit for hexane and dodecane.

| **Fuel** | **Minimum wall temperatures** [°C] |
|---|---|
| n-Hexane | 80, 90, 95, 97 |
| n-Dodecane | 80, 90, 95, 97 |

**Table 15:** Case matrix for the thermal-deficit magnitude study.

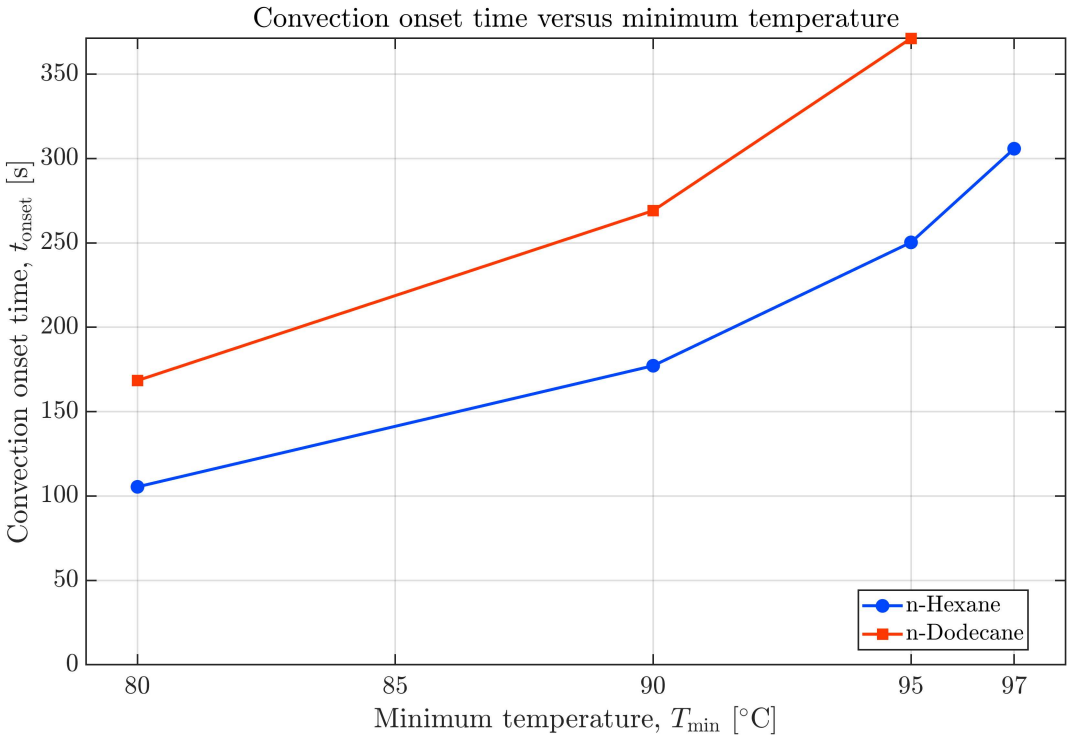
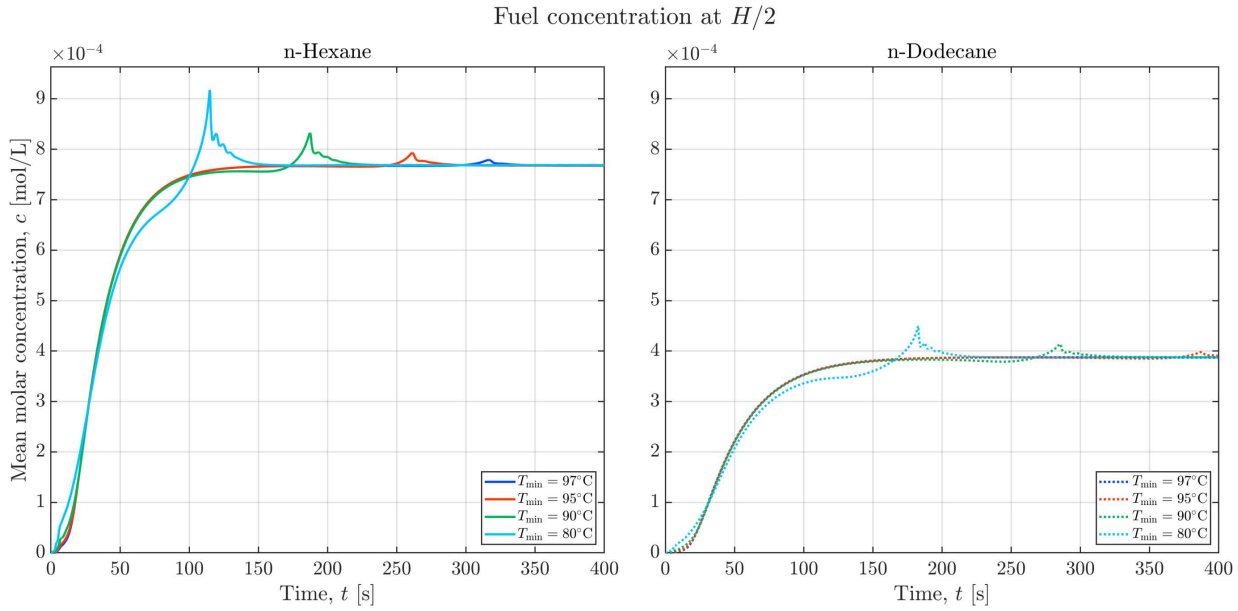



**Figure 43:** Variation of convection onset with minimum wall temperature for hexane and dodecane.

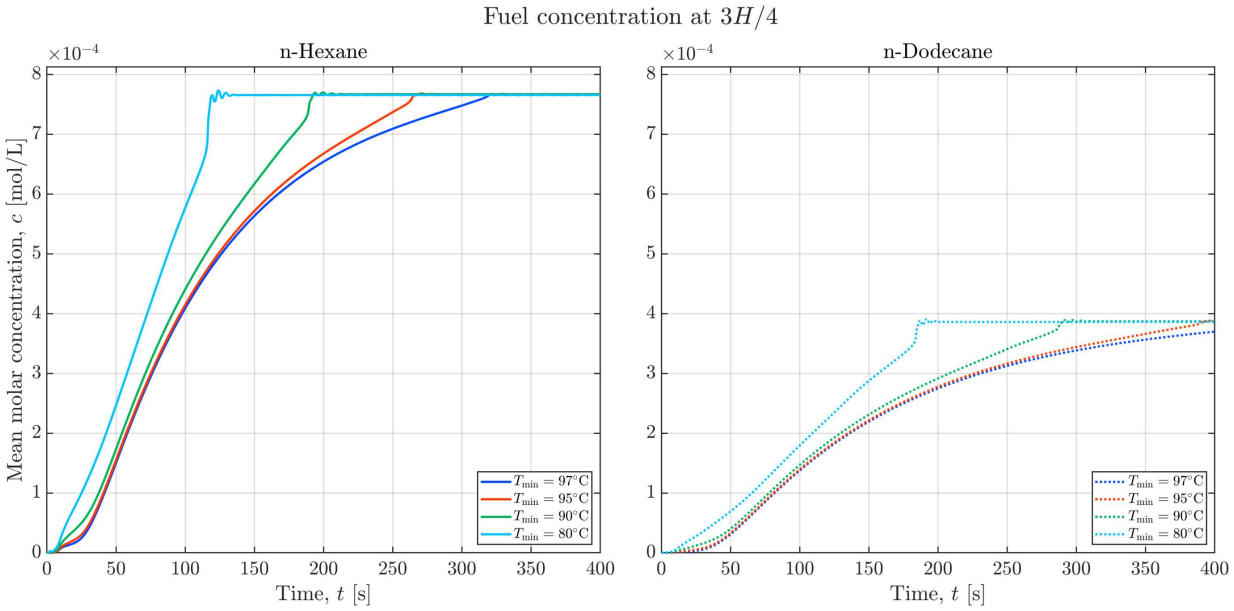
The results are quite revealing; all cases except the 97 °C dodecane case trigger onset within the 400 s of the simulation. The trend is clear: as the thermal deficit becomes smaller, thermal-buoyancy becomes weaker, takes longer to overcome compositional stratification, and therefore delays convection onset. The heavier the fuel, the lower its diffusivity, and the longer the compositional stratification lasts; more details will be given in Section 6. It is not possible to extract a minimum temperature, or a vertical asymptote in the graph. It is also not possible to perform predictive interpolation based on the study's small dataset.

Using the purely diffusive 1D model, it would take $Dt/H^2 \simeq 0.50$ for 99% mixing at $z/H = 0.75$, assuming $\delta/H = 0.0237$ or a $100\,\mu$L injection. That would mean an estimated time of $t = 0.50H^2/D \approx 444\,\text{s}$ for $D = 1.13 \times 10^{-5}\,\text{m}^2/\text{s}$ and $H = 0.10\,\text{m}$ for hexane, and approximately 661 s for dodecane using $D \approx 7.6 \times 10^{-6}\,\text{m}^2/\text{s}$, both of which are well above the standard 300 s test time for the cubic test cell. Even a small temperature deficit located at the center of the window walls (not the optimal position) of 3 °C for hexane and 5 °C for dodecane at 100 °C would trigger convection within 400 s and lead much sooner to a fully mixed environment. A better positioned cold source (near the bottom of the flask) would lead to convection onset even sooner, as explained in Section 5.1. This provides a very informative finding for the potential design of an intentional thermally-driven mixing mechanism for the cell. The computed line-averaged concentration presented in Figure 44 at $H/2$ and $3H/4$ depict the evolution toward a fully mixed environment after convection onset.




**(a)** Concentration signal at $H/2$.

**Figure 44:** Evolution of the computed line-averaged concentration for the thermal-deficit magnitude study at $H/2$ and $3H/4$.



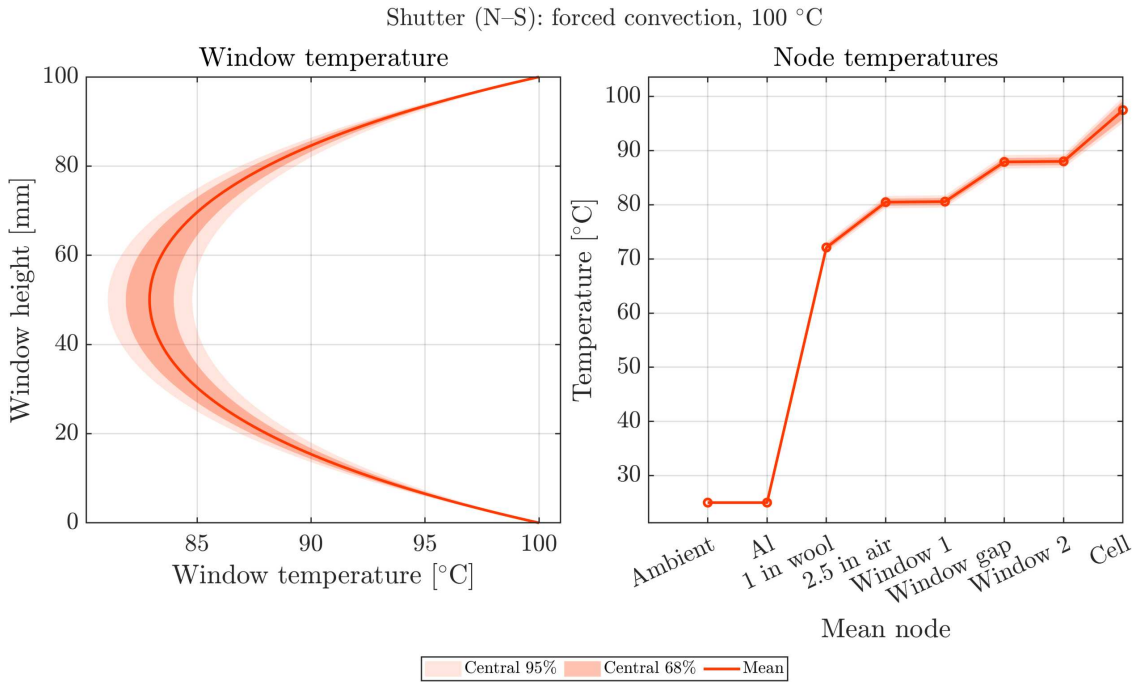

**(b)** Concentration signal at $3H/4$.

**Figure 44:** Evolution of the computed line-averaged concentration for the thermal-deficit magnitude study at $H/2$ and $3H/4$.

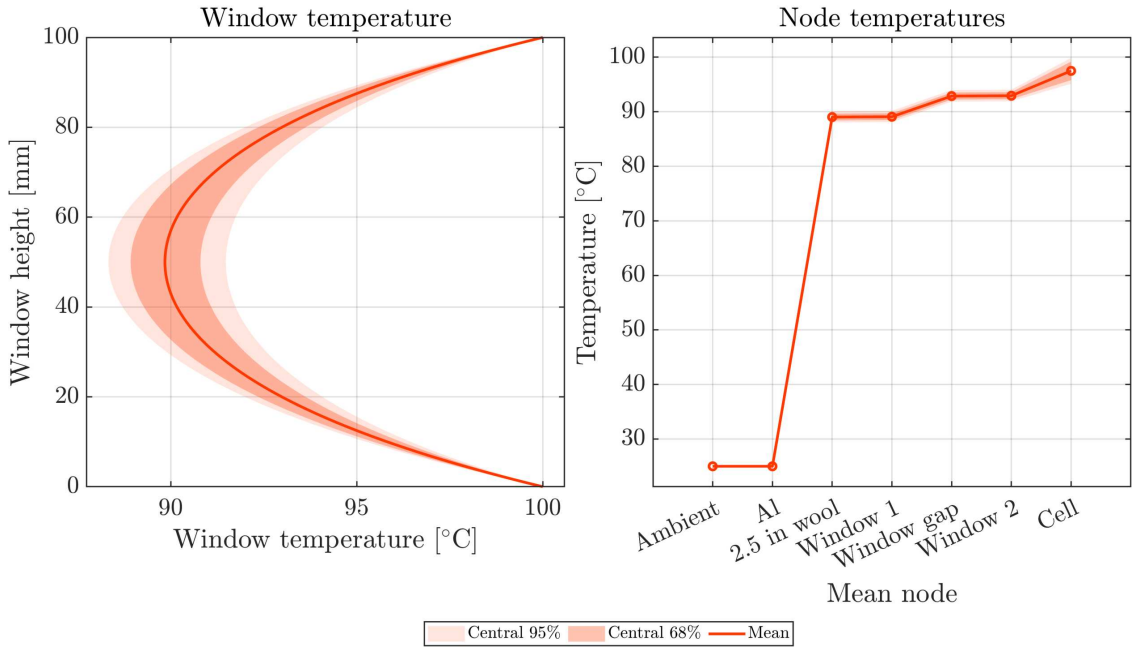
## 5.4 Heat-Transfer Model of the Window

To implement a physics-based temperature boundary condition, given its importance to the evolution of the pre-ignition field, a reduced-order quasi-2D heat transfer model was developed to estimate the temperature distribution along the walls of the test cell. The specifics of the model are included in Appendix D.

The resultant window temperature distributions had a hyperbolic shape, evolving from the top and bottom boundaries at 100 °C to an approximate 90 °C value at the middle. Figures 45a and 45b show the temperature distribution along the window and the different nodal temperatures along the heat-transfer pathway for the N-S and E-W directions, respectively.




**(a)** N-S window temperature distribution and nodal temperatures along the heat-transfer pathway.



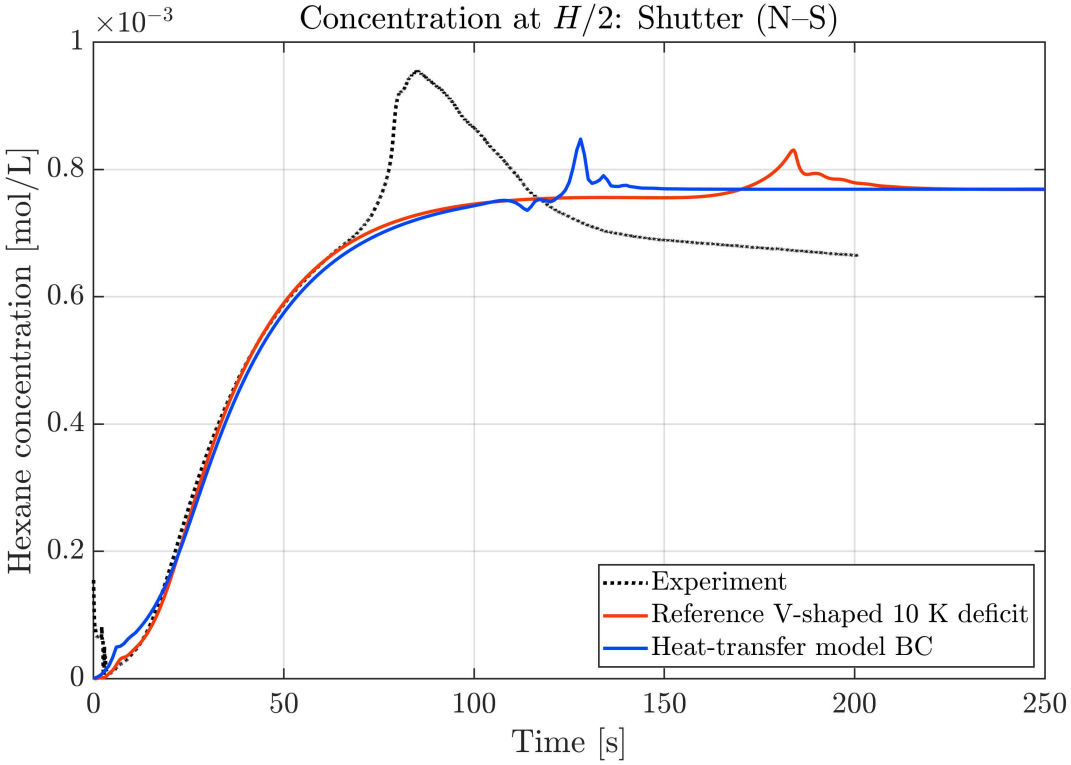

**(b)** E-W window temperature distribution and nodal temperatures along the heat-transfer pathway.

**Figure 45:** Temperature distributions and nodal temperatures computed using the Appendix D model and shown along the heat-transfer pathways for the N-S and E-W window directions.

The mean forced-convection temperature profile, shown in Figure 45b, was then used as a boundary condition into the current OpenFOAM CFD baseline to assess its agreement with the experimental signal.

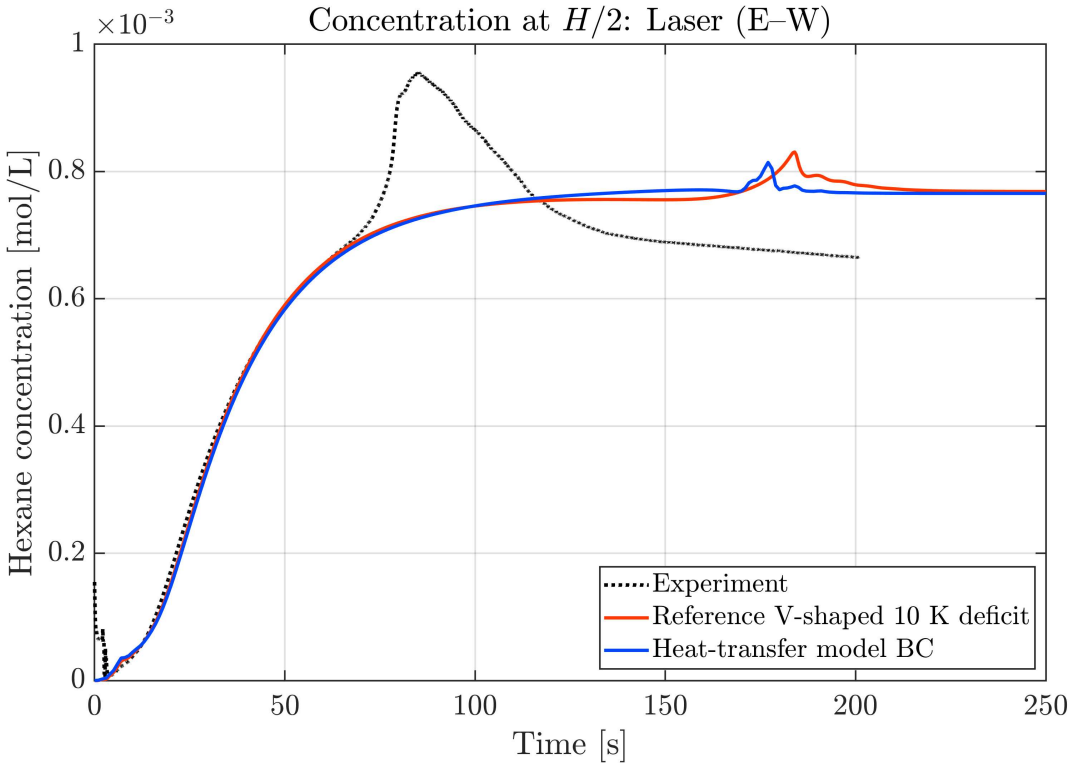
The new temperature distributions did not reproduce the experimental concentration results along

either the N-S or the E-W directions. Instead, they closely resemble the results from the Section 5.1 linear 10 K boundary-condition profile. This is reasonable, as the two distributions are similar in both distribution and magnitude. The N-S shutter temperature distribution shows earlier convection timing; this is expected given its larger wall thermal deficit compared with the E-W direction. Figure 46 shows the computed line-averaged concentration for the Section 5.1 reference case, the newly imposed boundary conditions along the N-S and E-W directions, and the experimental data.




**(a)** Concentration signal using the N-S temperature boundary condition.

**Figure 46:** Comparison of the computed line-averaged concentration obtained using the experimentally derived N-S and E-W temperature boundary conditions with the Section 5.1 reference 10 K boundary-condition case and the experimental data.




**(b)** Concentration signal using the E-W temperature boundary condition.

**Figure 46:** Comparison of the computed line-averaged concentration obtained using the experimentally derived N-S and E-W temperature boundary conditions with the Section 5.1 reference 10 K boundary-condition case and the experimental data.

These results suggest that the current heat transfer model may be an excessive oversimplification of the physical problem or that there may be an additional heat-transfer mechanism, such as a heat leak, that is not identified. It also highlights the high sensitivity of the convection formation to the imposed boundary condition profile. Note that additional 3D effects could further influence the formation of this convection, making the appropriate boundary condition choice a very complex problem.

## 5.5 Experimental Temperature Characterization Inside the Cell

The pre-injection thermal environment of the cubic test cell was further characterized in an effort to obtain information on the developed pre-injection temperature field using a T-shaped movable thermocouple probe described in Section 2.1. The characterization matrix consisted of three different batches covering different locations and/or conditions; it is presented in Table 16.

| Batch | Window condition | Probe location |
|---|---|---|
| 1 | Closed windows | Vertically along the centerline |
| 2 | Closed windows | Vertically along the window |
| 3 | Open windows | Vertically along the window |

**Table 16:** Experimental temperature characterization matrix.

For the closed-window setup, the central cell region appears to be at a fairly uniform temperature. The near-bottom data are less reliable due to the probe's limitation, and possible contact with the bottom of the cell. The current trends are therefore useful qualitatively, but not fully conclusive. This near-uniform distribution can be observed in Figure 47, where, from approximately $H/4$ to $3H/4$, $T_1$, $T_2$, and $T_3$ remain at similar values.

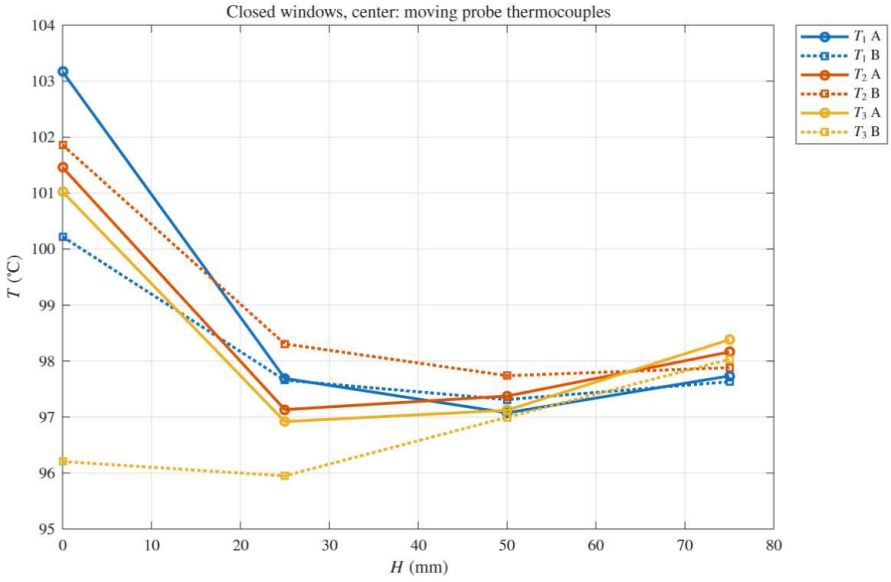



**Figure 47:** Moving-probe thermocouple measurements for the closed-window, centerline case.

Comparing the fully developed fields for the closed- and open-window cases also yields noteworthy conclusions. The open- and closed-window profiles have similar shapes, suggesting no major change in temperature distribution after opening the shutter and allowing the dry field to converge. A plot comparing the two temperature distributions along the window and in the center is shown in Figure 48:

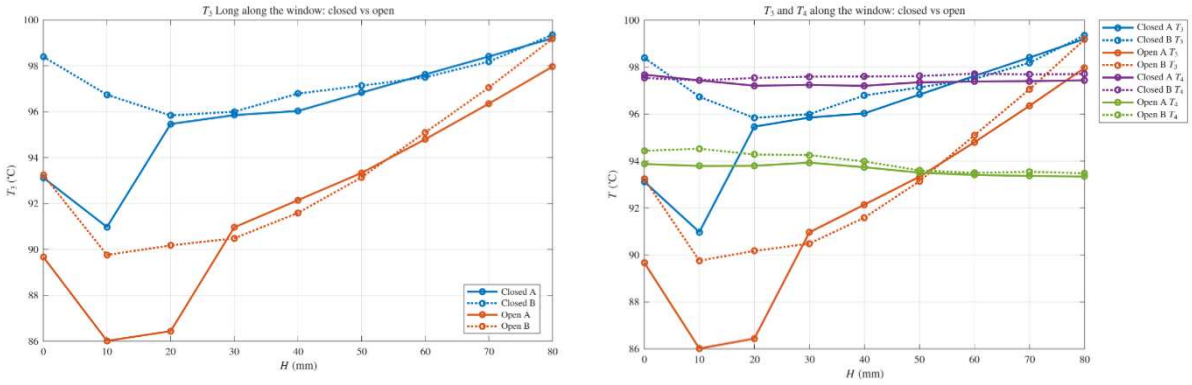
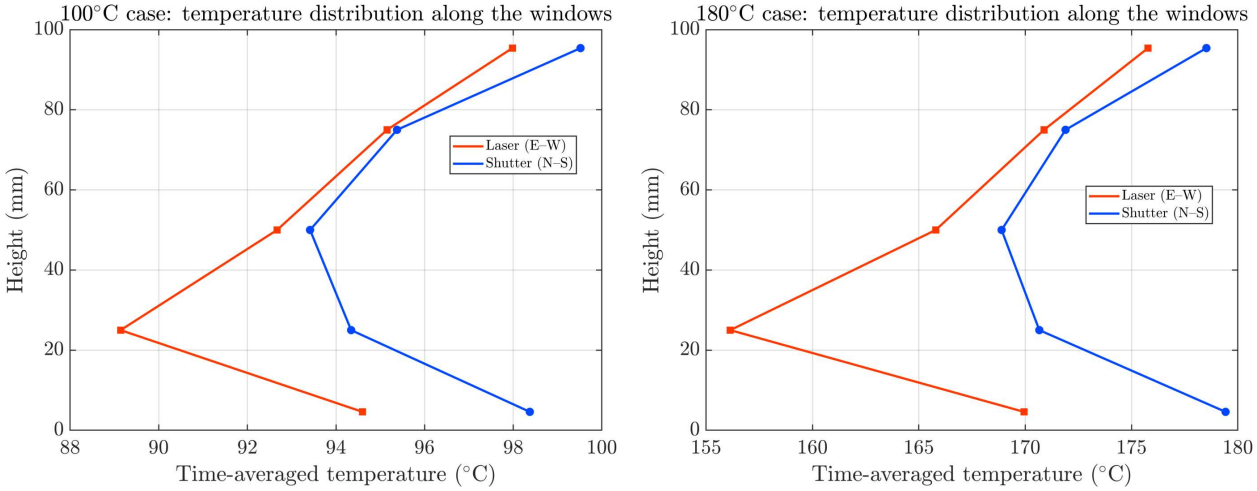



**Figure 48:** Comparison of the fully developed field temperature measurements of $T_3$ along the window and $T_4$ for the closed- and open-window cases.

## 5.6 Experimental Wall-Temperature Characterization

To better inform the physical choice underlying the temperature boundary condition, experimental temperature characterization along the walls was conducted using Type K self-adhesive thermocouples to gather data on the spatial distribution. Repeatability of the measurements was demonstrated; all the details of the experimental methodology are provided in Section 2.1. Figure 49 shows the steady-state, linearly interpolated temperature distributions at 100 °C and 180 °C.




**(a)** Steady-state, linearly interpolated wall temperature distribution at 100 °C.

**(b)** Steady-state, linearly interpolated wall temperature distribution at 180 °C.

**Figure 49:** Steady-state, linearly interpolated wall temperature distributions measured using Type K self-adhesive thermocouples at 100 °C and 180 °C.

We can infer from Figure 49 that the temperature distribution along the N-S direction, or the window shutter direction, closely resembles that obtained in Section 5.4 using the 2D heat transfer model. However, the E-W direction reports a substantial drop in temperature near the bottom of the flask. This trend holds for both temperature cases. This drop is hypothesized to occur as there is no direct insulation (an additional window) between the cell's window and the laser opening, causing cold air to leak and substantially cool the cell. Figure 50 shows a schematic of this phenomenon in the cell. This is quite a revealing finding, as we now know that the mixing is very sensitive to wall-temperature boundary conditions.

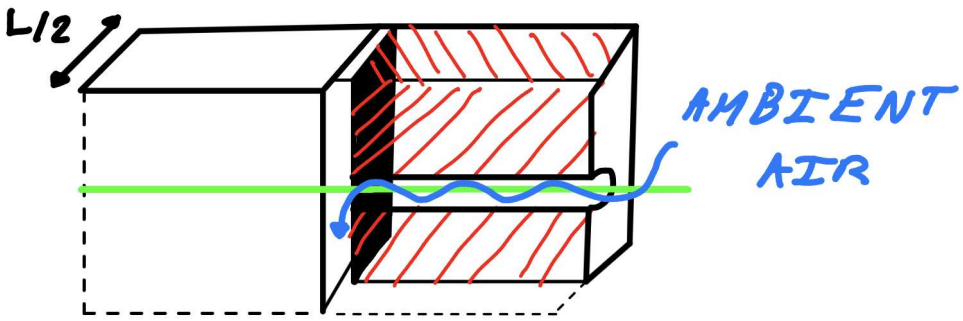



**Figure 50:** Schematic representation of the hypothesized cold-air leakage near the laser opening and the resulting localized cooling of the cell wall near the bottom of the window.

The experimentally obtained temperature distributions were implemented in the OpenFOAM framework for both the shutter N-S and laser E-W directions. Figure 51 shows experimental and computed line-averaged concentration.

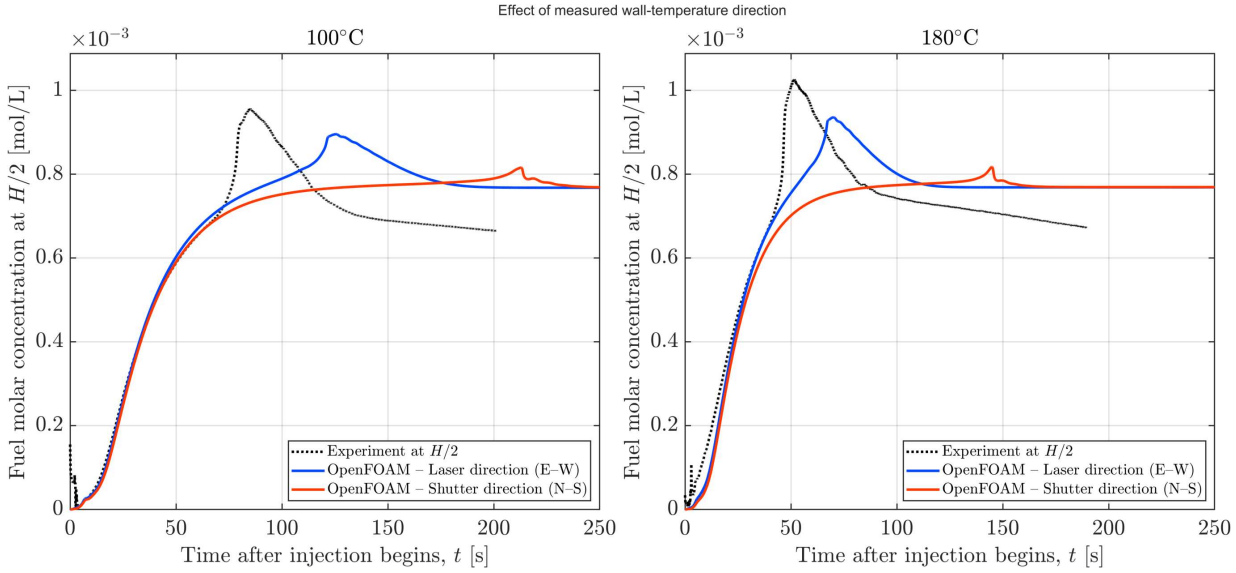
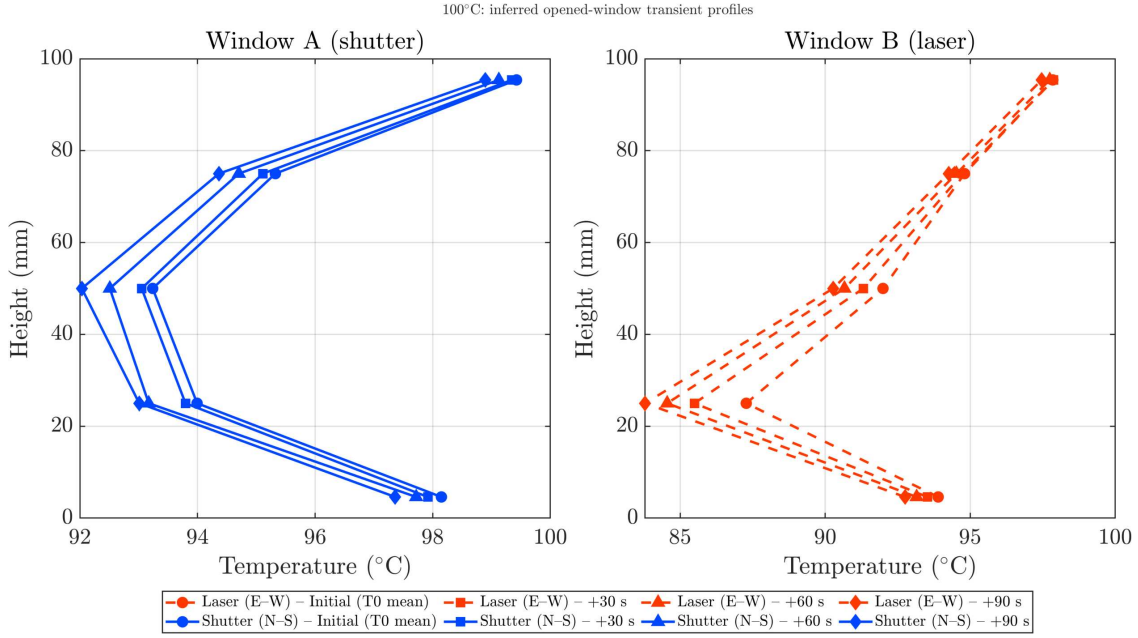



**Figure 51:** Comparison of the experimental and computed line-averaged concentration using the experimentally measured wall-temperature distributions.

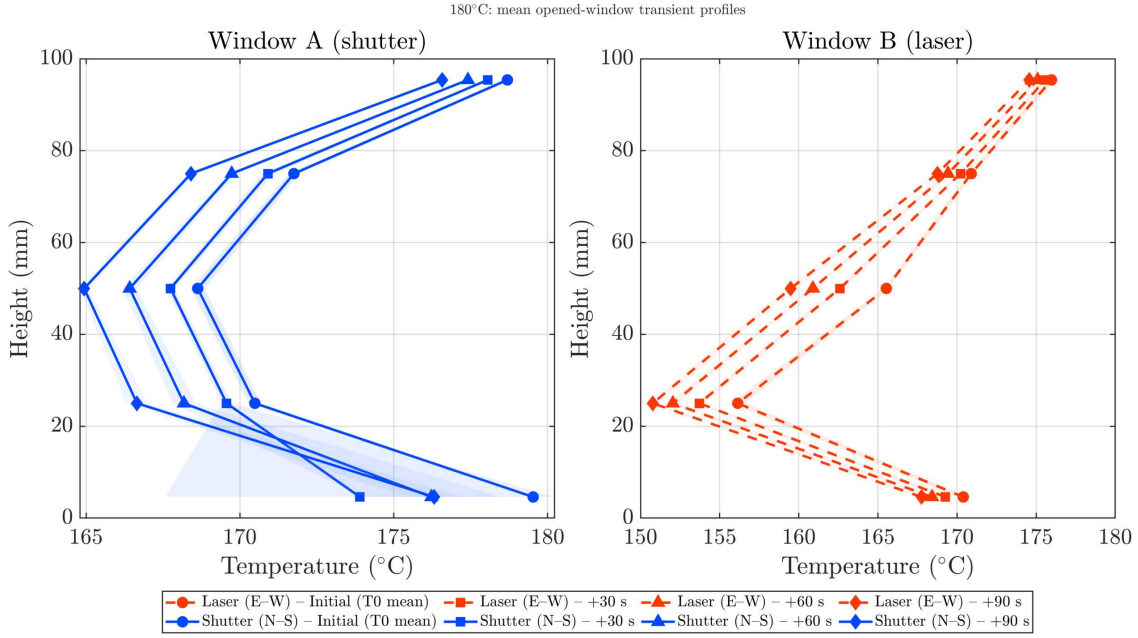
The agreement between the simulation using the laser-direction boundary condition and the experiment has significantly improved, though some timing differences remain. This is to be expected, as the position of the coldest point is near the bottom of the flask and will accelerate the convection onset timing as explained in Section 5.1. The differences in the agreement may be explained by the previously observed strong sensitivity of convection to the temperature distribution, together with the 2D simplification, and the discrete nature of the thermocouple measurements. Placing the thermocouple probe a few millimeters upward or downward may reveal an additional 1 °C temperature drop, which could accelerate the onset of convection by a few seconds in the simulation and provide closer agreement with the experimental results.

Finally, the transient thermocouple history was recorded after opening the shutters to characterize

the thermal response. The intention was to analyze whether the additional heat loss from reduced insulation after removing the shutters would lead to a faster onset of convection, given the solution's sensitivity to the temperature boundary condition. Figure 52 shows the time evolution of the wall thermal conditions for both 100 °C and 180 °C.




**(a)** Wall temperature evolution at 100 °C.




**(b)** Wall temperature evolution at 180 °C.

**Figure 52:** Evolution of the wall temperature profiles following the opening of the shutters at case temperatures of 100 °C and 180 °C.

It can be observed from Figure 52 that the drop in temperature is quite small, with most thermocouples decreasing by an average of approximately 1 °C in the 100 °C case and 2 °C in the 180 °C case.

Interestingly, the thermocouple with the largest temperature drop is the $T_2$ thermocouple, which was considered the region driving convection, despite not being in the direction of the shutters. Figure 53 shows the comparison of the measured line-averaged concentration.

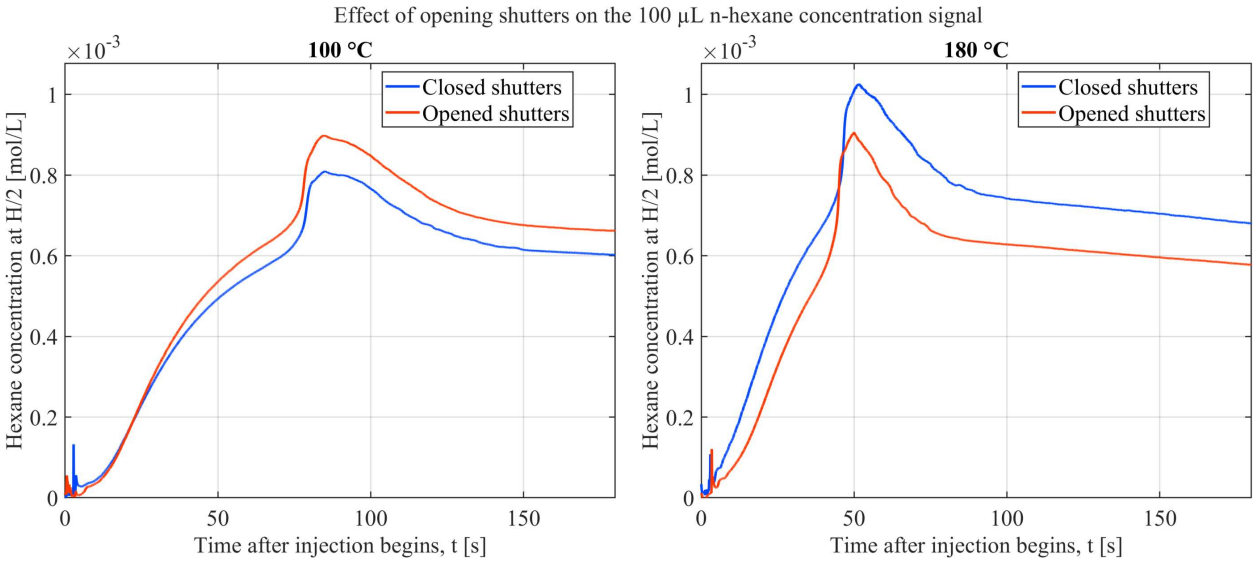



**Figure 53:** Comparison of the measured line-averaged concentration for the closed- and open-shutter cases at 100 °C and 180 °C.

It can be observed that in both the open- and closed-shutter cases, the convection onset occurs at similar times. The difference in the measured concentrations may have arisen from small differences in the amount of fuel injected or other factors, such as the reheating time between experiments. There is currently insufficient data to infer that the transient temperature drop in the windows significantly accelerates the onset of convection.

From the study, it is concluded that a region of increased heat loss, most likely caused by the lack of insulation along the laser direction, is likely to contribute significantly to the experimentally observed convection onset. Temperature drops after opening the shutters are on the order of 1–3 °C on average, but their effect on accelerating convection onset has not been conclusively established.

## 5.7 Conclusions

From the previously presented studies, it is concluded that the formation and stabilization of convection within the cell are highly sensitive to both the overall magnitude and the distribution of the temperature boundary condition. Larger temperature deficits lead to earlier convection onset and shorter stabilization times due to the increased strength of thermal buoyancy relative to compositional stratification. Local temperature drops are most effective in triggering convection near the bottom of the cell because the composition field at lower heights evolves earlier as the initial vapor layer diffuses upward. Experimentally, an unexpected heat-leak region is observed, causing a localized thermal-deficit spike near the bottom of the walls in the laser direction, which possibly contributes to convection. The transient temperature drop is on the order of 1–3 °C; its effect on accelerating convection onset is not yet conclusive. All these observations are consistent with the competition mechanism explained in Section 3. An accurate representation of the wall thermal conditions is therefore key to bringing the numerical results closer to experimental reality. It is also

important to consider all possible heat-loss pathways in the design of the cell, given the considerable effect that temperature differences of only a few degrees can have on the mixing mechanism.

# 6 Sensitivity to Fuel Properties and Fuel Quantity

The final batch of parametric studies focuses on the effect of fuel properties and fuel quantity on convection in the cell. These changes will alter the balance of the competition mechanism and affect the mixing mechanism. Experimental repeatability was demonstrated for the setup in Section 2.1. The reference case for the studies is described in Table 17. The reference temperature boundary condition is shown in Figure 54; it was chosen as it yielded the most similar concentration signal to the experimental one.

| **Parameter** | **Reference value** |
|---|---|
| Fuel | Hexane |
| Case temperature | 100 °C |
| Temperature boundary conditions | 15 °C constant deficit |
| Injected equivalent mass | 0.0655 g |
| Vaporization duration | 5 s |
| Vaporization shape | 50 mm × 5 mm at the bottom center |

**Table 17:** Reference case to explain pre-ignition dynamics.

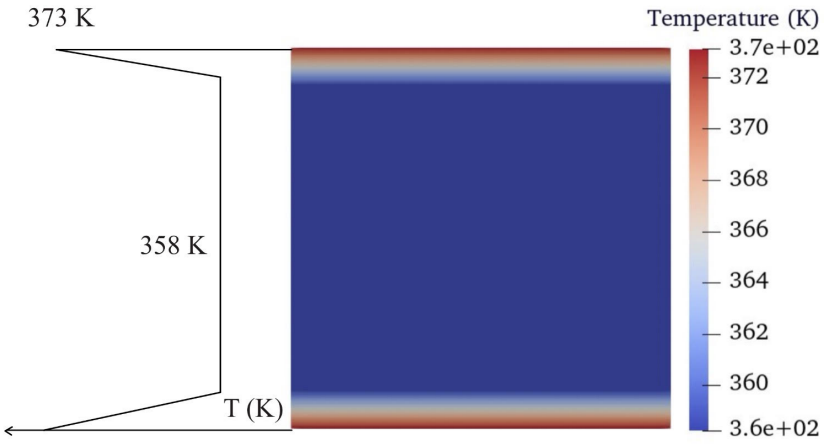



**Figure 54:** Imposed wall temperature distribution used in the study.

## 6.1 Fuel Molecular-Weight Study

The first study focused on the effect of fuel molecular weight. Table 18 summarizes the fuel selection used in the numerical parametric study. The total injected mass across the cases remained constant. Table 19 shows the variation in convection metrics. Figure 55 shows the effect of molecular weight on the concentration signal.

| Fuel | Molecular weight [g/mol] |
|---|---|
| Reference n-Hexane | 86.18 |
| n-Nonane | 128.26 |
| n-Dodecane | 170.34 |
| n-Pentadecane | 212.42 |

**Table 18:** Fuel matrix for the molecular-weight parametric study.

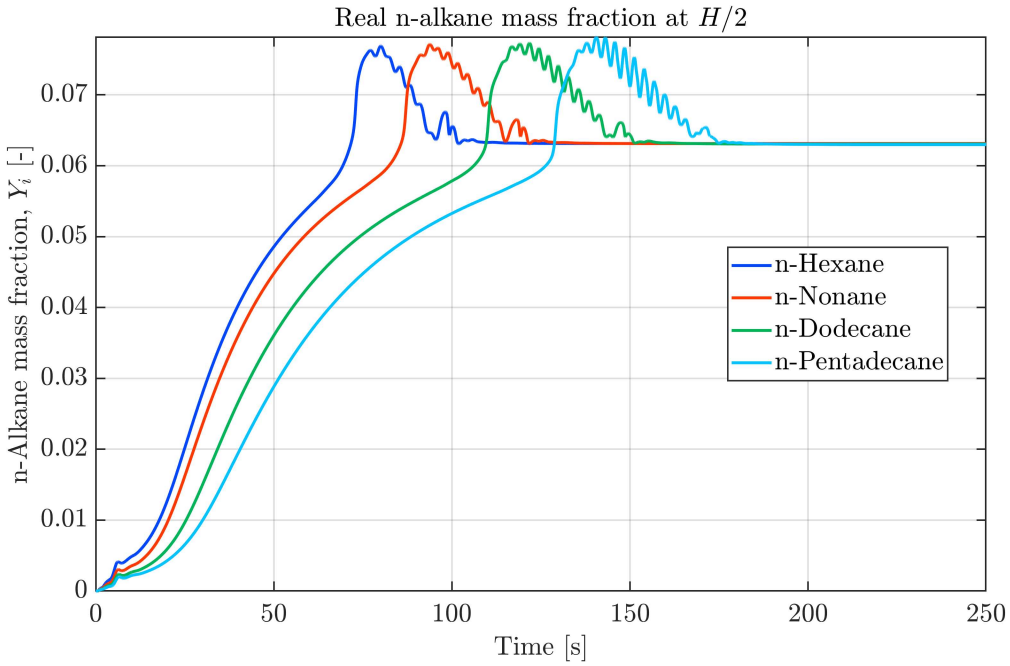



**Figure 55:** Effect of fuel molecular weight on the computed line-averaged concentration history at H/2.

| Fuel | Convection onset [s] | Stabilization [s] |
|---|---|---|
| Reference n-Hexane | 65.35 | 55.95 |
| n-Nonane | 78.90 | 56.95 |
| n-Dodecane | 101.40 | 64.60 |
| n-Pentadecane | 119.75 | 74.45 |

**Table 19:** Convection metrics for the fuel molecular-weight study.

It is observed that higher-molecular-weight fuels exhibit later onset and stabilization of convection. These results are consistent with the competition mechanism explanation from Section 3.5: within the n-alkanes considered, increasing molecular weight is associated with a decrease in diffusivity, and the compositional stratification take longer to smear out until thermal buoyancy becomes competitive. The decrease in diffusivity is consistent with the Chapman–Enskog expression for binary species diffusion[12]; an increase in cross section, and therefore effective collision diameter, will decrease diffusivity $D_{AB} \propto 1/\sigma_{AB}^2$.

$$D_{AB} = \frac{3}{16} \frac{\sqrt{\frac{2\pi k_B^3 T^3}{\mu_{AB}}}}{p\,\pi\sigma_{AB}^2 \Omega_D}. \tag{30}$$

Where $\sigma_{AB}$ is the effective collision diameter, $\mu_{AB}$ is the reduced molecular mass, and $\Omega_D$ is the collision integral.

In terms of stabilization, it is hypothesized that lower diffusivity may lead to a slower smearing of the interface between the mixed and unmixed regions, thereby yielding a longer stabilization time. The mechanism is not completely understood. It is also observed that there are differences in the mixing mechanisms between the cases. The concentration signal indicates that the oscillatory behavior in the convection stabilization process is enhanced with increasing molecular weight. This may arise from a larger restoring buoyancy force arising from a sharper interface for lower-diffusivity, higher-molecular-weight species, which causes the restoring density difference to be higher across the non-mixed–well-mixed interface. This trend is also consistent with the explanation of internal waves in a box provided in Section 3.6.

The study was also carried out experimentally in the laboratory, with fuel selection varying based on availability. Total injected mass, 0.06550 g, remained constant across fuels. This was equivalent to 105.5 $\mu$L of pentane, 100 $\mu$L of hexane, and 96.6 $\mu$L of heptane. Note that there was an uncertainty of $\pm 2\,\mu$L due to a manual injection process used only for this study. Table 20 shows the experimental fuel variation matrix. Figure 56 shows the effects of increased molecular weight on the time evolution of the line-averaged concentration in terms of fuel mass fraction. The procedure for reducing the data for these cases is described in Section 2.1.

| **Fuel** | **Molecular weight [g/mol]** |
|---|---|
| n-Pentane | 72.15 |
| n-Hexane | 86.18 |
| n-Heptane | 100.21 |

**Table 20:** Fuel matrix for the experimental molecular-weight study.

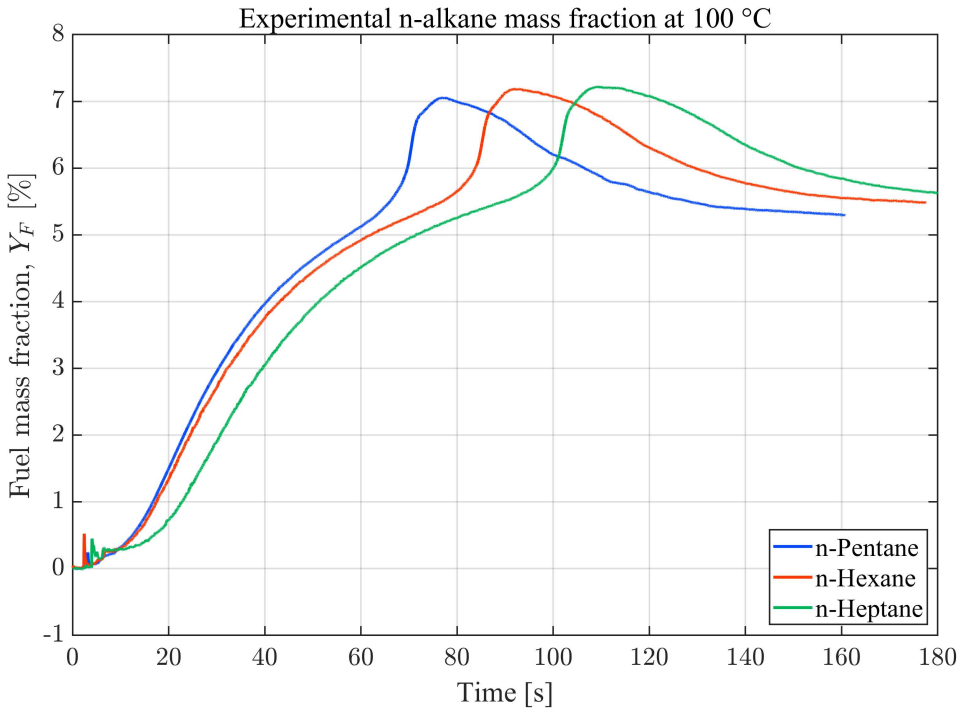



**Figure 56:** Experimental measurements of line-averaged concentrations for the fuel molecular-weight study.

It can be observed that the numerical trend holds experimentally: as molecular weight increases, diffusivity decreases, leading to longer convection onset and stabilization times. As mentioned in Section 3.5, however, the concentration signal oscillations are not prevalent in the experimental data.

Note that the original experiments also included Octane and Dodecane. They have been excluded from the present study as their boiling temperatures exceeded 100°C, resulting in significant condensation at the walls and preventing comparison with differences in the diffusive part of the mixing mechanism. These cases were discussed in Section 4.4.

## 6.2 Injected-Volume Dependence

The following parametric study examined the effect of injection volume on mixing. Table 21 shows the case matrix. Table 22 shows the resulting convection metrics. Figure 57 portrays the evolution of the concentration signal.

| **Case** | **Injected volume** [$\mu$L] |
|---|---|
| A | 50 |
| B | 75 |
| Reference | 100 |
| C | 200 |

**Table 21:** Case matrix for the injected-volume parametric study using hexane.

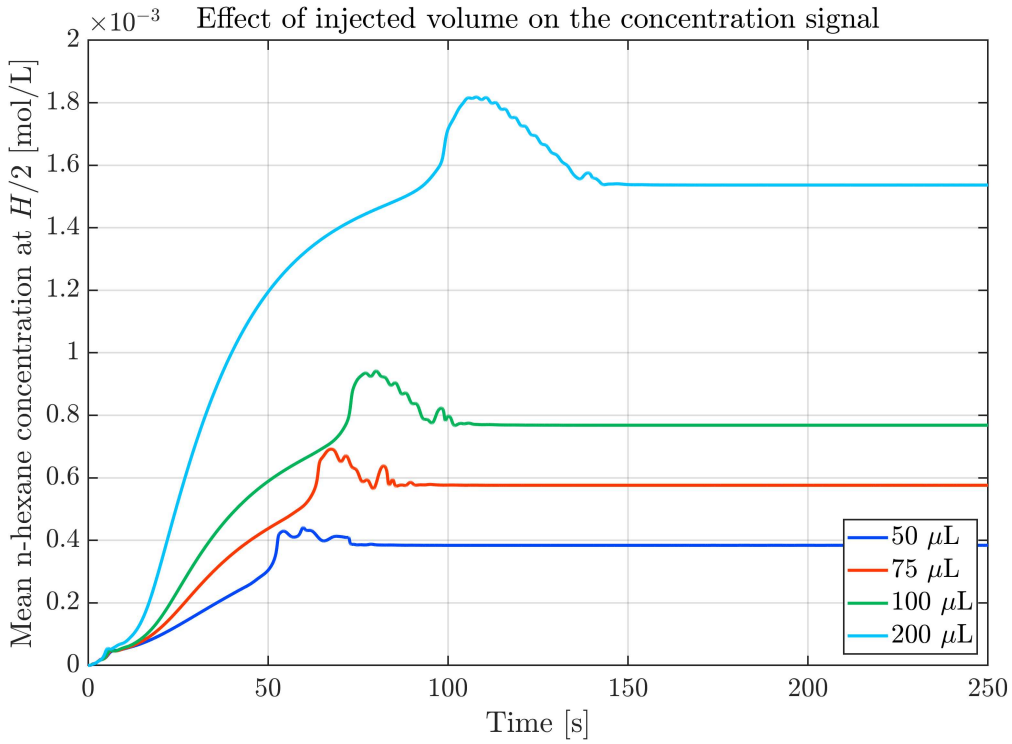



**Figure 57:** Time evolution of the computed line-averaged concentration for the injected-volume dependence study, raw data.

| Injected volume [$\mu$L] | Convection onset [s] | Stabilization [s] |
|---|---|---|
| 50 | 47.25 | 45.05 |
| 75 | 57.35 | 48.85 |
| Reference 100 | 65.35 | 55.95 |
| 200 | 87.65 | 70.65 |

**Table 22:** Variation in the convection metrics for the injected-volume dependence study.

As expected, a larger fuel amount delays the onset of convection. This is consistent with the competition mechanism: as more fuel is injected, the mixture becomes more fuel-rich, and compositional stabilization strengthens; thus, a longer time is required for convection to be triggered. The trend also holds for convection stabilization: after a local density inversion and convection onset, the concentration field in the higher-injected-volume cases will have a higher magnitude in the composition gradients that thermal buoyancy must overcome, leading to longer stabilization times.

Applying non-dimensional scaling to the results by using $t^* = Dt/H^2$ and $c^* = c/c_0$, we can observe how the diffusive processes collapse for volumes $> 75\,\mu$L, but that the higher volume cases show later convection onset and longer stabilization times. Figure 58 shows the non-dimensionalization of the injected-volume dependence study. Although the scaled concentration gradients $c/c_0$ may be the same, their physical magnitudes, which are driving the convection, are larger in the higher-injected-volume cases, yielding a more compositionally stable field and requiring stronger thermal buoyancy and thus more time for the convection to onset and stabilize even when collapsed non-dimensionally.

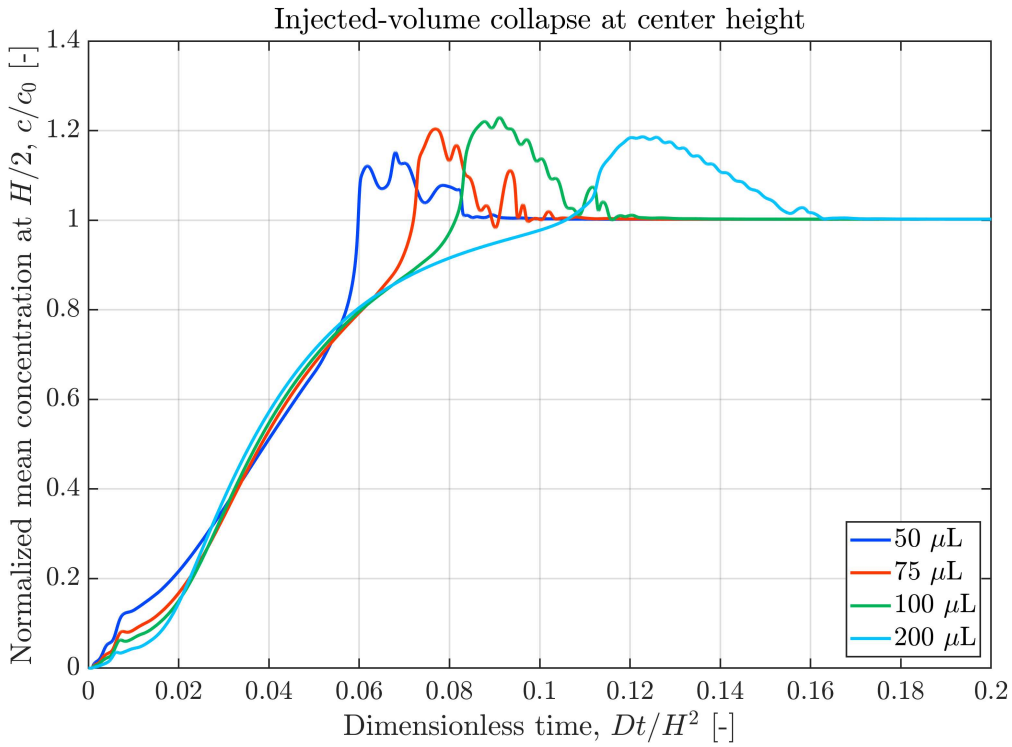



**Figure 58:** Time evolution of the computed line-averaged concentration for the injected-volume dependence study, non-dimensional concentration vs. nondimensional time.

It is also noteworthy that the 50 $\mu$L diffusive process does not follow the same diffusive curve as the other cases. One possible explanation is that the buoyancy-driven stratification produced by a lower injection volume will be smaller, making differences in the injection process prevail over time. This conclusion follows the rationale explained in Section 4.4. Vaporization process-driven differences are erased by strong buoyancy forcing; if this force is smaller, for example, by a smaller injection volume or lighter fuel, these differences may not be fully erased and affect the convection formation. Note that this is not the case for the applications of interest, where the relevant fuels have relatively high molecular weights, and injection volumes are above 100 $\mu$L.

This study was also previously conducted in the laboratory by Fouchier[6]. The experimental results agree with the previously stated trends. The 50 $\mu$L case is much closer to non-dimensional collapse in the experimental study, which may reflect a limitation in the vaporization modeling for this volume (imprecise cloud shape, for example). Figure 59 shows the difference of injected volume on the non-dimensionalized concentration signal. Note that the difference in the exact concentration history arises from the imprecise modeling of the temperature boundary conditions.

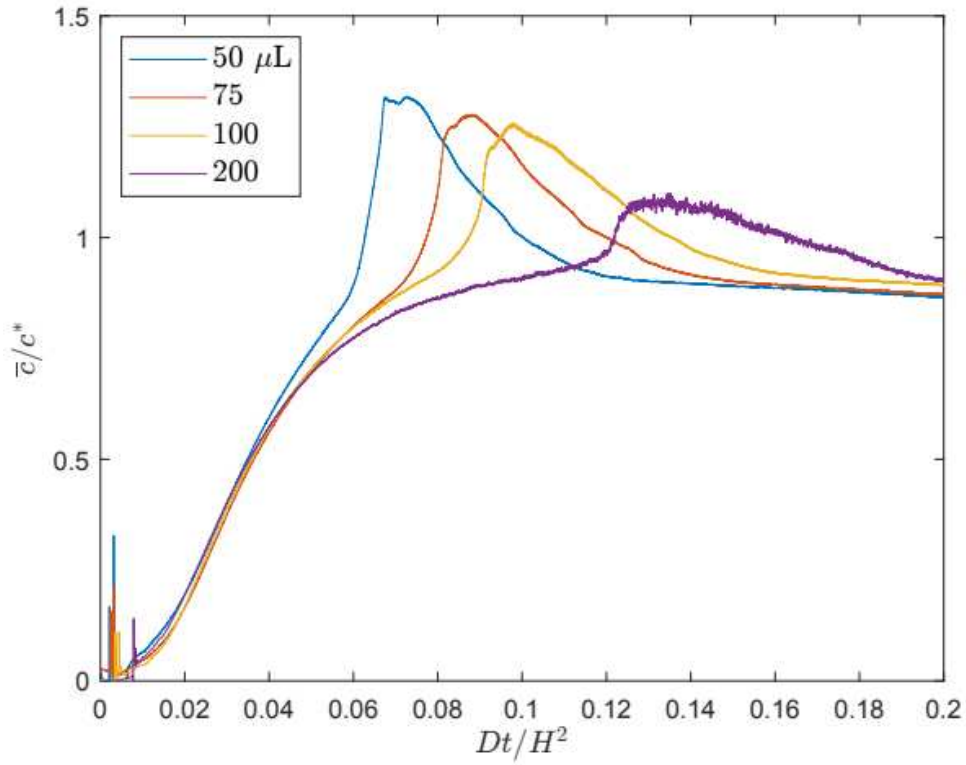



**Figure 59:** Effect of injected volume on the experimental line-averaged concentration, nondimensional variables. Adapted from Fig. 8 of Fouchier et al. [6]

### 6.3 Temperature Dependence

The last parametric study covers the effects of case temperature on convection formation. Note that this study couples temperature and fuel property changes: on the one hand, thermal buoyancy increases with case temperature as the thermal deficit scales up; on the other hand, fuel diffusivity is temperature-dependent and increases, smearing the compositional stratification sooner. The study was conducted only experimentally. Table 23 shows the experimental case matrix for a 100 $\mu$L injection. Figure 60 compares the effect of case temperature on the concentration signal.

| **Case** | **Case temperature** [°C] |
|---|---|
| A | 100 |
| B | 180 |

**Table 23:** Experimental case matrix for the case-temperature study.

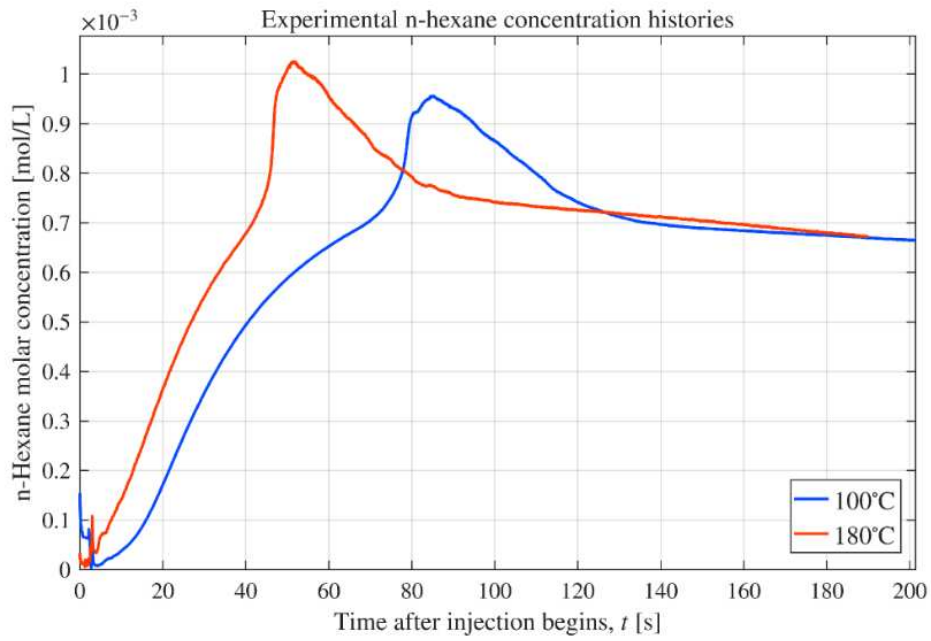



**Figure 60:** Effect of case temperature on the experimental line-averaged concentration for 100 $\mu$L hexane injections.

As expected, at higher cell temperatures, both the mixture diffusivity and the thermal-buoyancy effects are enhanced, leading to faster and stronger convection.

### 6.4 Conclusions

It is concluded that fuel properties will also have a significant effect on the mixing mechanisms in the cell. For higher molecular-weight fuels, convection onset and stabilization will be slower due to the associated lower fuel diffusivity. For higher injection volumes, the onset and stabilization of convection will be slower due to increased compositional stratification, as the mixture becomes more fuel-rich after injection. Finally, an increase in case temperature will accelerate the onset and stabilization of convection by increasing fuel diffusivity and thermal-buoyancy strength. All of these conclusions are consistent with the competition mechanism covered in Section 3.5.

## 7 Conclusions and Future Work

The present work provided insight into the buoyancy-driven mixing processes inside the experimental cubic test cell. These findings may also enable the design of the next generation of test cells or standardized test apparatus. The results of our study are summarized below:

- For the rapid vaporization cases above $T_{\text{boiling}}$ and standard injections $> 100\,\mu$L of representative fuels with molecular weights above approximately 80 g/mol with the current reduced-complexity model, variations in the spatial and temporal aspects of injection had no significant impact on the subsequent convection.

- Convection is highly sensitive to the wall temperature distribution, both to the overall deficit magnitude and to the profile shape. Temperature deficits near the bottom of the cell triggered convection most effectively. As case temperature rises, convection onset occurs sooner due to a combined effect of stronger thermal buoyancy and increased fuel diffusivity, which erases compositional stratification sooner.
- The properties of the fuel tested also determine the mixing timescale. Higher molecular-weight fuels will delay the onset of convection due to their lower diffusivities, which are associated with the greater persistence of compositional stability induced after vaporization. Higher injection volumes will also delay the onset of convection due to greater compositional stratification from a more fuel-rich region near the bottom of the flask.

As noted in the introduction, different mixing behaviors may lead to distinct pre-ignition environments and affect the variability of results. These results imply that there must be more careful monitoring and characterization of wall temperatures; fuel properties must be considered not only from a chemical ignition standpoint but also in mixing phenomena; and efforts should focus on developing mixing techniques to overcome mixing differences and achieve a similar fully mixed field among cases.

The clear future steps are to extend the simulation framework to 3D. The current 2D simulations cannot be expected to supply quantitatively representative 3D flowfields without further 3D validation, as there may be 3D flow asymmetries that are not captured by the current setup. In addition, the next clear step is to connect differences in the mixing processes and the pre-ignition field directly to autoignition variability.

# References


[1] Conor D Martin and Joseph E Shepherd. Low temperature autoignition of Jet A and surrogate jet fuel. *Journal of Loss Prevention in the Process Industries*, 71:104454, 2021.

[2] Colson Johnson and Chad Mashuga. Reconsidering autoignition in the context of modern process safety: Literature review and experimental analysis. *Journal of Loss Prevention in the Process Industries*, 81:104963, 12 2022. doi: 10.1016/j.jlp.2022.104963.

[3] ASTM-E659. *Standard test method for autoignition temperature of liquid chemicals*. American Society for Testing and Materials, 2014.

[4] Branson Davis, Charline Fouchier, and Joseph E Shepherd. Fluid motion and heat transfer in an ASTM-E659 apparatus. *Journal of Loss Prevention in the Process Industries*, 94:105558, 2025.

[5] Branson Davis, Joseph Shepherd, and Rémy Mével. Numerical modeling of gaseous n-hexane autoignition in an astm-e659 apparatus. *Fuel*, 405:136691, 2026.

[6] Charline Fouchier, Hannah Ramsperger, and Joseph E. Shepherd. Autoignition testing: Injection, mixing, and ignition. 16th International Symposium on Hazards, Prevention and Mitigation of Industrial Explosions, Kaohsiung, Taiwan, April 20–24, 2026, 2026.

[7] R. Mével, P.A. Boettcher, and J.E. Shepherd. Absorption cross section at 3.39$\mu$m of alkanes, aromatics and substituted hydrocarbons. *Chemical Physics Letters*, 531:22–27, 2012. doi: 10.1016/j.cplett.2012.01.069.

[8] Charline Fouchier and Joseph Shepherd. ASTM-E659 standardized test analysis and results for synthetic paraffinic kerosene. *Journal of Loss Prevention in the Process Industries*, 94:105568, 2025.

[9] CFD Direct. OpenFOAM v13 user guide: Solver modules. `https://doc.cfd.direct/openfoam/user-guide-v13/solvers-modules`, 2025. Accessed: 2026-07-07.

[10] OpenCFD Ltd. $p_{rgh}$ pressure formulation. `https://doc.openfoam.com/2312/tools/processing/solvers/algorithm-p-rgh/`, 2023. OpenFOAM v2312 documentation. Accessed: 2026-09-25.

[11] OpenCFD Ltd. JANAF thermodynamics model. `https://doc.openfoam.com/2306/tools/processing/models/thermophysical/thermodynamics/rtm/janaf/`, 2023. OpenFOAM v2306 documentation. Accessed: 2026-07-07.

[12] Robert Kee, Michael Coltrin, Peter Glarborg, and Huayang Zhu. *Chemically Reacting Flow: Theory, Modeling and Simulation*. Wiley, 2nd edition, 2017.

[13] D.J. Tritton. *Physical Fluid Dynamics*. The Modern University in Physics Series. Springer Netherlands, 1977.

[14] Branson Davis. Buoyancy driven flow equation derivations. Unpublished manuscript, August 2022.

[15] J.S. Turner. *Buoyancy Effects in Fluids*. Cambridge Monographs on Mechanics. Cambridge University Press, 1979.

[16] Frank P. Incropera, David P. DeWitt, Theodore L. Bergman, and Adrienne S. Lavine. *Fundamentals of Heat and Mass Transfer*. Wiley, 7th edition, 2007.

[17] Stuart W. Churchill and Humbert H.S. Chu. Correlating equations for laminar and turbulent free convection from a vertical plate. *International Journal of Heat and Mass Transfer*, 18(11): 1323–1329, 1975.

[18] L.D. Landau and E.M. Lifshitz. *Fluid Mechanics*, volume 6 of *Course of Theoretical Physics*. Pergamon, 2013.

## Acknowledgments

I would like to thank Prof. Shepherd and Dr. Fouchier for the opportunity to conduct this research at the Explosion Dynamics Laboratory. Their guidance and help were key to the success of this work. Thank you, Prof. Shepherd, for the time spent in meetings and the unmeasurable knowledge and resources you shared with me. Thank you, Dr. Fouchier, for introducing me to experimental methods, challenging me with important questions, and always being available; you have been an incredible mentor. Your guidance has also strengthened my interest in pursuing graduate studies and a career in research.

I would also like to thank the rest of the SURF students, Reema, Luis, Luca, and Teahan, and PhD student William, for making my stay in the lab so warm and introducing me to their work. I am also grateful to the Boeing Company for funding the research and offering me the possibility to contribute. Finally, I would like to thank the Caltech SURF program for their continuous support throughout the experience.

## A Numerical Settings

Two sets of numerical schemes were used in the presented cases. The first one was more diffusive, characterized by mostly first-order schemes in both the temporal and spatial discretization. The second set was less diffusive and used mostly second-order schemes in both the temporal and spatial discretizations. The first set was used for the studies presented in Sections 4, and 5. The second set was used for the studies presented in Section 6 and for the reference case from Section 3 to ensure that the oscillatory phenomenon during the convection stabilization process was not numerically damped. No significant differences in the concentration signal were observed between the numerical sets.

The first and second set of discretization schemes are presented in Table 24.

| Term | First set | Second set |
|---|---|---|
| Time | Euler | backward |
| $\nabla \mathbf{U}$ | Gauss linear | cellLimited Gauss linear 1 |
| $\mathrm{div}(\phi, \mathbf{U})$ | Gauss upwind | Gauss linearUpwind grad(U) |
| $\mathrm{div}(\phi_d, p_{rgh})$ | Gauss upwind | Gauss limitedLinear 1 |
| $\mathrm{div}(\phi, K)$ | Gauss upwind | Gauss limitedLinear 1 |
| $\mathrm{div}(\phi, Y_i h)$ | Gauss upwind | Gauss limitedLinear 1 |
| Laplacian | Gauss linear uncorrected | Gauss linear orthogonal |
| Interpolation | linear | linear |
| Surface-normal gradient | uncorrected | orthogonal |

**Table 24:** Discretization schemes used in the two numerical scheme sets.

# B Initialization Issues and Fixes

The simulation framework had an initialization issue that produced an artificial spike in the velocity field. The root cause of the issue was identified as too large values for the initial sequence of time steps. The reason behind this was a mix of the `adjustableTimeStep` option and the initial static field. As the simulation initialized from an almost static field, the time step was selected from the CFL condition, $\mathrm{CFL}_{\max} = u\Delta t/\Delta x \leq 1$. Since $u$ is near zero throughout the field, the solver could select an excessively large timestep in the first iterations that still satisfied the CFL condition, leading to the glitch. In essence, the initial time steps were selected from a condition ($\mathrm{CFL}_{\max}$) that is not sufficiently small to obtain convergence in the nearly static initial conditions.

To address the issue, an initial period with a fixed, small value of the timestep is implemented in the simulations. The `adjustableTimeStep` option with `maxCo = 0.7` is activated later in the simulation, once the flow field has already begun to develop.

# C 3D Simulations

To study the effects of extending the current model to 3D on the reported vaporization signal, a 3D case was simulated. The current case used a $10^6$-cell mesh [$100 \times 100 \times 100$] with an average nominal size of 1 mm to make the simulation feasible with the available computational resources. The side wall boundary conditions imposed on all four side walls were the 85 °C temperature distribution profile from Section 5.2 , as they best matched the experimental signal. The injection shape was imposed as a cylinder of diameter 50 mm and height 5 mm. All injection parameters and simulation settings were kept the same as the ones summarized in Section 5.

Note that a $100 \times 100 \times 100$ mesh is much coarser than the $300 \times 300$ 2D mesh used in previous cases and mesh convergence was not demonstrated for $100 \times 100 \times 100$. A more highly refined case is therefore needed for a fair comparison of results, and the current analysis is considered preliminary.

To estimate the effect of mesh coarseness on the results, a 2D injection case with a $100 \times 100$ grid was simulated. Quantitatively, the 2D $100 \times 100$ case showed a 1.2% earlier convection onset and an 11.3% shorter time from onset to stability relative to the reference case. The larger difference in stability is consistent with a coarser enhancing interface smearing through numerical diffusion.

Returning to the 3D simulation, Table 25 summarizes the characteristic convection timings for

the reference 2D and simplified 3D case. Figure 61 compares the concentration signals for the experimental data, the reference 2D case, and the 3D case.

| Metric | Reference 2D ($300 \times 300$) | 3D ($100 \times 100 \times 100$) |
|---|---|---|
| Time until convection begins [s] | 65.2 | 60.0 |
| Time from onset to stability [s] | 56.4 | 63.0 |

**Table 25:** Characteristic convection timings for the reference 2D simulation and the coarser 3D simulation.

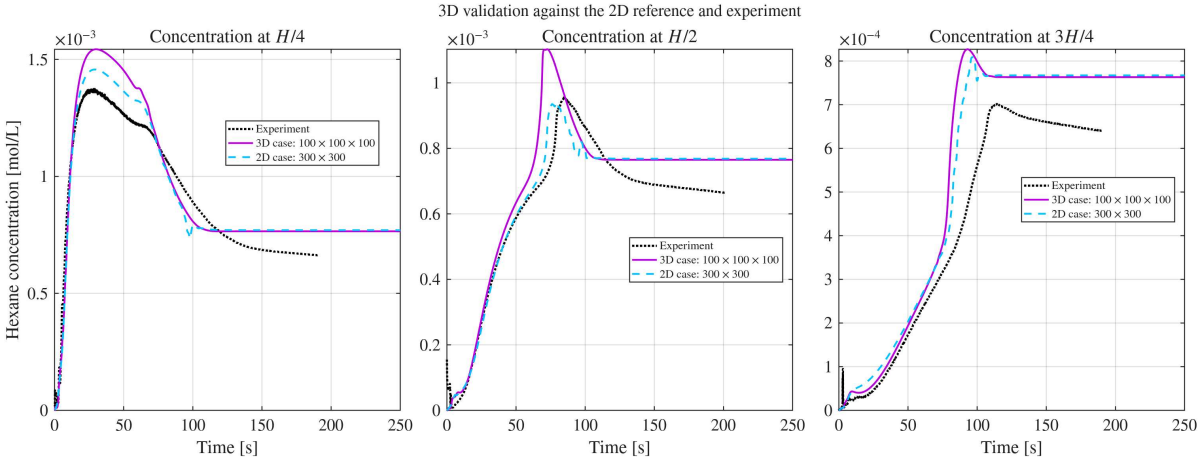



**Figure 61:** Comparison of the line-averaged computed concentration with the experimental data, the reference 2D simulation, and the coarser 3D simulation.

The 3D case shows a substantial increase in the strength of the convection mode, with a higher peak concentration reported for all 3 heights along the flask. The morphology of the peaks is, however, conserved. The timing between the cases is also similar, with the 3D case reporting only an 8.0% faster onset of convection. Figure 62 compares the final stabilized temperature and velocity-magnitude fields at a vertical slice taken through the middle of the cell for the 2D and 3D cases.

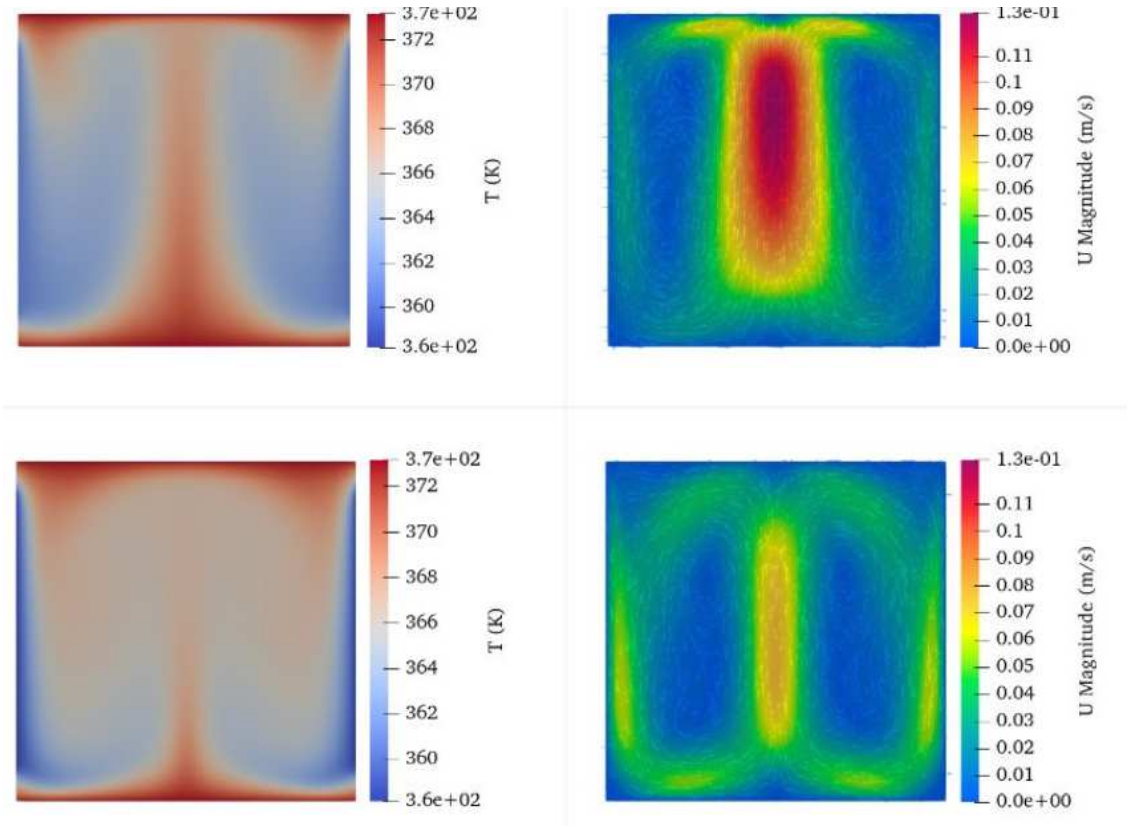



**Figure 62:** Comparison of the final stabilized temperature and velocity-magnitude fields at the mid-plane of the cell for the reference 2D simulation (bottom) and the simplified 3D simulation (top).

The overall morphology of both modes is similar, with a denser mixture falling along the walls and a lighter rising plume through the middle of the cell. The 3D case, however, reports a much wider plume, in addition to approximately twice as fast velocities along it: $0.13\,\mathrm{m\,s^{-1}}$ vs $0.07\,\mathrm{m\,s^{-1}}$) for their maximum values. These observations support the previous findings. Subsequently, the main conclusion of the study is that, at least for an extension of the problem into 3D applying the 2D boundary condition along all four side walls, the added dimension increases the strength of the convective mode but does not substantially change its morphology.

Finally, by looking at a horizontal slice of the velocity field, a diagonal, higher-velocity structure is observed coming from the intersection of the walls. This interaction may happen as a result of the individual vortical structures rolling down through the sides of the windows and interacting, superimposing on one another at the edges. Figure 63 shows a snapshot of the velocity-magnitude field at $Z = H/10$ during the formation of the convection.

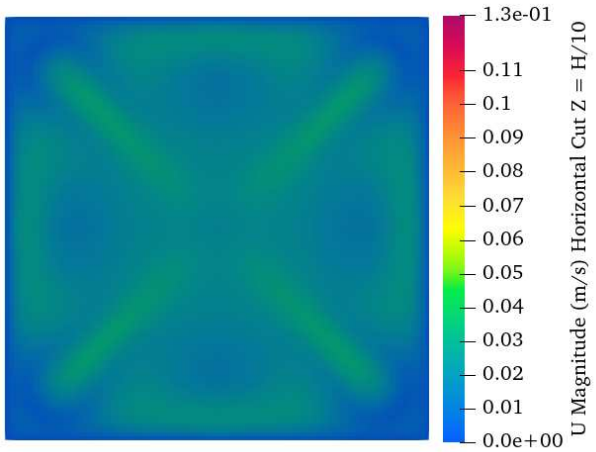



**Figure 63:** Velocity-magnitude field at $Z = H/10$ during the formation of convection in the simplified 3D simulation.

# D Heat-Transfer Model

The cubic cell apparatus of Fouchier et al.[6] consists of a 2 mm thin shell of aluminum, followed by a 2.5 in thick insulated layer of glass-wool, followed by a 2 mm thin quartz-window, a 1 in air gap, and finally the 4 in wide test cell. The air gaps and insulation mean that all conduction, convection, and radiation heat transfer mechanisms will be present in the system. Figure 64 shows a schematic vertical cross section of the experimental apparatus. The figure is not to scale.

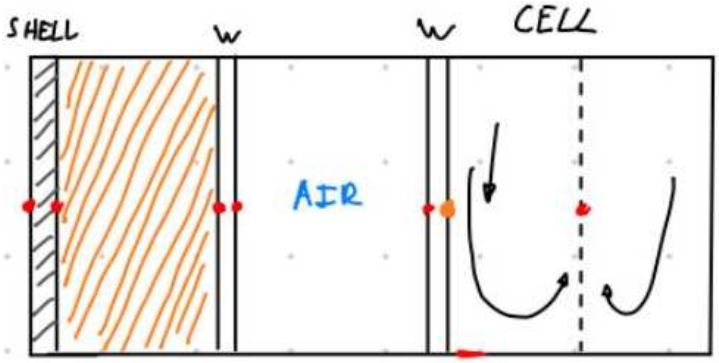



**Figure 64:** Schematic vertical cross section of the experimental apparatus. The figure is not to scale.

The model consists of a simplified steady-state, resistance-based nodal thermal network of the experimental test apparatus. The main assumptions of the model are the following:

- Steady state.
- Stagnant air in the insulating layer.
- Walls are large and parallel to each other (view factor = 1 for radiative surfaces).
- Walls are opaque in the thermal infrared (no transmission).

The thermal characteristics of the experimental apparatus were simplified to a one-dimensional

series of resistance values based on their material and heat transfer properties. For conduction paths, their resistance per unit area is calculated as $R''_{\text{cond}} = \dfrac{L}{k}$. For convective paths, their resistance per unit area is calculated as $R''_{\text{conv}} = \dfrac{1}{h}$. Note that the heat transfer coefficient must be estimated from empirical correlations. Two different approaches were taken for this. The first one, a simple estimation using a Reynolds number-based average Nusselt correlation for laminar forced convection over an isothermal flat plate[16]:

$$\overline{Nu}_L = 0.664\, Re_L^{1/2}\, Pr^{1/3}, \qquad \text{for } Pr > 0.6.$$

where $Re = vL/\nu$, and $v$ was taken as the average velocity along the wall extracted from simulations, $0.05\,\mathrm{m\,s^{-1}}$, and $L$ a characteristic length of the height of the cell 0.10 m, note that this correlation is not intended for the flow as it is based on forced convection, but it serves as an estimation. This approach uncouples convection, as the velocity value is independent of the cell-wall convection forcing $\Delta T$

The second approach uses a Rayleigh-number-based natural convection correlation, specifically, the Churchill–Chu correlation for an isothermal vertical flat plate:[17]

$$Nu_L = 0.68 + \frac{0.670\, Ra_L^{1/4}}{\left[1 + \left(\dfrac{0.492}{Pr}\right)^{9/16}\right]^{4/9}}.$$

This approach couples the temperature difference between the cell and the window through the Rayleigh number

$$Ra_H = \frac{g\,\beta\,(T_{\text{cell}} - T_{\text{window}})\,H^3}{\nu\,\alpha},$$

Note again that our current window is not isothermal and is not fully represented by either of the convection models intended for vertical flat plates and not a cubical cell geometry. They serve only as an initial simplified convection modeling choice. For radiation paths, the radiation resistance per unit area, $R''_{\text{rad}} = \dfrac{1}{h_{\text{rad}}}$, can be estimated as driven from the view factor = 1 and no transmission assumptions where:

$$h_{\text{rad}} = \frac{\sigma\,(T_1 + T_2)\,(T_1^2 + T_2^2)}{\dfrac{1}{\varepsilon_1} + \dfrac{1}{\varepsilon_2} - 1},$$

The temperature-dependent radiation resistance and the coupled convection method will require an iterative solution method for our system. Figure 65 shows the quasi-2D thermal resistance network.

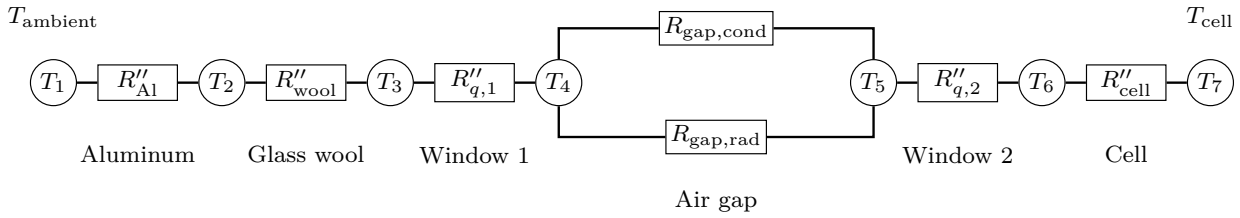



**Figure 65:** Quasi-2D thermal resistance network of the experimental apparatus.

To account for the temperature distribution along the window, the heated top and bottom aluminum plates are considered. For an infinitesimal amount of window wall, in steady state, across the window, $\sum q'' \, \mathrm{d}A = 0$, considering $T$ homogeneous on both sides as the window thickness is very small:

$$q''(y)\, t_q - q''(y + \mathrm{d}y)\, t_q = (q''_r + q''_l)\, \mathrm{d}y$$

Where $q''(y)$ is the vertical heat flux entering the glass, $q''(y + \mathrm{d}y)$ is the vertical heat flux leaving the glass, and $q''_l$ and $q''_r$ are the horizontal heat fluxes entering through the left and right boundaries, respectively. The equation can be further developed as a function of temperature as:

$$k_q\, t_q \, \frac{\mathrm{d}^2 T}{\mathrm{d}y^2} - \frac{T - T_{\text{amb}}}{R''_{\text{amb}}} - \frac{T - T_{\text{cell}}}{R''_{\text{cell}}} = 0.$$

Where $R''_{\text{amb}}$ is the total area-specific thermal resistance network of the window wall toward the ambient side, and $R''_{\text{cell}}$ is the total area-specific thermal resistance of the window wall toward the cell side. Fixing the boundary conditions at the top and bottom of the window at 100 °C, assuming a small contact resistance with the aluminum, the temperature distribution along the window can be solved analytically as a function of the heat transfer on either side of the wall:

$$T(y) = f(R''_{\text{amb}},\, R''_{\text{cell}})\,.$$

The model then solves for the system nodal temperatures and window temperature distribution through the following algorithm:

1. Starts from an initial temperature estimate.
2. Calculates the thermal resistances.
3. Determines convection:
   - Using the coupled Rayleigh-number correlation, or
   - Using the uncoupled Reynolds-number correlation.
4. Solves the analytical expressions for $T(y)$ and $T_{\text{mean}}$ in the window node.
5. Calculates the heat transfer in the rest of the 1D system as: $q'' = \dfrac{\Delta T}{R''}$.
6. Updates the nodal temperatures.
7. Repeats until convergence.

A targeted Monte Carlo simulation was implemented to account for the uncertainty in the cell reference temperature 95 °C to 100 °C, which differs across the cell, and the imposed velocity for the Reynolds-number-based correlation $0.03\,\mathrm{m\,s^{-1}}$ to $0.07\,\mathrm{m\,s^{-1}}$.

# E Derivations

## E.1 1D Diffusion Analytical Model

The 1D analytical model solves the binary diffusion case by solving the diffusion equation,

$$\frac{\partial c}{\partial t} = D\frac{\partial^2 c}{\partial z^2} \tag{31}$$

Through separation of variables and a Fourier series expansion for a closed, constant-temperature and constant-pressure cell[6], the solution yields the form

$$c(t,z) = c_0\left[\frac{\delta}{H} + 2\sum_{n=1}^{\infty}\frac{1}{n\pi}\exp\left(-\frac{Dn^2\pi^2 t}{H^2}\right)\cos\left(\frac{n\pi z}{H}\right)\sin\left(\frac{n\pi\delta}{H}\right)\right] \tag{32}$$

where $c_0$ is the initial concentration of hexane, $\delta$ is the height of the initialized vapor layer, $H$ is the height of the cell, and $D$ is the binary diffusion coefficient.

## E.2 Navier Stokes Non-Dimensional Equations

The non-dimensionalization of the following equations is based on the derivations done by Davis[14] These derivations rely on several assumptions and are not intended to replicate the exact formulations used in the numerical simulations. Its purpose is to provide insight into the non-dimensional groups that drive the mixing phenomena observed in the cell.

**Momentum Equation**

We start with the momentum equation for a buoyancy-driven, variable-density flow.

$$\rho\frac{\partial \mathbf{u}}{\partial t} + \rho(\mathbf{u}\cdot\nabla)\mathbf{u} = -\nabla p + \rho\mathbf{g} + \nabla\cdot\boldsymbol{\tau}. \tag{33}$$

We introduce a reference hydrostatic state such that.

$$\rho = \rho_0 + \rho', \qquad p = p_0 + p', \tag{34}$$

$$\nabla p_0 = \rho_0\mathbf{g}. \tag{35}$$

Substituting into Equation. 33 yields

$$(\rho_0+\rho')\frac{\partial \mathbf{u}}{\partial t} + (\rho_0+\rho')(\mathbf{u}\cdot\nabla)\mathbf{u} = -\nabla(p_0+p') + (\rho_0+\rho')\mathbf{g} + \nabla\cdot\boldsymbol{\tau}. \tag{36}$$

Removing the hydrostatic terms and dropping the superscript prime notation gives

$$\rho\frac{\partial \mathbf{u}}{\partial t} + \rho(\mathbf{u}\cdot\nabla)\mathbf{u} = -\nabla p + \Delta\rho\,\mathbf{g} + \nabla\cdot\boldsymbol{\tau}, \tag{37}$$

where $\Delta\rho$ is the density variation associated with the buoyancy force.

Using Stokes' hypothesis for a Newtonian fluid

$$\boldsymbol{\tau} = \mu\left[\nabla\mathbf{u} + (\nabla\mathbf{u})^T - \frac{2}{3}(\nabla\cdot\mathbf{u})\mathbf{I}\right]. \tag{38}$$

Substituting into Eq. 37 yields

$$\begin{aligned}\rho\frac{\partial\mathbf{u}}{\partial t} + \rho(\mathbf{u}\cdot\nabla)\mathbf{u} = & -\nabla p + \Delta\rho\,\mathbf{g} \\ & + \nabla\cdot\left\{\mu\left[\nabla\mathbf{u} + (\nabla\mathbf{u})^T - \frac{2}{3}(\nabla\cdot\mathbf{u})\mathbf{I}\right]\right\}.\end{aligned} \tag{39}$$

Assuming pressure variations are small enough so that viscosity is only temperature dependent and the identities

$$\nabla\mu = \frac{\partial\mu}{\partial T}\nabla T. \tag{40}$$

$$\nabla\cdot(a\mathbf{b}) = a\nabla\cdot\mathbf{b} + (\nabla a)\cdot\mathbf{b}. \tag{41}$$

$$\nabla\cdot(\nabla\mathbf{u}) = \nabla^2\mathbf{u}, \tag{42}$$

$$\nabla\cdot(\nabla\mathbf{u})^T = \nabla(\nabla\cdot\mathbf{u}), \tag{43}$$

the momentum equation becomes

$$\begin{aligned}\rho\frac{\partial\mathbf{u}}{\partial t} + \rho(\mathbf{u}\cdot\nabla)\mathbf{u} = & -\nabla p + \Delta\rho\,\mathbf{g} + \mu\nabla^2\mathbf{u} + \left(\frac{\partial\mu}{\partial T}\nabla T\right)\cdot\nabla\mathbf{u} + \mu\nabla(\nabla\cdot\mathbf{u}) \\ & + \left(\frac{\partial\mu}{\partial T}\nabla T\right)\cdot(\nabla\mathbf{u})^T - \frac{2}{3}\mu\nabla(\nabla\cdot\mathbf{u}) - \frac{2}{3}\left(\frac{\partial\mu}{\partial T}\nabla T\right)\cdot[(\nabla\cdot\mathbf{u})\mathbf{I}].\end{aligned} \tag{44}$$

Assuming now the flow is incompressible, following Davis's analysis

$$\nabla\cdot\mathbf{u} = 0. \tag{45}$$

The momentum equation then reduces to

$$\boxed{\begin{aligned}\rho\frac{\partial\mathbf{u}}{\partial t} + \rho(\mathbf{u}\cdot\nabla)\mathbf{u} = & -\nabla p + \Delta\rho\,\mathbf{g} + \mu\nabla^2\mathbf{u} \\ & + \left(\frac{\partial\mu}{\partial T}\nabla T\right)\cdot\left[\nabla\mathbf{u} + (\nabla\mathbf{u})^T\right].\end{aligned}} \tag{46}$$

Defining the non-dimensional variables Davis used introduced in Section 3.7

$$t^* = \frac{\alpha_0 t}{L^2}, \qquad \nabla^* = L\nabla, \qquad \mathbf{u}^* = \frac{L\mathbf{u}}{\alpha_0}, \tag{47}$$

$$p^* = \frac{pL^2}{\rho_0 \alpha_0^2}, \qquad \rho^* = \frac{\rho}{\rho_0}, \qquad \Theta = \frac{T}{T_0}, \qquad \mu^* = \frac{\mu}{\mu_0}. \tag{48}$$

Then,

$$t = \frac{L^2}{\alpha_0} t^*, \qquad \nabla = \frac{1}{L}\nabla^*, \qquad \mathbf{u} = \frac{\alpha_0}{L}\mathbf{u}^*, \tag{49}$$

$$p = \frac{\rho_0 \alpha_0^2}{L^2} p^*, \qquad \rho = \rho_0 \rho^*, \qquad T = T_0 \Theta, \qquad \mu = \mu_0 \mu^*. \tag{50}$$

Substituting into Eq. 46 and writing

$$\mathbf{g} = g\mathbf{e}_g, \tag{51}$$

gives

$$\begin{aligned} \frac{\rho_0 \alpha_0^2}{L^3}\rho^* \frac{\partial \mathbf{u}^*}{\partial t^*} + \frac{\rho_0 \alpha_0^2}{L^3}\rho^* \mathbf{u}^* \cdot \nabla^* \mathbf{u}^* = & -\frac{\rho_0 \alpha_0^2}{L^3}\nabla^* p^* + g\Delta\rho\, \mathbf{e}_g + \frac{\mu_0 \alpha_0}{L^3}\Big\{\mu^* \nabla^{*2}\mathbf{u}^* \\ & + \frac{\partial \mu^*}{\partial \Theta}(\nabla^* \Theta) \cdot \Big[\nabla^* \mathbf{u}^* + (\nabla^* \mathbf{u}^*)^T\Big]\Big\}. \end{aligned} \tag{52}$$

Dividing by $\rho_0 \alpha_0^2 / L^3$

$$\begin{aligned} \rho^* \frac{\partial \mathbf{u}^*}{\partial t^*} + \rho^* \mathbf{u}^* \cdot \nabla^* \mathbf{u}^* = & -\nabla^* p^* + \frac{\Delta\rho\, g L^3}{\rho_0 \alpha_0^2}\mathbf{e}_g + \frac{\mu_0}{\rho_0 \alpha_0}\Big\{\mu^* \nabla^{*2}\mathbf{u}^* \\ & + \frac{\partial \mu^*}{\partial \Theta}(\nabla^* \Theta) \cdot \Big[\nabla^* \mathbf{u}^* + (\nabla^* \mathbf{u}^*)^T\Big]\Big\}. \end{aligned} \tag{53}$$

Using the Rayleigh and Prandtl numbers

$$Ra_0 = \frac{\Delta\rho\, g L^3}{\mu_0 \alpha_0}, \qquad Pr_0 = \frac{\nu_0}{\alpha_0} = \frac{\mu_0}{\rho_0 \alpha_0}. \tag{54}$$

Equation 53 becomes

$$\boxed{\begin{aligned} \rho^* \frac{\partial \mathbf{u}^*}{\partial t^*} + \rho^* \mathbf{u}^* \cdot \nabla^* \mathbf{u}^* = & -\nabla^* p^* + Ra_0 Pr_0\, \mathbf{e}_g + Pr_0\Big\{\mu^* \nabla^{*2}\mathbf{u}^* \\ & + \frac{\partial \mu^*}{\partial \Theta}(\nabla^* \Theta) \cdot \Big[\nabla^* \mathbf{u}^* + (\nabla^* \mathbf{u}^*)^T\Big]\Big\}. \end{aligned}} \tag{55}$$

Thus, it can be seen that the Rayleigh and Prandtl numbers are critical non-dimensional groups governing buoyancy and viscous momentum transport, and the mixing process in the cell.

**Species Equation**

Starting from the species equation used in the current work:

$$\frac{\partial(\rho Y_f)}{\partial t} + \nabla \cdot (\rho \mathbf{u} Y_f) = \nabla \cdot (\rho D \nabla Y_f) + S_{m,f}. \tag{56}$$

After the vaporization process,

$$S_{m,f} = 0, \tag{57}$$

and Eq. 56 becomes

$$\frac{\partial(\rho Y_f)}{\partial t} + \nabla \cdot (\rho \mathbf{u} Y_f) = \nabla \cdot (\rho D \nabla Y_f)\,. \tag{58}$$

In addition, after vaporization, mass conservation is simple.

$$\frac{\partial \rho}{\partial t} + \nabla \cdot (\rho \mathbf{u}) = 0. \tag{59}$$

Expanding the temporal and advective terms

$$\frac{\partial(\rho Y_f)}{\partial t} = Y_f \frac{\partial \rho}{\partial t} + \rho \frac{\partial Y_f}{\partial t}, \tag{60}$$

$$\nabla \cdot (\rho \mathbf{u} Y_f) = Y_f \nabla \cdot (\rho \mathbf{u}) + \rho \mathbf{u} \cdot \nabla Y_f. \tag{61}$$

Therefore,

$$\rho \left( \frac{\partial Y_f}{\partial t} + \mathbf{u} \cdot \nabla Y_f \right) + Y_f \left[ \frac{\partial \rho}{\partial t} + \nabla \cdot (\rho \mathbf{u}) \right] = \nabla \cdot (\rho D \nabla Y_f)\,. \tag{62}$$

And substituting Eq. 59, the species equation can be written as

$$\boxed{\rho \left( \frac{\partial Y_f}{\partial t} + \mathbf{u} \cdot \nabla Y_f \right) = \nabla \cdot (\rho D \nabla Y_f)\,.} \tag{63}$$

Using the same non-dimensional groups as in the momentum equation,

$$t^* = \frac{\alpha_0 t}{L^2}, \qquad \nabla^* = L\nabla, \qquad \mathbf{u}^* = \frac{L\mathbf{u}}{\alpha_0}, \qquad \rho^* = \frac{\rho}{\rho_0}. \tag{64}$$

The species and diffusion groups are defined as

$$Y_f^* = \frac{Y_f - Y_{f,0}}{\Delta Y_f}, \qquad D^* = \frac{D}{D_0}. \tag{65}$$

$$Y_f = Y_{f,0} + \Delta Y_f Y_f^*, \qquad D = D_0 D^*. \tag{66}$$

Substituting into Eq. 63 gives

$$\frac{\rho_0 \alpha_0 \Delta Y_f}{L^2} \rho^* \left( \frac{\partial Y_f^*}{\partial t^*} + \mathbf{u}^* \cdot \nabla^* Y_f^* \right) = \frac{\rho_0 D_0 \Delta Y_f}{L^2} \nabla^* \cdot \left( \rho^* D^* \nabla^* Y_f^* \right). \tag{67}$$

Dividing by

$$\frac{\rho_0 \alpha_0 \Delta Y_f}{L^2} \tag{68}$$

yields

$$\rho^* \left( \frac{\partial Y_f^*}{\partial t^*} + \mathbf{u}^* \cdot \nabla^* Y_f^* \right) = \frac{D_0}{\alpha_0} \nabla^* \cdot \left( \rho^* D^* \nabla^* Y_f^* \right). \tag{69}$$

Where the Lewis number is

$$Le_0 = \frac{\alpha_0}{D_0}, \tag{70}$$

and the nondimensional species equations become

$$\boxed{\rho^* \left( \frac{\partial Y_f^*}{\partial t^*} + \mathbf{u}^* \cdot \nabla^* Y_f^* \right) = \frac{1}{Le_0} \nabla^* \cdot \left( \rho^* D^* \nabla^* Y_f^* \right).} \tag{71}$$

Because the binary fuel-air diffusion coefficient is defined as a constant in the current work, $D/D_0 = 1$ and $D^* = 1$ such that the species equation becomes

$$\boxed{\rho^* \left( \frac{\partial Y_f^*}{\partial t^*} + \mathbf{u}^* \cdot \nabla^* Y_f^* \right) = \frac{1}{Le_0} \nabla^* \cdot \left( \rho^* \nabla^* Y_f^* \right).} \tag{72}$$

The Lewis number is the critical nondimensional group governing species diffusion relative to thermal diffusion.

### E.3 Frequency of Internal Waves in a Box

The derivation for the characteristic frequency of internal waves in a box is based on a problem from p. 40 of Landau and Lifshitz [18] and Prof. Shepherd's internal notes.

We consider two stratified fluids in a two-dimensional box, as in the simulation domain of the current work. We consider the lower fluid to have a density $\rho_1$ and depth $h_1$, and the upper fluid to have a density $\rho_2$ and a depth $h_2$. The interface is located at $z = 0$.

$$z = -h_1, \qquad z = +h_2. \tag{73}$$

at the bottom wall and at the top wall.

The total height $H$ can be calculated as

$$H = h_1 + h_2. \tag{74}$$

Assuming a stable stratification such that

$$\rho_1 > \rho_2. \tag{75}$$

**Assumptions**

The density constant in each layer and motion in each layer is that of an incompressible fluid,

$$\nabla \cdot \mathbf{u} = 0, \tag{76}$$

So we can obtain the velocity field from the velocity potential.

$$\mathbf{u} = \nabla\phi, \qquad \mathbf{u} = (u, w), \tag{77}$$

with

$$w = \frac{\partial\phi}{\partial z}, \qquad u = \frac{\partial\phi}{\partial x}. \tag{78}$$

The corresponding boundary conditions are no-penetration conditions at the domain walls.

$$w = 0 \qquad \text{at} \qquad z = \begin{cases} +h_2, \\ -h_1, \end{cases} \tag{79}$$

$$u = 0 \qquad \text{at} \qquad x = 0, H. \tag{80}$$

Solving the differential equation, we obtain the following potential functions.

$$\phi_2 = A_2 \cosh\left[k(z - h_2)\right] \cos(kx) e^{-i\omega t}, \tag{81}$$

$$\phi_1 = A_1 \cosh\left[k(z + h_1)\right] \cos(kx) e^{-i\omega t}. \tag{82}$$

The no-penetration boundary conditions at $z = -h_1$ and $z = +h_2$ are automatically satisfied.

At $x = 0, H$,

$$\sin(kx) = 0, \tag{83}$$

such that

$$k_n H = n\pi, \qquad n = 0, 1, 2, 3, \ldots \tag{84}$$

the wavenumber and wavelength are then

$$k_n = \frac{n\pi}{H}, \qquad k = \frac{2\pi}{\lambda}, \qquad \lambda = \frac{2H}{n}. \tag{85}$$

Matching now at the interface, let

$$\eta(t, x, y) \tag{86}$$

denote the height of the interface above $z = 0$.

The vertical velocity of the interface must be the same as the fluid velocity of both sides of the interface.

$$w = \left.\frac{\partial \eta}{\partial t}\right|_{z=0} = \left.\frac{\partial \phi_1}{\partial z}\right|_{z=0} = \left.\frac{\partial \phi_2}{\partial z}\right|_{z=0}. \tag{87}$$

This implies motion of the interface must be of the form

$$\eta = Ce^{-i\omega t}\cos(kx). \tag{88}$$

Solving for both fluids

$$-i\omega C = A_1 k \sinh(kh_1), \qquad -i\omega C = -A_2 k \sinh(kh_2). \tag{89}$$

$$A_1 = \frac{-i\omega C}{k\sinh(kh_1)}, \qquad A_2 = \frac{+i\omega C}{k\sinh(kh_2)}. \tag{90}$$

**Pressure Matching**

Applying the common unsteady, linearized Bernoulli equation used in linearized water wave theory

$$P_i = -\rho_i \frac{\partial \phi_i}{\partial t} - \rho_i g \eta. \tag{91}$$

Matching pressure at the interface

$$P_1 = P_2 \qquad \text{at} \qquad z = 0. \tag{92}$$

$$\rho_1 \frac{\partial \phi_1}{\partial t} - \rho_2 \frac{\partial \phi_2}{\partial t} = (\rho_2 - \rho_1) g \eta. \tag{93}$$

At $z = 0$,

$$-i\omega\left[\rho_1 A_1\cosh(kh_1)-\rho_2 A_2\cosh(kh_2)\right]=(\rho_2-\rho_1)g\eta. \tag{94}$$

Substituting Eqn for $A_1$ and $A_2$ yields

$$-i\omega\left[\frac{-i\omega\rho_1\cosh(kh_1)}{k\sinh(kh_1)}-\frac{i\omega\rho_2\cosh(kh_2)}{k\sinh(kh_2)}\right]=(\rho_2-\rho_1)g. \tag{95}$$

$$-\frac{\omega^2}{k}\left[\rho_1\coth(kh_1)+\rho_2\coth(kh_2)\right]=(\rho_2-\rho_1)g. \tag{96}$$

$$\boxed{\omega^2=\frac{k(\rho_1-\rho_2)g}{\rho_1\coth(kh_1)+\rho_2\coth(kh_2)}} \tag{97}$$

Using the angular frequency and the wavenumber

$$\omega=2\pi f,\qquad k_n=\frac{n\pi}{H}. \tag{98}$$

The corresponding mode frequencies are

$$\boxed{f_n=\frac{1}{2\pi}\sqrt{\frac{\frac{n\pi}{H}(\rho_1-\rho_2)g}{\rho_1\coth\left(\frac{n\pi h_1}{H}\right)+\rho_2\coth\left(\frac{n\pi h_2}{H}\right)}}}. \tag{99}$$